SISSA
Scuola
Internazionale
Superiore di
Studi Avanzati

Neuroscience Area – PhD course in Neurobiology

AFM applications to native cell membranes and membrane proteins

Candidate:
Nicola Galvanetto

Advisor:
Prof. Vincent Torre

Academic Year 2018-19

Scuola Internazionale Superiore di Studi Avanzati

Doctoral Thesis

AFM applications to native cell membranes and membrane proteins

Author:
Nicola Galvanetto

Supervisor:
Prof. Vincent Torre

A thesis submitted in fulfillment of the requirements for the degree of Doctor of Philosophy

Neurobiology - Biophysics

October, 2019

"*At the end of the day, you are making order from disorder.*"

Anonymous

Abstract

The cell membrane is a special casing necessary to keep homeostasis for cells survival. It is a two-dimensional agglomeration of lipids that holds a large number of membrane proteins with diverse vital functions. The fluid nature of the membrane makes it difficult to be handled, and requires the development of *ad hoc* techniques to investigate its properties and composition.

In this PhD thesis, I developed a method to isolate the apical cell membrane of single cells. Taking advantage of the Atomic Force Microscope (AFM), I imaged and probed the mechanical properties of these isolated patches of membranes. I also extensively performed AFM-based single-molecule force spectroscopy to unfold the membrane proteins from the native membranes, collecting hundreds of thousands of unfolding curves. I analyzed these data with a custom software able to find the recurrent pattern of unfolding in the data, and I developed a Bayesian inference method to assign these unfolding curves to a limited number of membrane proteins. The underlying motivation of these experiments is to bring AFM technologies a step closer to an application in biomedicine.

This work demonstrates that *i)* the cell membrane can be reliably isolated from single cells; *ii)* AFM can be used to characterize the membrane topography and mechanical properties of the cells of interest (e.g. I found that neural cell membranes are thicker and stiffer than membranes of brain cancer cells); *iii)* it is possible to record the unfolding pathways of the membrane proteins contained in the cell membranes and to identify them with the cross-matching of proteomic databases, and *iv)* the population of unfolding curves obtained with SMFS reflects the actual population of membrane proteins obtained with Mass Spectrometry.

Contents

List of publications

- **N. Galvanetto**, A. Perissinotto, A. Pedroni, V. Torre, Fodis: Software for Protein Unfolding Analysis, Biophysical Journal, 114 (2018) 12641266.
- **N. Galvanetto**, Single-cell unroofing: probing topology and nanomechanics of native membranes, Biochimica et Biophysica Acta (BBA) - Biomembranes, 1860 (2018) 25322538.
- N. Ilieva, **N. Galvanetto**, M. Allegra, V. Torre, A. Laio, Automatic classification of single-molecule force spectroscopy traces from samples containing heterogeneous mixtures of proteins, *submitted*.
- **N. Galvanetto**, S. Maity, N. Ilieva, A. Laio, V. Torre, Unfolding and identification of membrane proteins from native cell membranes, BioRxiv, (2019) 732933.

Chapter 1

Introduction

Atomic Force Microscopy in biology

In this introductory chapter I will provide some background information which will be useful to appreciate the goals and the challenges that have guided my PhD work.

1.1 Background

The progress of science is usually a graded process, but once in a while it happens to show discontinuities due to some disruptive revolutions. In physics there have been mostly conceptual revolutions: theories that allows to link experimental results that were previously uncorrelated; in modern biology, on the contrary, there have been mostly *technological* revolutions: techniques that enable (previously) unthinkable experiments.

The invention of the Atomic Force Microscope (AFM [1]; Figure 1.1 a) is one of these revolutions.

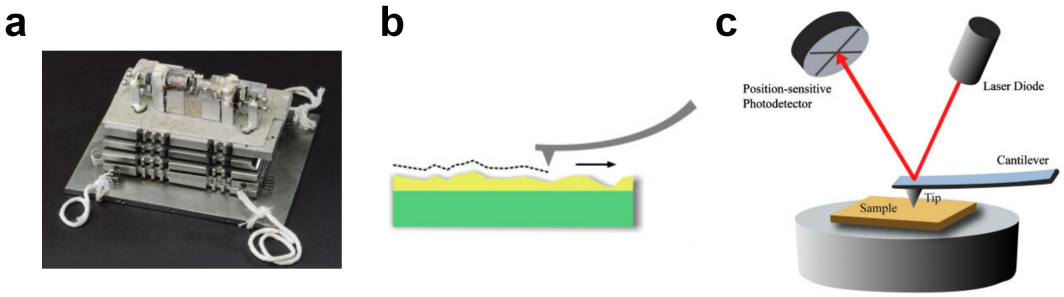

Fig. 1.1: a: picture of the first AFM built in 1985 by Binnig and colleagues [1]. b: sketch of an AFM probe moving on top of the imaged surface (adapted from ref. [2]). c: basic scheme of a AFM device (adapted from ref. [2])

1.2 AFM is an enabling technology still under development

1.2.1 AFM is a special kind of microscope

The word *microscope* derives from the Greek words *mikros*—"small"—and *skopein*—"to look". If we took literally this definition, it wouldn't be right to call the Atomic Force Microscope really a 'microscope', because AFMs are metaphorically much closer to touch than to sight. Indeed, the basic working principle of the AFM is that of a tip that touches and moves on top of a surface (Figure 1.1 b).

The working principle is simple, but the necessary technology to bring it to sub-nanometric precision is all but not trivial. Broadly speaking, the goal is to raster scan the surface of the sample with a tiny probe (cantilever tip), to record the scanned information as X-Y-Z coordinates, and to reconstruct this map into a topographical image true to the original sample. A modern AFM [3] is constituted by a micrometric cantilever with a sharp tip on one side, and connected to a cantilever holder on the other (Figure 1.1 c). The cantilever holder is fixed to a piezo tube (a piezoelectric crystal fused in a tubular volume) necessary to move the cantilever tip in the X-Y-Z directions. The piezo tube is a key element because it uses the special property of piezo crystals to deform in a very accurate manner under high electric voltages, thus to move the cantilever with sub-nanometric precision. The forces to which the cantilever is subjected are constantly monitored through a laser beam that points to the cantilever and reflects into a photodetector (Figure 1.1 c): in this way, even the smallest deflections of the cantilever are detected by the photodetector as movements of the laser spot. Moreover, in the regime of small deflections, the cantilever behave like a spring, therefore the AFM can not only be used to raster scan a surface, but also to measure forces applied to an extremely small area (i.e. the apex of the tip). The power of the AFM comes from the fine intercombination of these elements and from the miniaturization that started in the 60s, on the wave of the silicon revolution.

To summarize, an AFM is the combination of three advanced technologies: piezoelectric crystals, microfabrication for the cantilever tip, laser and electronics for the control device. In the following, I will briefly review the advancements in microfabrication and electronics that represent the domains of major gain of AFM performance of the last few years.

1.2.2 'Make it smaller and faster' (microfabrication & electronics)

The resolution of the AFM depends on the size of the probe that is used to scan the surface of interest. In order to follow nanometer features, tips with an apex with nanometer radius of curvature are essential. Moreover, if the sample presents densely packed hills and holes, the tip necessitates to enter the holes and follow every detail in order to generate a faithful topographical representation of the sample (Figure 1.2 a). For these reasons, scientist developed methods

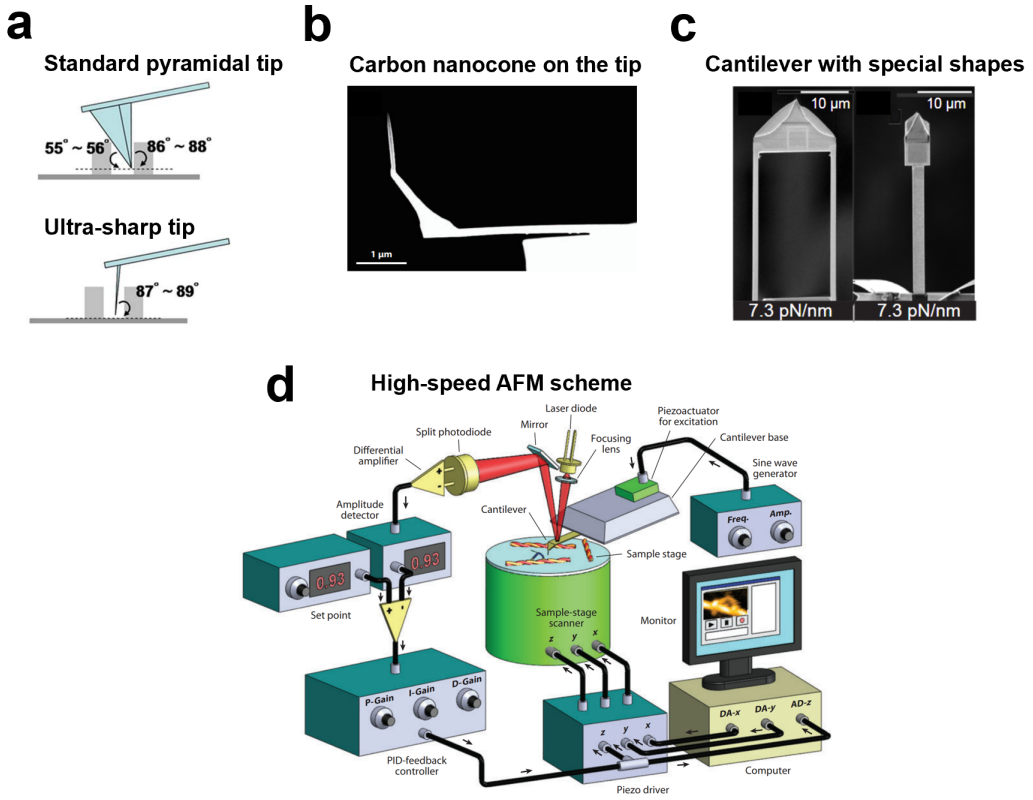

Fig. 1.2: a: comparison between a standard tip vs an ultra-sharp tip [4]. b: scanning electron microscopy image of an ultra-sharp tip (with carbon nanotube grown on top of a silicon tip; adapted from ref. [5]). c: top views of modified cantilevers for enhanced temporal resolution (adapted from ref. [6]). d: scheme of the electronic devices necessary for a high-speed AFM (adapted from ref. [5]).

to grow on top of the cantilever—or on top of the cantilever tip itself (Figure 1.2 b)—an additional ultra-sharp tip made of carbon atoms. This additional tip can be several μm high and can have a radius of curvature of 1-2 nm [4], so to follow the finest details of the sample.

But it is not only a matter of tips, indeed the quality of the topographical reconstruction depends also on the size of the cantilever. As a general principle, the smaller the better, because a small lever is softer (less invasive) and lighter (less inertia). The challenges were a) to manufacture small and precise levers and b) to adapt the AFM accordingly. The advancements in microelectronics allowed to have the right technology to build small probes, and these small probes were also modified (sculptured) with Focused Ion Beams to make them even softer and lighter (Figure 1.2 c) [6]. Once small probes were made, a standard AFM became inadequate, in particular in the laser-photodetector coupling. In order to focus the laser beam onto these new small probes, the AFMs were customized with an optical objective necessary to focus the light onto the smaller reflection area of the new levers. Now that all the ingredients for better AFMs were ready, the last step was to make them faster. An AFM image used to require several minutes to be recorded. Therefore, AFMs were equipped with special ultra-fast electronics giving birth to what is now called High-speed AFM (HS-AFM) (Figure 1.2 d), which can be considered a second

revolution in the field [5].

1.3 AFM is a microscope for unlabeled molecules

Biology and modern medicine make extensive use of imaging techniques, and in particular of fluorescence microscopy [7, 8] (Figure 1.3 c). The general idea underlying fluorescence microscopy is to obtain signals from the specific biomolecule of interest, and to associate it with its spatial distribution in the sample, hopefully also for quantitative assessments. The biomolecule of interest is in almost all cases not fluorescent—i.e. invisible—therefore it needs to be labeled with another fluorescent molecule to be detected. In any case, with the exception of particular applications of Forster Resonance Energy Transfer (FRET), no structural information of the biomolecules can be obtained with fluorescence microscopy.

To obtain structural information, structural biology and pharmacology use X-ray crystallography, NMR, and more recently cryo-EM to investigate the internal structure of the biomolecule of interest [9, 10] (Figure 1.3 a). With these techniques it is possible to reach sub-nanometer resolution of the 3D arrangements of the amino acids in the case of proteins, which is very relevant in drug design. To gather these structural information there are some experimental steps which include the purification of the biomolecule, or its freezing, that necessarily does not allow to keep the molecules in a physiological (not even almost-physiological) environment.

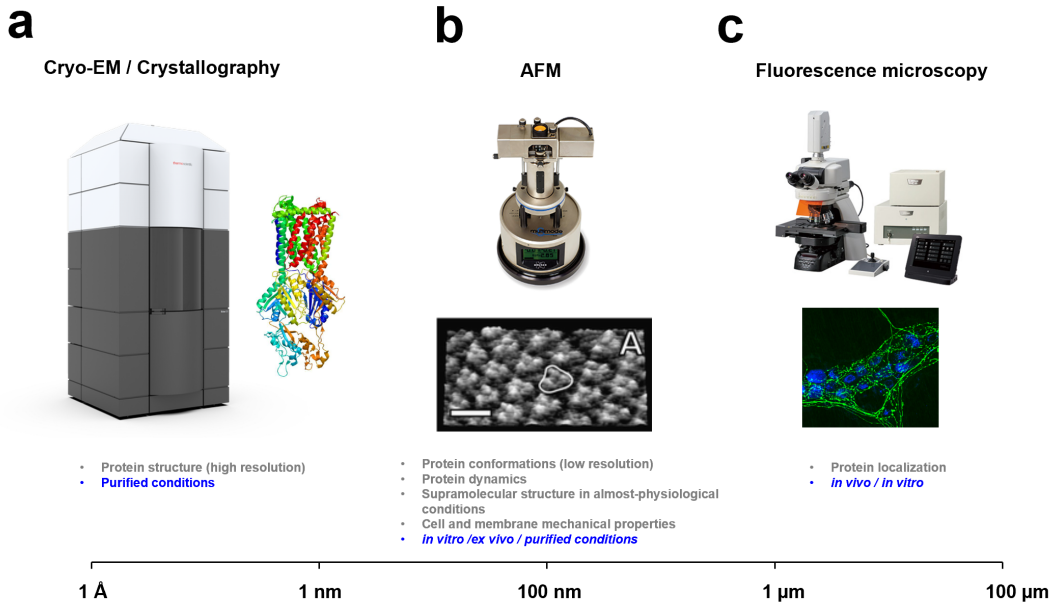

Fig. 1.3: Comparison of imaging techniques for biomolecules and their domains of application, a: for structural, high-resolution, imaging . b: for intermediate molecular imaging with dynamics (adapted from ref. [11]). c: for cellular imaging of biomolecules localization.

There are situations, or scientific prerequisites, where either the label cannot be applied, or the project necessitate structural and dynamical information

of the biomolecule in an almost-physiological environment. For these kind of situations, the AFM is the ideal microscopy technique because it sits exactly in between fluorescence microscopy and crystallography/cryo-EM (Figure 1.3 b).

1.3.1 Purified proteins reconstituted in membranes

Despite of being the target of about 50% of modern drugs [12], structural studies was particularly complicated with membrane proteins that are not prone to crystallization because they have a biphasic surface (hydrophilic at the poles and hydrophobic at the equator to accommodate the membrane) and therefore it is difficult to measure the structural effect of a ligand.

In the late 80s, the newborn AFM that was invented for applications on semiconductors and insulators entered also the biology departments, and the first pioneering studies on membrane proteins began. The first membrane protein for which it was developed a protocol for AFM imaging was bacteriorhodopsin [13] (Figure 1.4 a), a membrane protein that form 2D crystal called purple membranes. Some years later it was possible to reach sub-molecular resolution and compare the AFM topographs with the atomic model derived from electron microscopy [14] (Figure 1.4 b). The real AFM advantages over electron microscopy started to be evident at this point: indeed AFM could be operated in liquid, i.e. emulating the physiological conditions of the membrane proteins environment. For instance, Muller et al. [14] showed that by changing the pH of the imaging solution, the purple membrane displayed conformational changes in its structure. Later studies demonstrated also that the application of forces induced changes in the bacteriorhodopsin structure [15] opening the way for "multidimensional" molecular imaging. In this regard, a more recent study of bacteriorhodopsin mechanical response [16] reached such a high level of precision that allowed the authors to determine which are the stiffest and which are the softest domains within the single protein. But the class of membrane proteins that is the most natural subject of investigation for a technique that allows to measure forces are the mechanosensitive proteins, e.g. PIEZO channels. In mechanosensitive proteins, the application of forces is thought to be responsible of key structural changes (like channel gating). This is exactly what a recent study searched for in a combination of cryo-EM and AFM experiments, where authors were able to propose a mechanisms that translate the forces applied to the membrane to channel gating [17].

What was lacking in these experiments was a dynamical point of view in the time-scale of seconds. The slow operation mode of conventional AFMs was boosted starting from the year 2010 when T. Ando and his group introduced the technical improvements described in section 1.2.2 and built the first High-Speed AFM, which could acquire several frames per second. The fast frame rate enabled the visualization of fast molecular mechanisms, for instance, the first direct imaging of thee movements of myosin [20] or the diffusion of membrane proteins in membranes [18] (Figure 1.4 c).

I believe that HS-AFM will become increasingly prominent for practical applications in drug discovery because it allows to directly probe the structural effects of ligands on the membrane protein of interest with a relatively simple

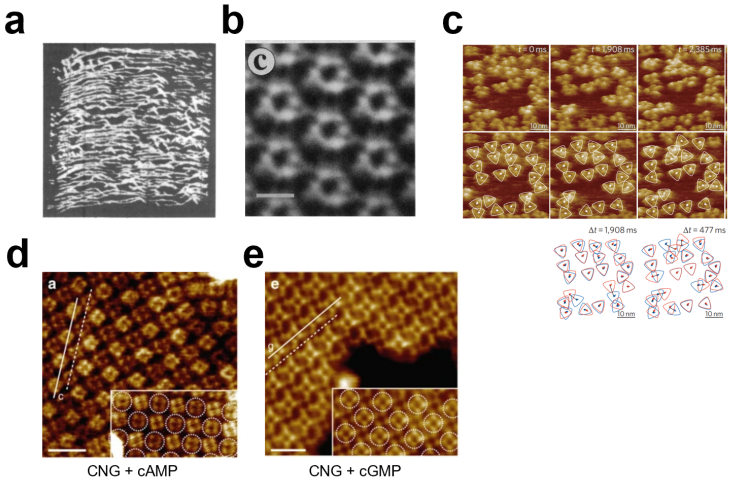

Fig. 1.4: a: AFM line scans of purple membranes in 1988 [13]. b: sub-molecular resolution of purple membranes in 1995 [14]. c: HS-AFM of membrane protein diffusion in a synthetic membrane [18]. d and e: HS-AFM of conformational changes of an homolog of CNG channel in presence of cAMP and cGMP [19].

machine [19] (Figure 1.4 d and e). In the next section I will describe how AFM has been applied to real cell membranes.

1.3.2 Native cell membranes (from electron microscopy to AFM)

The question *"How does a real cell membrane look like?"* started to be answered only from the 70s when the first rudimentary technique to break the cells and to create membrane-only samples was developed [21]. Given the length-scale of the membrane features, the only microscopy technique available for their investigation was electron microscopy. This microscopy technique was extensively adopted in the following years, in particular thanks to a radical change in the preparation method that made the sample preparation more reliable: the use of sonic waves to break the cells to obtain the so called "unroofed" membranes [22]. From these investigations we learned how the membrane skeleton is arranged by looking directly into it from the cytoplasmic side of the membrane (Figure 1.5 a). For instance, it was possible to shed light on how the actin filaments arrangements partition the plasma membrane decreasing the lateral diffusion of lipids and proteins [23].

The versatility of AFM discussed also in the previous section comprises a relatively simpler instrument compared to the electron microscope and, more importantly, the possibility to operate at room temperature with the sample under the physiological medium. Despite of these theoretical advantages on paper, the AFM was applied to native membranes relatively late, and starting with special compartments of the cell constituted just by membrane (Figure 1.5 b). An example of these applications is the rod outer segment disc, key for vision and rich in Rhodopsin [24]. AFM was able to resolve the macromolecular

structures of Rhodopsin in discs that forms nano-domains with an average size of 500 nm2 [25, 26].

Only more recently, a group in Japan revisited the unroofing technique developed for electron microscopy [27] and used these samples, after fixation, with AFM obtaining molecular resolution at room temperature (Figure 1.5 c and d).

After having tested many of these methods, I can safely say that one of the major disadvantages of using AFM with native cell membranes is the fact that the position of the membrane itself is difficult to be found, and requires time consuming scanning of the sample that affect also the quality of the tip. For this reason, inspired by ref. [28], I developed un unroofing method that breaks only one single cell (or a few) on the very corner of a triangular coverslip [29] (Figure 1.5 e and f). In this way, the identification of the position of the membrane is straightforward, and the membrane seems to be isolated without the membrane skeleton that was observed with other techniques. The very last goal in this case would be to image single membrane proteins with sub-molecular resolution in their complex macromolecular organization, but not even the latest AFMs seem to be able to reach such a resolution on this dirty environment.

How the information coming from the topology of native membranes could be transferred to applications in nano-medicine is discussed in chapter 3.

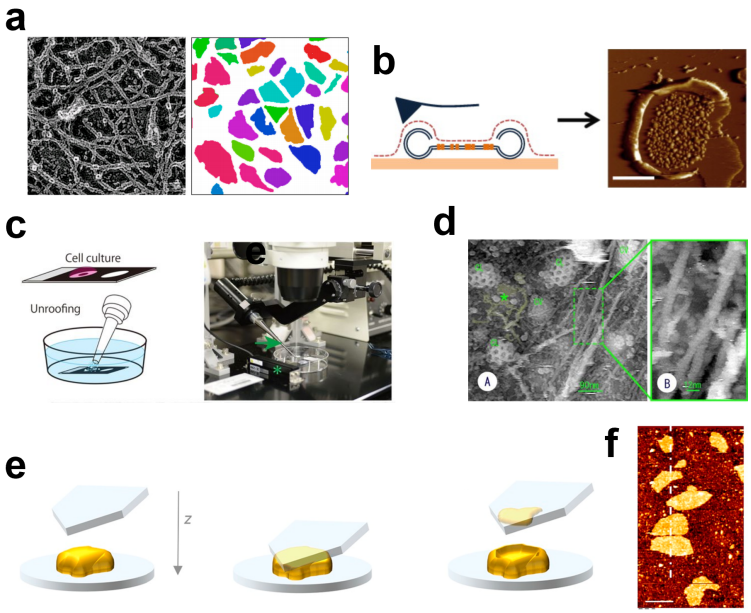

Fig. 1.5: a: electron microscopy of actin filaments that form boundaries on the membrane [23]. b: AFM imaging of rod outer segment discs [25]. c & d: unroofing preparation through sonic waves and AFM imaging of actin filaments and clatrin [27]. e & f: single cell unroofing through the gentle squeezing of a single cell and the resulting isolated membrane [29].

1.4 AFM as a force probe for cells and cell membranes

In the previous sections I discussed the imaging capabilities of the AFM, but we cannot forget that the AFM is also an instrument able to measure forces at the micro- and nano-scale level. In the next sections I will present the major results of the past two decades obtained with the application of AFM-based force spectroscopy to biological materials.

1.4.1 Single-cell force spectroscopy

Cells are soft objects that ranges from 1 to 50 microns in size. As opposed to inanimate objects, cells are active entities constituted by a complex internal structure, since they can duplicate and mix with other cells forming tissues, and finally organisms. The biochemical signals that the cells use to communicate and function have been the subject of investigation of molecular biology which made an enormous progress in the last 70 years. Different cell types are characterized by different biochemical signatures, and a question that one may ask is: *are different cells characterized by different mechanical properties?*

AFM can answer this question as the AFM tip can be used to indent a cell while recording the cantilever deflection. The recorded curve is informative of the cell stiffness and from the same curve it is possible to extrapolate conventional mechanical properties like the Young modulus [30]. There is a vast scientific literature on this topic which focused very early on the attempt to find biomedical applications, in particular for cancer cell detection [31,32]. The general conclusion of these studies is that cancer cells (lung, breast, pancreas [33], ovarian [32]) are softer and with a narrower standard deviation of the Young modulus compared to non-malignant cells of the same body cavity. Being softer may help cancer cells to be more dynamic and therefore successful in infiltrating tissues, but a definitive explanation of the problem is still to come.

More recently, people developed also some alternative operating mode to expand the range of mechanical properties that AFM can investigate. Yango el al. [34], for instance, introduced cycles of indentation and relaxation to measure both the Young modulus and the internal viscosity of the cell. An interesting advancement is the one introduced by Rigato et al. [35] where they measured the cell viscoelastic properties at different time scales, stimulating the cells from 1 Hz to 100 kHz. This is important because the cell is an active object which constituents (e.g. cytoskeleton filaments) can rearrange at different time scales, therefore defining the 'mechanical fingerprint' can help to sort cells more accurately.

Being able to uniquely identify cancerous cells (or specimens) just by probing their mechanics, so without the use of biochemical markers, seems to be a challenge that may be completed in relatively few years.

1.4.2 Nanomechanics of lipid bilayers: from synthetic to native membranes

The mechanical properties of the lipid bilayer—i.e. the component that separates the cell interior from the external environment—were not accessible with the standard biochemical techniques available until the invention of the AFM. AFM opened the way for the direct investigation of the strength of molecular interactions among lipids in supported membranes. In these experiments, synthetic lipids (e.g. DPPC, DOPC) are mixed in solution and deposited on atomically flat surfaces (e.g. cleaved mica), then they are imaged with AFM to confirm their correct assembly, and finally indented with the AFM tip to probe the nanomechanical properties of the membrane. The prototypical indentation curve recorded by the AFM shows an initial elastic behavior of the membrane (deformation of the bilayer), until the compression force of the AFM tip reaches a critical value that causes the breakage of the bilayer. After the breakage, the tip is retracted while the membrane self-assembles back, closing the hole.

To my knowledge, the first experiments on lipids nanomechanics were performed in 1999 by Dufrene et al. [36]: they demonstrated the versatility of AFM to probe the chemical and physical properties of lipid membranes. After these pioneering studies, many labs around the world started to apply atomic force microscopy to membranes, characterizing their behavior in many different conditions of physiological relevance. For instance it was shown that the stiffness of the membrane increases by reducing its temperature [37] or by increasing the percentage of cholesterol [38], with important consequences for our understanding of the dynamic of processes at cellular and sub-cellular level. It is surprising how, from relatively crude indentations and enough statistics, it is possible to extrapolate very detailed physical quantities of the bilayer like the line tension and the spreading pressure [39, 40], quantities that are essential in coarse grain simulations of the cell.

I would like to mention two noteworthy recent experimental advancements in the field. Goncalves et al. [41], instead of studying supported membranes, developed a substrate with sub-micrometric holes where the membrane could remain free-standing, emulating a real cell surface. In this way, they were able to precisely measure the breaking point of a membrane that could bend under the AFM tip push. While Al-Rekabi et al. [42], similarly to Rigato et al. [35] as described in the previous section, introduced a multifrequency AFM mode that allows to capture the viscoelastic properties of the membrane and demonstrates how cholesterol concentration is a key ingredient in changing membrane properties from viscous to elastic.

One of the goals of this thesis is to transfer the application of the powerful methods described above (and benchmarked with synthetic membranes) to native cellular membranes in order to gather information of the real nanomechanics generated by the native complexity.

1.5 AFM as a force probe for single proteins

Measuring the mechanical properties of cells or cell membranes is definitely a technological leap, but it does not represent a conceptual breakthrough, in the sense that these results could be somehow expected. What really represents a practical revolution for an unsolved problem in biology is the possibility to record the un-folding of single proteins—one at a time—with AFM-based single-molecule force spectroscopy (SMFS).

In fact, the physico-chemical process that guides a linear sequence of amino acids into the 3-dimensional precise structures that (almost-)every protein shows may be taken for granted, but it is a puzzle since the 50s [43]. The number of variables that should be taken into account to simulate with atomic resolution the folding of a protein is simply intractable for modern computational power, and therefore, in the past years many computational "shortcuts" have been invented to tackle the problem in an approximate manner (e.g. [44]). On the other hand, from the experimental point of view, the only way to study protein folding and unfolding was by chemical denaturation [45], thus at the ensemble level and not at the single-molecule level. There was no certain mechanistic understanding of how the dynamics of protein folding should work.

This is the context where SMFS, starting from the late 90s, revolutionized the way people study protein folding. The experimental setup consists in a AFM cantilever tip that, instead of being used for imaging as discussed in section 1.3.1, is approached and retracted form a flat sample onto which many copies of the same protein of interest were deposited. The AFM tip push the sample and binds one of the terminus end of the underlying protein. Then the tip is retracted while recording the force experienced by the cantilever, so that it is possible to form a force vs distance spectrum (F-D curve). If the other terminus of the protein is bounded to the sample surface, the tip will literally stretch the protein, forcing it to denaturate. The prototypical unfolding curve of a sequence of immunoglobulin domains was observed for the first time by Rief et al. in 1997 [46] (Figure 1.6 a) showing the so called saw-tooth like shape, i.e. a sequence of rising phases followed by vertical jumps to the baseline at zero-force.

How can we describe this behavior? The rising phases can be fitted with the worm-like chain model, i.e. a model developed in polymer physics that describes the stretching of an ideal semi-flexible chain [48]. The sudden jump to zero-force are instead representative of the abrupt unfolding of a complete protein domain, and this was unexpected. The unfolding of the protein does not happen in a continuous way, but rather in a all-or-none fashion. This two-state behavior (folded vs unfolded) is typical for the majority of globular proteins investigated so far, e.g. GFP, Xylanase, Fibronectin and many others [49]. Moreover, these globular proteins tends to fold back into their original 3D structure even in vitro [46].

Membrane proteins, and in particular trans-membrane proteins are topologically very different from globular proteins because, instead of being fully immersed in the cytosol, they perform their function embedded in the cell membrane. They are also more difficult to be studied since they are laborious to be

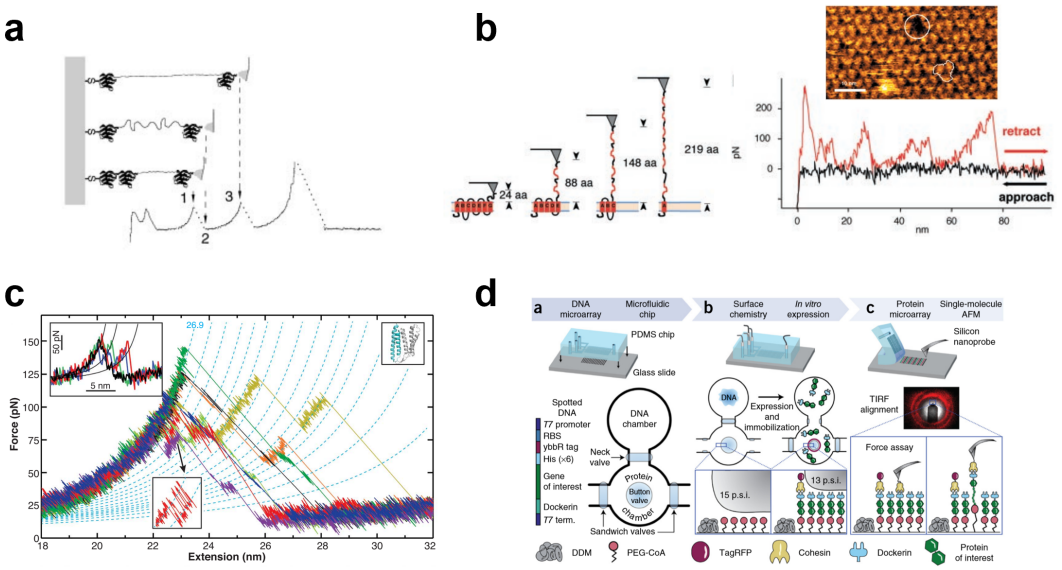

Fig. 1.6: a: unfolding curve of a tandem of globular protein [46]. b: unfolding curve of a trans-membrane protein [47] and AFM image of the membrane after unfolding. c: hidden unfolding intermediates resolved with special AFM probes [55]. d: microfluidic-AFM platform to express proteins and to probe them with SMFS [49].

purified and they don't crystallize well (it is often necessary to study homologous proteins that are easier to be handled). The fact that they operate across the membrane introduces an additional complex ingredient to the problem of folding, indeed it was discovered that trans-membrane proteins needs the help of other proteins (translocon) to be correctly folded into the membrane [50].

SMFS have what it takes to be very powerful when applied to membrane proteins, possibly being informative also of membrane protein structure. The first experimental observation dates back to the year 2000 when Oesterhelt et al. [47] used AFM-based SMFS to unfold bacteriorhodopsin. The unfolding curve of bacteriorhodopsin (see Figure 1.6 b) resembles the unfolding of a tandem of globular proteins (Figure 1.6 a) but it has a slightly different interpretation. As opposed to what happens to the majority of globular proteins that unfold in an all-or-none fashion, in bacteriorhodopsin the different domains unfold separately and consecutively, one after the other. A general empirical observation is that these domains correspond to pairs of alpha helices (or beta hairpin). This observation is actually quite robust given that further studies of other membrane proteins tend to support this empirical "rule", also in beta-barrel membrane proteins: aquaporin [51], sodium-proton antiporter [52], FhuA [53], etc. The unfolding behavior of membrane proteins is somehow reminiscent of the mechanistic intuition of how these proteins should exit the membrane when pulled. However, thanks to a recent improvement in resolution of the AFM probes, it has been shown that the single and separated peaks of unfolding that was reported in the past, and that corresponds to the unfolding of pairs of alpha helices, are actually decorated by a rich series of minor unfolding events indicating that the complexity of the process is still highly unresolved [55] (Figure

1.6 c).

With SMFS it is possible to test not only the detailed physics of folding, but also to obtain biological insights on the structure-function of specific proteins, both related to folding or not. An example is the work by Serdiuk et al. where they directly observed the action of chaperon proteins acting on membrane proteins that were previously unfolded, showing that without the help of these chaperons, a membrane protein cannot autonomously fold back into the membrane [56].

In the previous paragraphs I described how SMFS can be used to explore the problem of protein folding, but I strongly believe that the major applications of SMFS are to problems at the intersection with biomedicine. SMFS can be exploited to investigate proteins behaviors where other techniques cannot be applied. I will now report some applications in this direction. One way to use SMFS to tackle a biomedical problem is to study the differences of a membrane protein and a mutated one that may be involved in a disease. Kawamura et al. [58] took a similar direction studying the differences between rhodopsin and opsin, which is the same protein not bounded to the chromophore that enable vision. In this case they detected slightly differences in the unfolding behavior, showing that SMFS can resolve these changes. Another approach is to study the mechanical differences induced by the binding of a ligand to a membrane protein, and how it affect the structure [59]. But what seems a highly unexplored area of research is the one touched by Otten et al. [49] (Figure 1.6 d), i.e. trying to change the scale and the throughput of the SMFS experiments. They developed an interesting platform that can express proteins in vitro, and then screen them in order to create a SMFS resource to test the most various hypothesis related to protein mechanics or folding, for instance malfunction due to misfolding.

In chapter 2 I will present the experimental results of my PhD work which primary goal was to study the unfolding of membrane proteins in native membranes, but that turned out to require also the development of special experimental and computational techniques. In chapter 3 I will discuss the conclusions of the thesis.

Chapter 2

Results

In this chapter are presented the research papers that contains the results of my PhD work. I substantially contributed to the design and to the writing of all these articles.

1. In the first article *Fodis: Software for Protein Unfolding Analysis* [60] I developed a software for the analysis of Force-Distance curves that represent the unfolding of single proteins, either pulled by AFM or optical tweezers. The software was also released to the public on the GitHub repository.

2. In the second article *Single-cell unroofing: probing topology and nanomechanics of native membranes* [29] I invented a technique to break and isolate the cell membrane of single cells, in order to probe the cell membrane with Atomic Force Microscopy.

3. In the third article *Automatic classification of single-molecule force spectroscopy traces from samples containing heterogeneous mixtures of proteins* I contributed to the design of a pipeline that allows to identify the recurrent protein unfolding curves within a dataset, without knowing in advance the number and the shape of these unfolding curves.

4. In the fourth article *Unfolding and identification of membrane proteins from native cell membranes* [61] I performed AFM-based SMFS experiments on native cell membranes isolated from neurons. By the cross-matching of proteomic databases (ProteomeXchange, Uniprot, PDB), I proposed and verified a Bayesian inference method to find the identity of the Force-Distance curves generated during the experiments. I also proved that the combination of SMFS and the automatic data selection that we developed generates proteomic information comparable to the Mass Spectrometry performed on the same cell types, but with several order of magnitude fewer cells (1:1,000,000).

Biophysical *Journal*
Computational Tool

Biophysical Society

Fodis: Software for Protein Unfolding Analysis

Nicola Galvanetto,[1,*] Andrea Perissinotto,[1] Andrea Pedroni,[1] and Vincent Torre[1,2,3]
[1]International School for Advanced Studies (SISSA), Trieste, Italy; [2]Cixi Institute of Biomedical Engineering, Ningbo Institute of Materials Technology and Engineering, Chinese Academy of Sciences, Zhejiang, People's Republic of China; and [3]Center of Systems Medicine, Chinese Academy of Medical Sciences, Suzhou Institute of Systems Medicine, Suzhou Industrial Park, Suzhou, Jiangsu, People's Republic of China

ABSTRACT The folding dynamics of proteins at the single-molecule level has been studied with single-molecule force spectroscopy experiments for 20 years, but a common standardized method for the analysis of the collected data and for sharing among the scientific community members is still not available. We have developed a new open-source tool—Fodis—for the analysis of the force-distance curves obtained in single-molecule force spectroscopy experiments, providing almost automatic processing, analysis, and classification of the obtained data. Our method provides also a classification of the possible unfolding pathways and the structural heterogeneity present during the unfolding of proteins.

INTRODUCTION

The investigation of proteins has been greatly advanced from the recent technical improvements of cryo-EM, which have allowed the determination of the structure of many proteins by avoiding the bottleneck of crystallization (1). However, fundamental single-protein properties, such as their folding and/or unfolding dynamics and structural heterogeneity, have to be addressed with other experimental methods like single-molecule optical methods (single-molecule fluorescence and single-molecule fluorescence resonance energy transfer) or single-molecule force spectroscopy (SMFS) (2). SMFS is an application of atomic force microscopy and of optical tweezers (Fig. 1, *A* and *B*) in which the force F required to unbind a ligand or unfold a polymer is measured as a function of the length *d* at piconewton and nanometer resolution. The obtained force-distance (*F-d*) curves are composed of a series of force peaks characterizing the unfolding of structural segments. A force peak occurs during the unfolding of an α-helix and/or β-sheets followed by an unfolded segment. When a protein changes its conformation, the force peaks of *F-d* curves change their location and amplitude; from these changes, structural information of the molecular rearrangements is obtained. The location of a force peak is obtained by fitting the experimental *F-d* curve with the worm-like chain model, providing the values of the contour lengths (Lc). From the value of the Lc, it is possible to estimate the number of amino acids of the segment unfolded between the occurrence of two consecutive force peaks, and to probe its structural heterogeneity from the distribution of the force peaks at different pulling rates (3).

Recent improvements allow the collection of more data and with higher quality (4), but there is no universal ready-to-use data sharing platform for the analysis of obtained *F-d* curves. Several algorithms to reduce manual intervention have been published (5–7), but the analysis has not been fully automated yet and still requires a significant amount of decisions to be taken by the researcher.

We developed Fodis (force-distance software) (Fig. 1 *C*), an open-source software providing an all-in-one environment with several tools for the analysis of *F-d* curves from raw curves to data representations and, to our knowledge, novel analytical methods.

MATERIALS AND METHODS

Fodis filters the *F-d* curves according to a few set parameters (Figs. S1 and S2) that consist mainly of the expected distance of the fully stretched molecule (i.e., Lc-maximum). Fodis aligns automatically filtered *F-d* curves (Figs. 2 *A* and S3) and provides a thorough statistical characterization of their variability (Fig. 2, *B* and *C*; Fig. S4). Filtered *F-d* curves with similar values of Lc-maximum are heterogeneous, but Fodis

Submitted August 11, 2017, and accepted for publication February 6, 2018.

*Correspondence: nicola.galvanetto@sissa.it

Nicola Galvanetto and Andrea Perissinotto contributed equally to this work.

Andrea Pedroni's present address is Department of Neuroscience, Karolinska Institutet, Stockholm, Sweden.

Editor: Andreas Engel.

https://doi.org/10.1016/j.bpj.2018.02.004

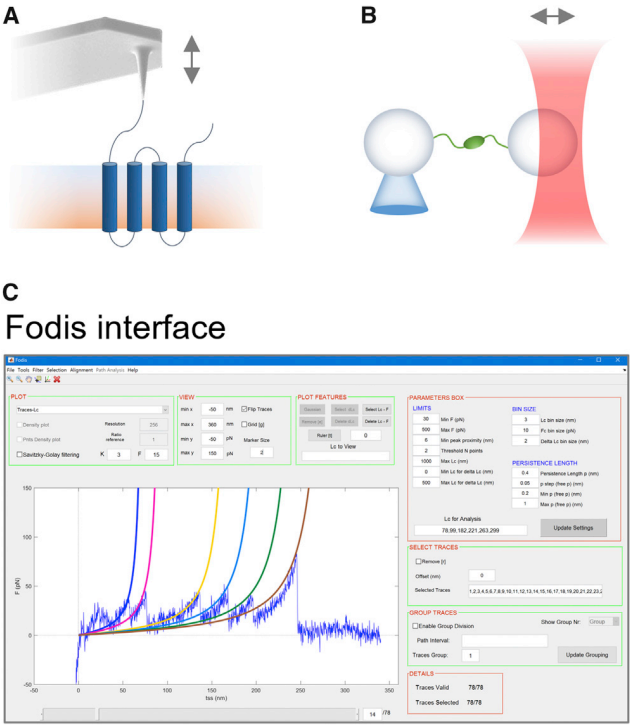

FIGURE 1 Cartoon of an SMFS experiment based on (*A*) AFM and (*B*) optical tweezer. (*C*) An example of the graphic user interface of Fodis is shown. To see this figure in color, go online.

identifies clusters of similar *F-d* curves with similar force peaks. These clusters, depending on the experiment under consideration, correspond to the unfolding of different molecules, to the same molecule in different states, or to different unfolding pathways (Fig. 2 *E*; Fig. S5). Fodis can open raw data files from different atomic force microscope manufacturers (JPK Instruments, Carpinteria, CA; Bruker Instruments, Billerica, MA) and also the ASCII matrices of *F-d* values (Supporting Materials and Methods). The software is designed to assist the user in the most common and critical steps with a reversible workflow, allowing the user to keep track of the original information. Fodis can save working sessions, export curve selections, and extract graphical data representations.

RESULTS AND DISCUSSION

As a testbed, we processed *F-d* curves obtained from SMFS experiments on oocyte membranes after the overexpression of the cyclic nucleotide-gated CNGA1 channels (8) (Supporting Material). On a typical notebook computer (4 GB memory, 2.0 GHz central processing unit), Fodis loads 1000 *F-d* curves in 5 s and performs a filtering routine in less than 20 s. Filtering depends on the type of analyzed data, and in Fig. S2, results from a 1-day experiment are presented. *F-d* curves selected from several experiments can be automatically aligned for statistical analysis; for this purpose, we implemented the method developed by Bosshart et al. (7) with some modifications (see Fig. S3 and Supporting Materials and Methods). All *F-d* curves are coded as strings into a global matrix (GM), a binary representation of the position of detected force peaks (see Fig. 2 *D*). From the GM, different statistical tests and graphical representations are generated, and users can integrate new and ad hoc analyses and tests. The global histogram of maxima (Fig. S4) counts the frequency of occurrence of force peaks with a value of Lc in a given range. The global histogram of maxima can be fitted by a multi-Gaussian distribution to identify the most probable Lc positions of unfolding events. Fodis creates cumulative scatterplots of peak populations that can be selected on the basis of their position (Lc) or force and then individually analyzed to extract force and position distributions (Fig. 1, *B* and *C*). The Lc-ΔLc plot shown in Fig. 1 *B* is an example of how we can extract information about the periodicity of peak occurrence from the GM (Fig. 2 *D*).

Fodis allows also the identification of different clusters of *F-d* curves (path plot: Figs. 1 *E*, S5, and S6) by coding *F-d* curves on the basis of the number of force peaks and their corresponding value of Lc. The path plot algorithm is used for a graphical representation of different unfolding pathways, generalizing previous methods for unfolding-pathway determination and selection presented by Schönfelder et al. (9), Yu et al. (2), or Thoma et al. (10).

CONCLUSIONS

In Fodis, we implemented relevant published and, to our knowledge, new algorithms for SMFS analysis. Fodis provides a toolbox to the SMFS community for the development and sharing of analytical methods in an all-in-one open-source software. It has been developed to meet the needs of a broad audience, both for researchers with no programming skills and for those who could contribute to Fodis's future versions.

Software availability

Fodis is available under the Apache License, version 2.0. Source code, executables, datasets, and full documentation are available for download from GitHub at https://github.com/nicolagalvanetto/Fodis. The latest release, version 1.2, is archived in Zenodo: Digital Object Identifier: 10.5281/zenodo.841277.

SUPPORTING MATERIAL

Supporting Materials and Methods, six figures, and one data file are available at http://www.biophysj.org/biophysj/supplemental/S0006-3495(18)30207-8

AUTHOR CONTRIBUTIONS

N.G. conceived the project, developed the algorithms, wrote part of the code, and wrote the manuscript. A. Perissinotto developed the algorithms

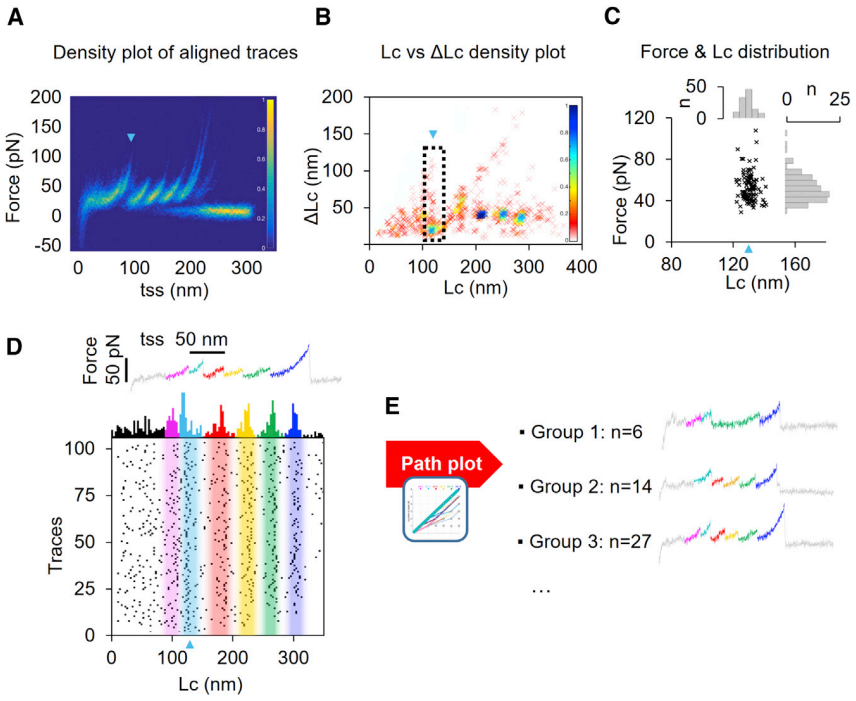

FIGURE 2 (*A*) Superimposition of 104 *F-d* curves as a density plot, after the automatic alignment (Fig. S3). (*B*) A scatterplot shows all detected peaks from the population of the 104 curves. The *x*-dimension is the contour length (Lc), and the *y*-dimension reports the difference between the considered peak and the previous force peak (ΔLc). Point density is color coded according to the bar on the right. (*C*) A scatterplot shows the unfolding events between 120 and 140 nm (*triangle* in *A*) and the histograms of force and Lc distribution. (*D*) At the top, a representative *F-d* curve is shown. At the bottom, a cumulative histogram counts the number of peaks along the Lc coordinate and the global matrix (an $N \times B$ matrix, where N is the number of traces (rows), and B is the number of bins along the Lc coordinate. Detected peaks are here plotted as *black pixels*). Colors identify the different unfolding groups. (*E*) The path plot algorithm (Figs. S5 and S6) splits the population of curves in homogeneous groups representing different unfolding pathways. tss, tip sample separation. To see this figure in color, go online.

and wrote the code. A. Pedroni helped in developing the software. V.T. conceived the project and helped in writing the manuscript. All the authors read and approved the final article.

ACKNOWLEDGMENTS

The authors thank Dr. Sourav Maity for data collection and Paolo Fabris for the initial technical support. The authors thank Manuela Lough for checking the English of the manuscript. The authors thank Dr. Michele Allegra and Dr. Giampaolo Zuccheri for useful discussions.

V.T. recognizes the support from the 3315 Project of Ningbo/Cixi, Zhejiang province, China.

SUPPORTING CITATIONS

References (11–18) appear in the Supporting Material.

REFERENCES

1. Bai, X., G. McMullan, and S. H. Scheres. 2015. How cryo-EM is revolutionizing structural biology. *Trends Biochem. Sci.* 40:49–57.
2. Yu, H., M. G. Siewny, …, T. T. Perkins. 2017. Hidden dynamics in the unfolding of individual bacteriorhodopsin proteins. *Science.* 355:945–950.
3. Hinczewski, M., C. Hyeon, and D. Thirumalai. 2016. Directly measuring single-molecule heterogeneity using force spectroscopy. *Proc. Natl. Acad. Sci. USA.* 113:E3852–E3861.
4. Otten, M., W. Ott, …, H. E. Gaub. 2014. From genes to protein mechanics on a chip. *Nat. Methods.* 11:1127–1130.
5. Marsico, A., D. Labudde, …, M. Schroeder. 2007. A novel pattern recognition algorithm to classify membrane protein unfolding pathways with high-throughput single-molecule force spectroscopy. *Bioinformatics.* 23:e231–e236.
6. Puchner, E. M., G. Franzen, …, H. E. Gaub. 2008. Comparing proteins by their unfolding pattern. *Biophys. J.* 95:426–434.
7. Bosshart, P. D., P. L. Frederix, and A. Engel. 2012. Reference-free alignment and sorting of single-molecule force spectroscopy data. *Biophys. J.* 102:2202–2211.
8. Maity, S., M. Mazzolini, …, V. Torre. 2015. Conformational rearrangements in the transmembrane domain of CNGA1 channels revealed by single-molecule force spectroscopy. *Nat. Commun.* 6:7093.
9. Schönfelder, J., R. Perez-Jimenez, and V. Muñoz. 2016. A simple two-state protein unfolds mechanically via multiple heterogeneous pathways at single-molecule resolution. *Nat. Commun.* 7:11777.
10. Thoma, J., N. Ritzmann, …, D. J. Müller. 2017. Maltoporin LamB unfolds β hairpins along mechanical stress-dependent unfolding pathways. *Structure.* 25:1139–1144.e2.
11. Savitzky, A., and M. J. E. Golay. 1964. Smoothing and differentiation of data by simplified least squares procedures. *Anal. Chem.* 36:1627–1639.
12. Marko, J. F., and E. D. Siggia. 1995. Statistical mechanics of supercoiled DNA. *Phys. Rev. E Stat. Phys. Plasmas Fluids Relat. Interdiscip. Topics.* 52:2912–2938.
13. Carrion-Vazquez, M., A. F. Oberhauser, …, J. M. Fernandez. 2000. Mechanical design of proteins studied by single-molecule force spectroscopy and protein engineering. *Prog. Biophys. Mol. Biol.* 74:63–91.
14. Oesterhelt, F., D. Oesterhelt, …, D. J. Müller. 2000. Unfolding pathways of individual bacteriorhodopsins. *Science.* 288:143–146.
15. Celik, E., and V. T. Moy. 2012. Nonspecific interactions in AFM force spectroscopy measurements. *J. Mol. Recognit.* 25:53–56.
16. Amestoy, P., T. Davis, and I. Duff. 1996. An approximate minimum degree ordering algorithm. *SIAM J. Matrix Anal. Appl.* 17:886–905.
17. Kawamura, S., M. Gerstung, …, D. J. Müller. 2013. Kinetic, energetic, and mechanical differences between dark-state rhodopsin and ppsin. *Structure.* 21:426–437.
18. Akaike, H. 1974. A new look at the statistical model identification. *IEEE Trans. Automat. Contr.* 19:716–723.

Biophysical Journal, Volume *114*

Supplemental Information

Fodis: Software for Protein Unfolding Analysis

Nicola Galvanetto, Andrea Perissinotto, Andrea Pedroni, and Vincent Torre

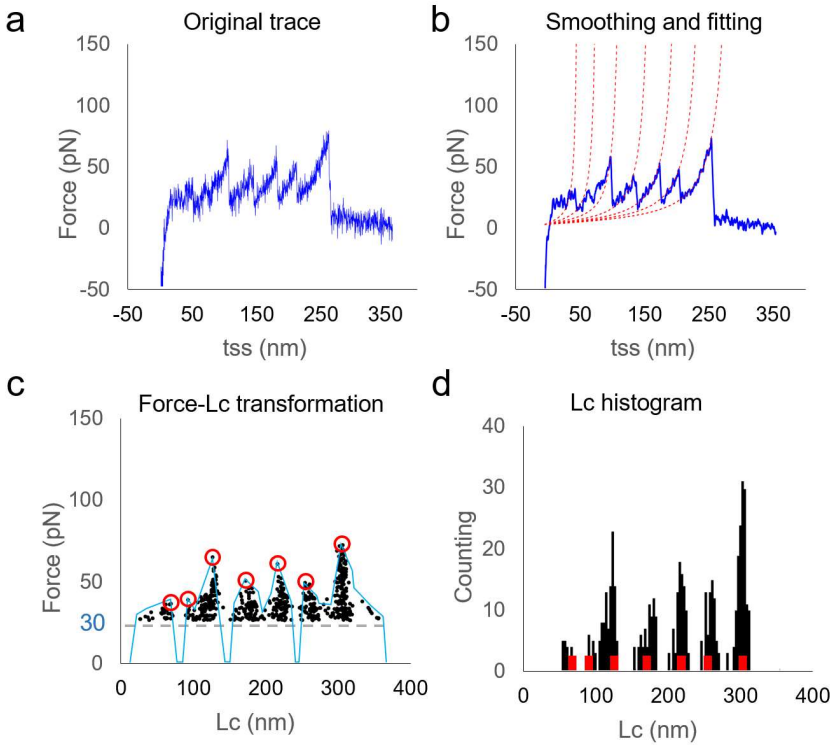

Supplementary Figure 1

Preprocessing of F-d curves

(a) Example of a Force-distance curve (F-d) obtained by a commercial AFM (JPK), representing the relation between the force exerted by the cantilever tip vs tip-sample-separation (tss). (b) the same curve after smoothing with Savitzky-Golay (1) filter, which preserves discontinuity. This filter reduces noise enhancing peaks detection. Dotted red lines: fit of the rising phases of the curve with the Worm-like chain (WLC) model (2) (fixed persistence length p=0.4 nm and free contour length (Lc), see equation (1) in Supplementary Note 2 for more details). (c) Transformation of the F-d curve in the (F,Lc) plane using equation (2) in Supplementary Note 2. Only points with a value of F larger than 30 pN were considered. The cyan line is the Force Profile, and it is used for the automatic detection of the peaks (see Supplementary note 2). (d) Histogram of the values of Lc shown in (c), also called “barrier position histogram”(3). Red bars represent the position of detected peaks.

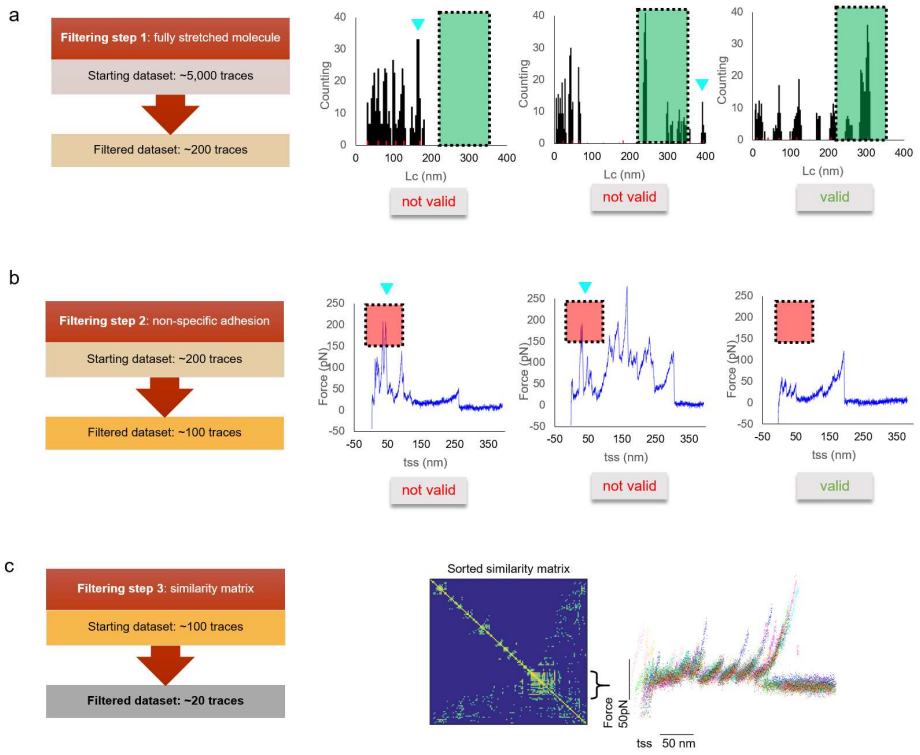

Supplementary Figure 2

Automatic filtering of F-d curves

(a) starting from a dataset of ~10,000 curves (Supplementary data), 3 steps are used to find the appropriate curves. *Filtering step 1* tests the fully stretched condition (i.e. the total length of the primary structure of the protein). This condition excludes curves that are longer or shorter than expected value of Lc. The length of the trace corresponds to the position of the last peak in the contour length histogram (Fig S1 d). The *expected length* of a protein is equal to the number of amino acids (N of a.a.) times the single a.a. length (~0.4 nm (4)). The *measured length*, estimated in the in the contour length histogram, highly depends on the value of persistence length (p; commonly set to 0.4 nm (5)), but which can vary between 0.3 nm and 0.8 nm (4). Because of all these uncertainties, we suggest to use a filtering window centered in the value of the *expected length*, and large at least ±30% of that value. The expected length for the CNG channel is ~280 nm (690 a.a. x 0.4 nm). The green window in (a) is 210-360 nm and determines the Lc region within which the trace must end. The *filtering step 1* is intended to be a coarse tool for excluding curves with a wrong length.
(b) *filtering step 2* discards curves that display high non-specific adhesion at the very beginning of the unfolding (curves with forces over 150 pN in the first 70 nm were discarded (6)).
(c) *filtering step 3* finds groups of similar curves. We define *similarity* as the value of cross correlation between the contour length histograms (Fig. S1 d) of two curves (see Supplementary note 3, equation 3). If *N* is the number of curves, a symmetric *N* x *N similarity matrix* is formed containing all the correlation values for each couple of curves. The resulting matrix is ordered with the symmetric approximate minimum permutation algorithm(7) (symamd MATLAB function) to obtain clusters of similar curves. Those clusters can be opened, inspected, and compared with a candidate trace or with control experiments. More details about the *similarity matrix* can be found in the user guide of the software.

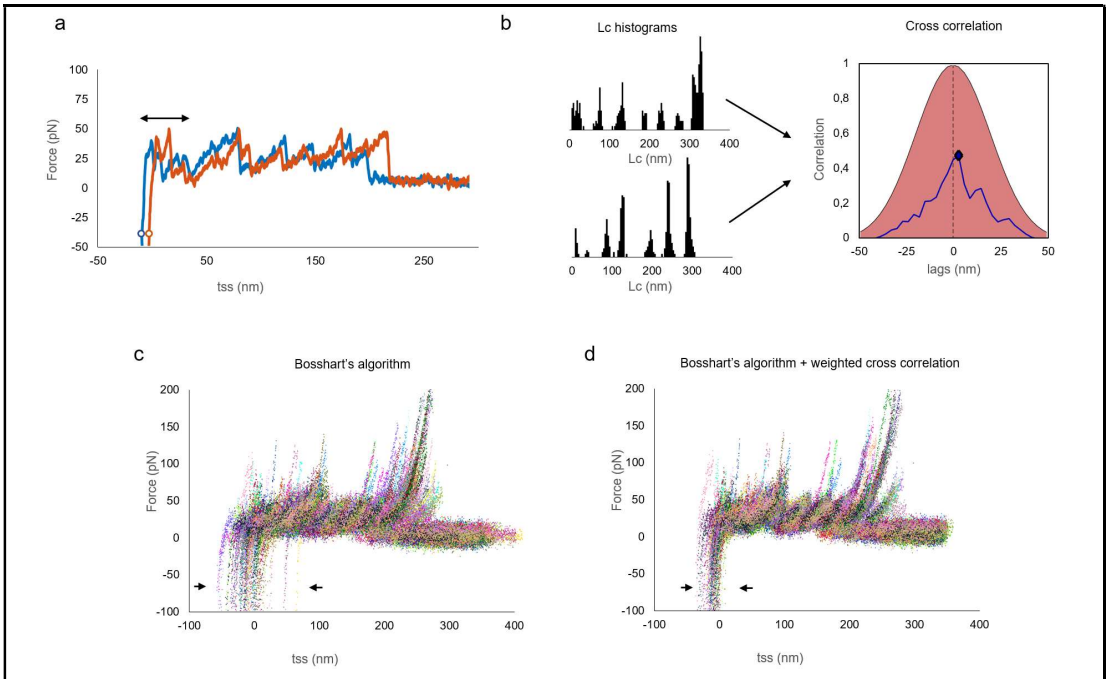

Supplementary Figure 3

Automatic alignment

(a) example of 2 misaligned curves. White circles indicate the *zero* of the of the tss (i.e. the z-position of the sample). (b) cross-correlation curve (blue line) between two contour length histograms. The maximum value of the correlation is highlighted by the blue diamond at lag=+2 nm; the vertical dotted line is positioned at 0 lag (i.e. where the *zeros* of the two curves coincide). The Gaussian distribution (red area) weights the cross-correlation curve (see Supplementary note 3, equation (3) and (4)). (c) superimposition of 106 curves automatically aligned with original Bosshart's algorithm (8). This algorithm does not prevent curves to be shifted from the origin by excessive large values. (d) the same superimposition automatically aligned with Bosshart's plus the weighted correlation curve (b) and in this way large shifts are reduced and almost eliminated.

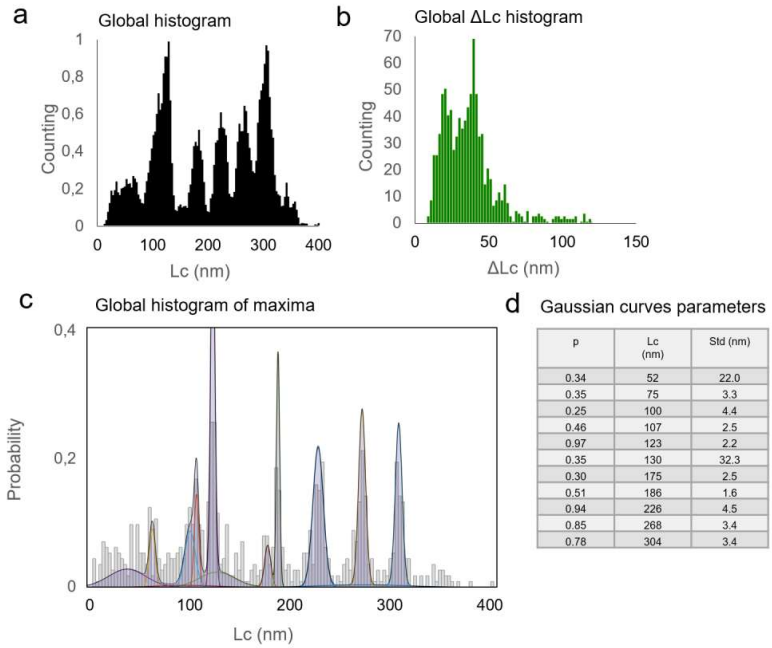

p	Lc (nm)	Std (nm)
0.34	52	22.0
0.35	75	3.3
0.25	100	4.4
0.46	107	2.5
0.97	123	2.2
0.35	130	32.3
0.30	175	2.5
0.51	186	1.6
0.94	226	4.5
0.85	268	3.4
0.78	304	3.4

Supplementary Figure 4

Analysis of the distribution of contour lengths (Lc)

Statistical analysis of selected curves. (a) The Global Histogram is the sum of all Lc histograms (Supp. Fig. 1d) normalized to the maximum bin value. The peak sharpness indicates a high homogeneity of F-d curves. (b) Global ΔLc histogram counts all increase of the values of Lc between two consecutive peaks. (c) Global histogram of maxima counts the values of the Lc of all detected peaks. The distribution can be fitted with multi Gaussians to determine the position and frequency of persistent unfolding events (see Supplementary Note 4 for the Gaussian mixture model). (d) probability, contour length (Lc) and standard deviation of the Gaussian curves displayed in (c).

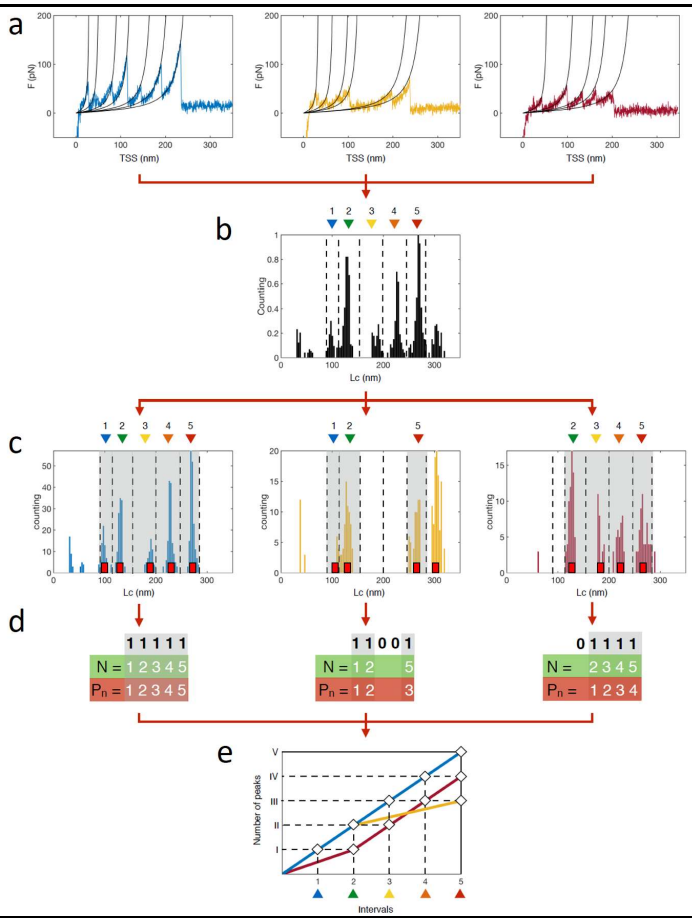

Supplementary Figure 5

Pathplot construction

The Pathplot is generated in 5 steps and is used to find clusters of curves with force peaks with similar values of Lc. (a) Curves are fitted with the WLC model, transformed into Lc histograms and grouped in the Global Histogram as described in Figure S4 a. (b) The Global Histogram is divided in intervals according to the ensemble of events so to obtain a partition of the Lc coordinates in regions with distinct maxima. (c) Following the aforementioned rule, in this explanatory panel, we selected 5 intervals corresponding to the intervals 90-118,118-155,155-200,200-247,247-285 nm. (d) On the basis of this division, each trace is coded in a binary string of 5 digits: 0 is assigned if no force peak is detected within the interval, 1 is assigned if at least one event is detected. From each string, we created two additional sequence: # and Pn. # is the sequence referred to the order of appearance of the force peak along the trace (in a trace with 2 peaks, the 1st peak has #=1 and the 2nd peak has #=2). Pn refers to the interval position occupied by a peak (a peak that fall within the 3rd interval has Pn=3). (e) Coded curves are plotted as broken lines into an orthogonal #-Pn space, the line-width is proportional to the number of curves that follow the same path.

This algorithm generalizes the previous proposed methods (9, 10) providing a representation able to distinguish different unfolding behaviors/clusters of a given set of curves, based on the number and position of occurrence of unfolding events.

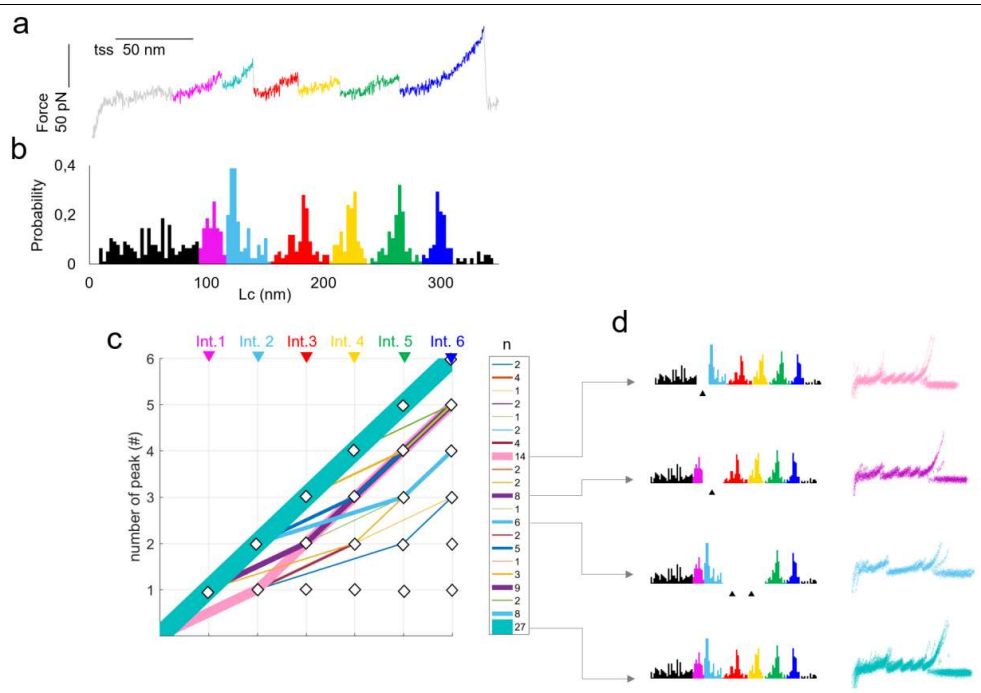

Supplementary Figure 6

Pathplot of CNGA1 curves

(a) a F-d curve from the unfolding of CNGA1 channels (11). (b) Global Histogram of Maxima (Fig. S1 d) applied to the population of 106 curves of CNGA1 (Supplementary dataset). The major peaks of the histogram are highlighted with different colors. (c) the Pathplot applied to this set of curves with Lc intervals congruent with (b): 90-118,118-155,155-200,200-247,247-285,285-320 nm. The legend on the right shows the number of curves belonging to the different pathways. (d) examples of identified clusters with the corresponding set of F-d curves and the Lc histograms.

Supplementary notes

Note 1

Data Import

Fodis has been designed to open raw data files from JPK and Bruker. To allow other users to operate with Fodis, but also to facilitate the portability of datasets, it can load (and export) data in ASCII format as explained in the User Guide section 1.2.

Open Samples

The open samples option opens .jpk-force raw files and .txt files generated by JPK's Data Processing software.
The open samples option opens .spm, .xyz (e.g. .084, .017 etc.) raw files and .txt generated by Bruker's NanoScope (more details can be found in the User guide section 1.2.2). Support for other formats can be requested at the dedicated section of the web site https://github.com/nicolagalvanetto/Fodis/issues.

Import Curves

Fodis imports *.txt* files of space separated numbers. The files should be organized in columns of Force and Distance values. *F1 X1 F2 X2 F3 X3 … FN XN* is the order of the columns, where *F1* is the first trace Force values, *X1* is the tip sample separation of the first trace and so forth until the N-th trace. For more details check the User Guide section 1.2.1 and the **Supplementary data** files.

Note 2

Curves pre-processing, curves transformations and peaks detection

-Pre-processing

Force-distance curve in Fodis must have in the x-axis the Tip Sample Separation in meters (TSS) with the contact point on the left, and in the y-axis the force in Newton (baseline corrected).

The imported data may not be already formatted for the analysis (wrong units, TSS transformation needed, etc). The tool **Absolute height to TSS** has been developed for this scope. It can perform 6 different types of transformations:

- Geometrical Adjustment: the mirroring option inverts the values of the Force. The rotation option swaps the coordinates.
- X-axis Adjustment: the x-axis values are multiplied by the constant Height multiplier (which is automatically read in the import files when present). This is necessary when the imported files contain only the non-corrected Height channel (e.g. in JPK files)
- Y-axis Adjustment: if the vertical deflection of the cantilever is imported in Volts, the curves need to be rescaled with the *Sensitivity constant* and the *Spring constant*. If the vertical deflection of the cantilever is imported in meters, the curves need to be rescaled with the *Spring constant*. (The constants are automatically read in the imported files when present).
- Subtract Baseline: if the Force values need to be vertically shifted, this option finds the baseline averaging the final part of the curve (red patch in the tool). The starting point and the ending point of the patch can be changed in the edit boxes.
- Find contact point: it finds the first positive value.
- From piezo height to TSS: it transforms the x-coordinate in tip sample separation (TSS). (The constant is automatically read in the import files when present).

-WLC-based transformations

F-d curves were first smoothed with Savitzky–Golay filter to reduce white noise (**Fig. S1 b**). Smoothed F-d curves were converted into a plot of force and contour lengths (F, Lc) (3, 8) (**Fig. S1 c**). The Worm-like chain approximate equation used to perform curves transformation is (2):

$$\frac{Fp}{k_bT} = \frac{1}{4}\left(1 - \frac{d}{L_c}\right)^{-2} - \frac{1}{4} + \frac{d}{L_c} \quad (1)$$

Here, the contour length is represented by *Lc*, the persistence length by *p*, the extension is represented by *d*, the external force is represented by *F*, and k_b and *T* are the Boltzmann constant and the absolute temperature. A persistence length (*p*) of 0.4 nm was used to compute the Lc value for each corresponding tip-sample separation (*d* or TSS) value, by solving the third order polynomial:

$$4\lambda 3 + \omega\lambda 2 - 1 = 0 \quad (2)$$

where $\lambda = 1 - d/Lc$ and $\omega = 4F(d,Lc)/\alpha - 3$ and $\alpha = k_bT/p$. This equation had three roots and the root of interest was the real root λ^* such that $0 < \lambda^* < 1$. In this manner, each point of the F-d curve (F, d) was transformed into a corresponding point (F, Lc), and each F-d curve was transformed into an (F, Lc) plot (**Fig. S1 c**). Owing to this transformation, each portion of the F-d curve that was fitted perfectly by a constant Lc in the WLC model was mapped to a perfect vertical segment. The transformation of an F-d curve was therefore a relation (set of point) in the (F, Lc) plane rather than a function in the plane, and it was also not a continuous curve. Given the F-Lc values, the histogram of the counts/bin of Lc values (Lc histogram) was computed (**Fig. S1 d**). The Lc axis of the (F, Lc) plot was first divided into bins. All points with a value of F larger than 30 pN were counted in the corresponding bin and summed.

-Peaks detection

The automatic detection of peaks (i.e. unfolding events) was done operating on the Contour length (Lc, Fc) plot (**Fig. S1 c**). A Force Profile is created dividing the Contour length (Lc, Fc) in bins, and taking the maximum force value in each bin. Then, Fodis uses the MATLAB function *findpeaks( )* on the Force Profile, and it detects **every** maxima of the profile. Fodis allows to tune the Force Profile operating on the *smoothing*, on *threshold N points* (i.e. number of points to neglect for each bin) and the *minimum peak proximity* (see user guide, section 1.5.4). The default parameters are optimized to detect the force peaks of the CNG unfolding trace. A shorter F-d curve will require a smaller *minimum peak proximity.* Binary strings containing the information of peaks position are plotted as red bars in Lc histogram view (**Fig. S1 d**) and are grouped together in the Global Matrix (**Fig. 1 e** of the main text).

Note 3

Cross-correlation and automatic alignment

F-d curves to be compared to each other may require horizontal alignment. The main cause of the lateral shift are the different attachment points between the protein terminus and the tip, but also other effects may be present. Bosshart and colleagues (8) developed a reference free alignment method consisting of 4 steps. Starting from the contour length histogram of every trace (**Fig. S1 d**), they:

- subdivided the curves into groups of homogeneous curves (i.e. curves with the same number of peaks);
- recursively aligned curves into the same group with the maximum correlation principle, building an average contour-length reference for each group;
- formed a global reference (**Fig. S3 c**);
- aligned all the curves of the dataset to the global reference.

This procedure is suitable for identical globular multidomain proteins where force peaks generally occurred within conserved Lc values. Instead, in the case of soluble and complex proteins or membrane proteins, the occurrence of unfolding events may be variable due to the stochastic nature of the process, or because of the multiplicity of the unfolding pathways that may be accessed by the protein. For this reason, we introduced two additional features to their procedure:

1. In addition to the contour-length histogram, we assign to every trace a zero-point, that is the point of tip-sample contact. Given the correlation curve (*C*; equation 3) of two curves, we then multiply the correlation curve with a Gaussian curve centered at the point in which the zero-points of the two curves match with each other (equation 4; **Fig. S3 b**). The idea is to apply a "potential well" to reduce the maximum displacement of the two zeros.
2. Group division proposed by Bosshart and colleagues works only if all the curves with the same number of peaks have the peaks in the same position, but this is not generally true for F-d curves of the same protein. Therefore, we used a group division following the method described in **Fig S5**. In this way, we imposed two constrains for a given trace to be part of a given group: to have a specific number of peaks and to have these peaks in a specific position.

In Fodis, the correlation curve *C* is computed between each couple of Lc histograms with *xcorr* MATLAB function, that is:

$$C[lag] = \sum_{i=min_{lag}}^{max_{lag}} h_1[lag]\, h_2[lag + i] \tag{3}$$

where *lag* is the relative shift between the two curves, h_1 and h_2 are the Lc histograms of the two curves, and min_{lag} and max_{lag} are the minimum and maximum allowed shifts. In order to minimize the displacement of the curves from the origin, we weighted the cross-correlation *C* with a Gaussian distribution *G* centered in the point of zero relative shift (see **Fig. S3 b)**:

$$C_f[lag] = C[lag]\ \ G[lag] \tag{4}$$

The best relative shift was the *lag* corresponding to the maximum value of C_f. Finally, the weighted contour length reference used for final re-alignment was "binarized" to avoid depletion of rare but statistically relevant peaks (**Fig. S3 c**).

Note 4

Multi Gaussian Fitting of Global Histogram of Maxima (GHM)

GHM shows the distribution of unfolding events (peaks) along the Lc coordinate. In 2013 it has been shown by Kawamura and colleagues (12) that an ideal GHM can be fitted by a Gaussian mixture model to determine the probability of occurrence of a certain unfolding event (likely corresponding to a stable structural segment). The fitting implemented in Fodis uses *fitgmdis* MATLAB function over 100 iterations. To determine the correct number of Gaussian bells that best fit the distribution, we computed *N* different distribution of Gaussian mixtures *{g1, … , gN}* where *g1* has *1* Gaussian bell, and *gN* has *N* Gaussian bells. The best distribution *gX* is the one that minimize the Akaike Information Criterion (AIC) (13). A real GHM is characterized by a distribution that is the sum of Gaussian bells, plus a constant background noise (12). To overcome this problem, Fodis divides the Lc values relatively to the selected bin size, and within each bin it randomly removes one point of Lc distribution. In this way, by setting different bin sizes it is possible to tune the background noise and enhance peak detection and fitting.

Supporting References

1. Savitzky, A., and M.J.E. Golay. 1964. Smoothing and Differentiation of Data by Simplified Least Squares Procedures. Anal. Chem. 36: 1627–1639.

2. Marko, J.F., and E.D. Siggia. 1995. Statistical mechanics of supercoiled DNA. Phys. Rev. E. 52: 2912–2938.

3. Puchner, E.M., G. Franzen, M. Gautel, and H.E. Gaub. 2008. Comparing Proteins by Their Unfolding Pattern. Biophysical Journal. 95: 426–434.

4. Carrion-Vazquez, M., A.F. Oberhauser, T.E. Fisher, P.E. Marszalek, H. Li, and J.M. Fernandez. 2000. Mechanical design of proteins studied by single-molecule force spectroscopy and protein engineering. Progress in Biophysics and Molecular Biology. 74: 63–91.

5. Oesterhelt, F., D. Oesterhelt, M. Pfeiffer, A. Engel, H.E. Gaub, and D.J. Müller. 2000. Unfolding Pathways of Individual Bacteriorhodopsins. Science. 288: 143–146.

6. Celik, E., and V.T. Moy. 2012. Nonspecific interactions in AFM force spectroscopy measurements. J. Mol. Recognit. 25: 53–56.

7. Amestoy, P., T. Davis, and I. Duff. 1996. An Approximate Minimum Degree Ordering Algorithm. SIAM. J. Matrix Anal. & Appl. 17: 886–905.

8. Bosshart, P.D., P.L.T.M. Frederix, and A. Engel. 2012. Reference-Free Alignment and Sorting of Single-Molecule Force Spectroscopy Data. Biophysical Journal. 102: 2202–2211.

9. Schönfelder, J., R. Perez-Jimenez, and V. Muñoz. 2016. A simple two-state protein unfolds mechanically via multiple heterogeneous pathways at single-molecule resolution. Nature Communications. 7: ncomms11777.

10. Yu, H., M.G.W. Siewny, D.T. Edwards, A.W. Sanders, and T.T. Perkins. 2017. Hidden dynamics in the unfolding of individual bacteriorhodopsin proteins. Science. 355: 945–950.

11. Maity, S., M. Mazzolini, M. Arcangeletti, A. Valbuena, P. Fabris, M. Lazzarino, and V. Torre. 2015. Conformational rearrangements in the transmembrane domain of CNGA1 channels revealed by single-molecule force spectroscopy. Nature Communications. 6: 7093.

12. Kawamura, S., M. Gerstung, A.T. Colozo, J. Helenius, A. Maeda, N. Beerenwinkel, P.S.-H. Park, and D.J. Müller. 2013. Kinetic, Energetic, and Mechanical Differences between Dark-State Rhodopsin and Opsin. Structure. 21: 426–437.

13. Akaike, H. 1974. A new look at the statistical model identification. IEEE Transactions on Automatic Control. 19: 716–723.

BBA - Biomembranes 1860 (2018) 2532–2538

Contents lists available at ScienceDirect

BBA - Biomembranes

journal homepage: www.elsevier.com/locate/bbamem

Single-cell unroofing: probing topology and nanomechanics of native membranes

Nicola Galvanetto

International School for Advanced Studies (SISSA), via Bonomea 265, Trieste 34136, Italy

ARTICLE INFO

Keywords:
Native membrane
Nanomechanics
AFM
Unroofing
Neuron
Single-cell

ABSTRACT

Cell membranes separate the cell interior from the external environment. They are constituted by a variety of lipids; their composition determines the dynamics of membrane proteins and affects the ability of the cells to adapt. Even though the study of model membranes allows to understand the interactions among lipids and the overall mechanics, little is known about these properties in native membranes. To combine topology and nanomechanics analysis of native membranes, I designed a method to investigate the plasma membranes isolated from a variety of single cells. Five cell types were chosen and tested, revealing 20% variation in membrane thickness. I probed the resistance of the isolated membranes to indent, finding their line tension and spreading pressure. These results show that membranes isolated from neurons are stiffer and less diffusive than brain cancer cell membranes. This method gives direct quantitative insights on the mechanics of native cell membranes.

1. Introduction

When the first observation of the bi-layered nature of cell membrane was made using the electron microscope in 1959 [1], the notion that it was composed of lipid layers had already been accepted for decades [2,3]. Since then, much has been discovered in terms of membrane composition and function, mostly thanks to biochemical approaches.

The direct imaging of a native membrane remained challenging for years because of its fluid nature. Major advancements occurred only in the Seventies when various techniques showed their potential and gave birth to what is now broadly called 'cell unroofing'.

They involved the separation of cell cortices by violent mechanical treatments [4], combined with electron microscopy. To observe the membrane isolated from the cytosolic environment, the cells were firstly deposited on a surface coated with a "glue" (*e.g.* poly-L-lysine or Alcian blue), and then broken. The aim is to isolate the cell membrane adherent with the substrate from the rest of the cell. Three are the main strategies that can be applied. The first strategy is to expose the cells to a strong *lateral flux* of medium: this will break the cells leaving residues of membranes attached to the substrate [5]. The second is *fracturing*: it consists on sandwiching the cells, freeze and separate the sandwich [6,7]; this allowed to achieve a more natural, life-like appearance of the samples. A variant of the fracturing method is the recently developed iMEM [8] that consist of isolating the cell membranes during the blotting step of a Cryo-EM grid preparation. The third uses *sonic waves* to break the body of the cells: in this way only the layer of membrane in contact with the substrate remains [9]. The preparation usually ends with a physical fixation of the sample and the investigation with the electron microscope.

Looking directly to the cytosolic side of the membrane expanded our knowledge on the internal architecture of the cell membrane that before was simply not accessible [10,11].

Another natural instrument of investigation with sub-nanometer precision is the atomic force microscope (AFM). AFM has a big advantage compared to light or electron microscopy, in fact the sample doesn't require neither fluorescent labels nor metal coating or cryo-fixation. Some recent studies [12–16] unraveled a detailed architecture of the cytoskeleton on the inner face of fixed membranes with a resolution of ~5 nm.

However, the preparation of these samples requires a considerable know-how to be successful and to become reproducible in large scale [13]; moreover the aforementioned treatments act on the entire cultures without any fine control of the process. In fact, the studies that required the manipulation of lipid membranes and vesicles concentrated mostly on synthetic preparations of mixtures of lipids [17–19]. Model membranes are in particular suitable for the study of lipids interactions [20–23] and to test how the membranes behave in their physiological environment. These studies demonstrated that the strength of the bilayer is enhanced by lowering the temperature

E-mail address: nicola.galvanetto@sissa.it.

https://doi.org/10.1016/j.bbamem.2018.09.019
Received 22 June 2018; Received in revised form 19 September 2018; Accepted 26 September 2018
Available online 28 September 2018
0005-2736/

[24,25], or when exposed to high ion concentrations [26] or in a mixture with cholesterol that mimic lipid rafts [27,28].

Here I present a method that allows the direct study of native membranes in buffer solution and under ambient pressure and temperature. I present an AFM topography analysis that depicts heights differences in the membrane of different cell types. I measured their breaking forces which allowed to determine the line tension and the spreading pressure, through the indentation of the bilayers with the tip of the AFM. Furthermore, I discuss future improvements to obtain submolecular resolution of membrane proteins in their native environment and the requirements for *in vivo* applications.

2. Materials and methods

2.1. Overview of the setup for sample preparation

The setup was based on an AFM (JPK Nanowizard III) mounted on an inverted optical microscope (Olympus IX71) as sketched in Fig. 1A and Fig. S1. The three central elements of Fig. 1A consist of a cell culture coverslip, mounted on a holder, and squeezed with a triangular glass (see the next Sections for the details). During the sample preparation process, the AFM was used just as a motor with micrometer precision, indeed it was obtained the same results squeezing the cells with a water three-axis micromanipulator.

2.2. Cell cultures

The method was tested with 5 cell types: U87, U251, HEK293, primary hippocampal neurons, primary dorsal root ganglia (DRG) neurons.

The preparation of the glass coverslip was identical for all the five cell types: glass round coverslips (12 mm in diameter, 200 μm in thickness) were plasma cleaned for 15 s, coated with 0.5 mg/ml poly-D-lysine (Sigma-Aldrich, St. Louis, MO, USA) for 1 h at 37 °C and washed 3 times in deionized water. The coating is necessary to create a strong adhesion between the cells and the substrate because they must resist the compression and the laceration.

Hippocampal and DRG neurons from Wistar rats (P2-P3) were prepared in accordance with the guidelines of the Italian Animal Welfare Act, and their use was approved by the Local Veterinary Service, the SISSA Ethics Committee board and the National Ministry of Health (Permit Number: 2848-III/15) in accordance with the European Union guidelines for animal care (d.l. 26, March 4th 2014 related to 2010/63/UE and d.1. 116/92; 86/609/C.E.). The animals were anesthetized with CO_2 and sacrificed by decapitation, and all efforts were made to minimize suffering. Dissociated cells were plated at a concentration of 4×10^4 cells/ml. The medium used for hippocampal neurons is in Minimum Essential Medium (MEM) with GlutaMAX supplemented with 10% Fetal Bovine Serum (FBS, all from Invitrogen, Life Technologies, Gaithersburg, MD, USA), 0.6% D-glucose, 15 mM Hepes, 0.1 mg/ml apo-transferrin, 30 μg/ml insulin, 0.1 μg/ml D-biotin, 1 μM vitamin B12 (all from Sigma-Aldrich), and 2.5 μg/ml gentamycin (Invitrogen). The medium used for DRG neurons is Neurobasal medium (Gibco, Invitrogen, Milan, Italy) supplemented with 10% Fetal Bovine Serum (FBS, from Invitrogen, Life Technologies, Gaithersburg, MD, USA). The experiments were performed from two to five days after dissociation.

The human HEK293, U87 and U251 cell lines were cultured with Dulbecco's modified Eagle's media (DMEM, Gibco) supplemented with antibiotics (100 U/ml penicillin, 100 μg/ml streptomycin, Gibco), GlutaMax Supplement (2 mM, Gibco), and 10% fetal bovine serum (Biowest, USA). All the cells were grown under standard culture conditions (37 °C and 5% CO_2).

2.3. Cell culture holder

The scope of the cell culture holder is to connect the cell culture (*i.e.* a coverslip) to a device that moves it with micrometer precision. The holder was designed for an AFM JPK Nanowizard III mounted on an Olympus IX71 optical microscope (but previous trials were successfully performed with a water three-axis manipulator). In Fig. S1 is shown the comparison between the original cantilever holder and the cell culture holder: the two share the same bayonet couplings. The cell culture holder is a cylinder that allows to glue the coverslip with Vaseline in the base of the cylinder. The cell culture holder was drawn in Solidworks and printed in resin (visijet m3 black) with a Projet 3510 HD 3D system (see Fig. S1 for more details; for the Solidworks file please contact the corresponding author). With the adaptation of the bayonet couplings, an equivalent coverslip holder can be used on every AFM-Inverted microscope setup.

2.4. Triangular coverslips preparation (glass arrows)

Glass coverslips (24 mm in diameter, 200 μm in thickness) were plasma cleaned for 15 s and broken in 4 quarter with the use of the hands. This passage is crucial and better explained in Fig. S2. It is worth noting that the coverslips cannot be cut with a diamond tip because the fracture must be sharp. The resulting quarters (called glass arrows) was immersed in 0.5 mg/ml poly-D-lysine (Sigma-Aldrich, St. Louis, MO, USA) for 30 min. The glass arrows were immersed in deionized water for 10 s before use.

2.5. Cell squeezing

The cell squeezing was performed bringing in contact two parts: the arrow and the cell culture (Fig. 1B–G).

Lower part: tilted arrow. The cover of a petri dish was filled with Ringer solution (2 ml). The arrow was placed tilted of 7–15 degrees (see Fig. S1) in the middle of the cover. The cover of the petri dish was then fixed on the stage of the AFM.

Top part: the cell culture was glued with Vaseline to the holder, and they were mounted on the AFM head stage (Fig. S1). The Head Stage was put on top of the AFM in measurement position. Gradually, the cell culture was immersed into the solution, by lowering the head stage with the electrical motors of the AFM. The distance between the cell culture and the arrows was controlled with the help of the optical microscope. Once the distance reached ~50 μm, I chose the target cell, centering the apex of the arrow. I set the focus of the microscope in the position of the arrow and I brought the cell in contact with the arrow 2 μm at a time. When the cell touches the arrow, it enlarges. I continued to approach until the cell doubled its area. I kept it in contact for 3 min and then I rapidly lifted the coverslip. Nothing, or just few cellular debris can be visible in the contact region, otherwise the preparation will result contaminated. The arrow was then laid down and fixed (see Fig. S1 D and E). The medium was replaced slowly, without drying completely the solution (the isolated membrane should not come out of the solution).

2.6. AFM imaging and force spectroscopy

AFM imaging and force spectroscopy were performed with a Nanowizard III system (JPK) mounted on an inverted optical microscope (Olympus IX71), using Hydra NGG (Appnano) cantilevers with nominal spring constant of 0.084 N/m. AFM images were taken in intermittent contact mode applying the lowest possible force during imaging (cantilever free oscillation amplitude was set at 18–20 nm, the surface was approached and scanned at ~75% of the free amplitude). Force-distance curves were acquired at a rate of 2000 nm/s. AFM imaging and force spectroscopy were performed in Ringer's solution (NaCl 145 mM, KCl 3 mM, CaCl2 1.5 mM, MgCl2 1 mM, Glucose

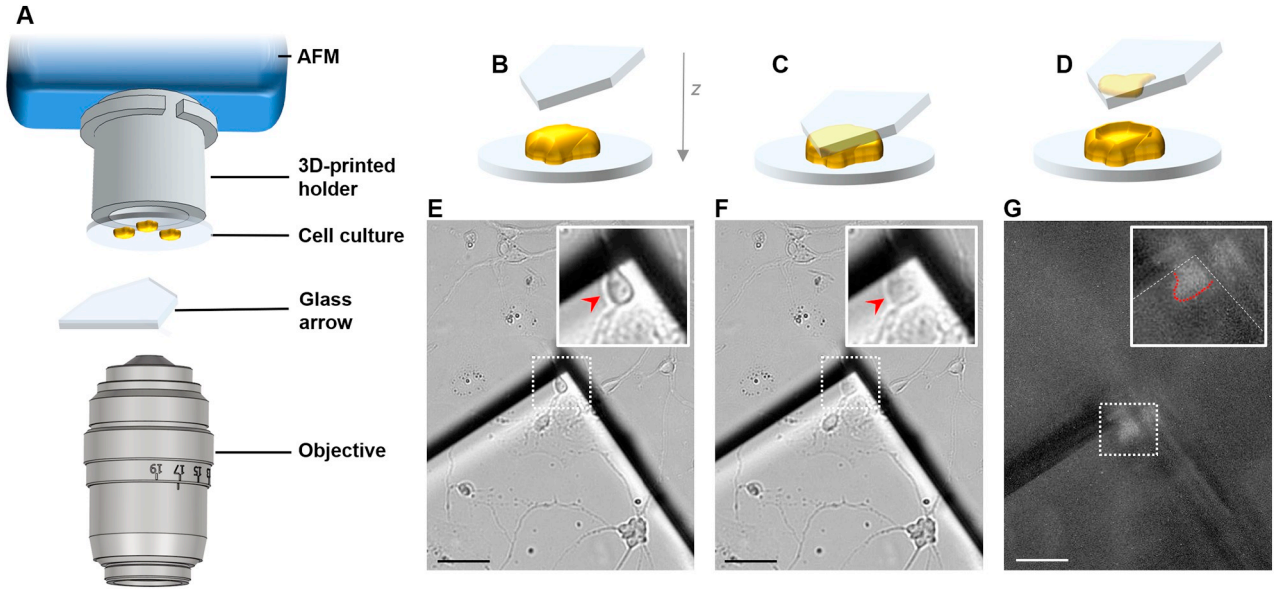

Fig. 1. (A) Scheme of the apparatus: the cell culture holder is mounted on the head-stage of the AFM which moves the cell culture downward against the fixed glass arrow. The process is controlled using the optical microscope. (B-C-D) Exemplificatory draws of the compression of one cell (the scheme is upside-down, and the cell is enlarged for clarity). (E-F-G) images of the compression of the target cell. (B-E) before compression, (C–F) during compression the cell is squeezed, (D-G) after compression. (G) The cell was stained with a fluorescent membrane dye (DII) to identify the membrane with the fluorescent image.

10 mM, HEPES 10 mM adjusted to pH 7.4 with NaOH) at 24C. The AFM height sensor was calibrated with the TGZ01 calibration grid before and after the series of experiments.

2.7. Data analysis

The AFM images were processed with the open source software Gwyddion [29]. The height measure (for each topographical image) was calculated as described in Fig. S3: briefly, the resulting height of the membrane is here defined as the difference between the mean of the z-position of the substrate and the mean of the z-position of the membrane (~10,000 z-positions for each level). Then, the mean of three height measures for each cell type is computed and reported in Fig. 2F (n = ~10,000/3 z-positions/samples). The error bars represent the standard error of the mean. The roughness was defined as the root mean square (RMS) of the height distribution, and calculated in Gwyddion. The force-distance curves and the force maps were analyzed with a modified version of the open source software Fodis [30] that automatically detects the baseline and the Breakthrough force. Breakthrough force averages of 800–1000 force spectra were calculated for each cell type and reported in Fig. 3B. The error bars represent the standard deviation of the distributions. The nucleation model was applied to the breaking force distributions and fitted with an add-on module of Fodis following the procedure described by Chiantina et al. [31]. The modified version of Fodis is available at https://github.com/nicolagalvanetto/Fodis.

3. Results

3.1. Upper membrane separation

I developed a method that allows the combination of topographical and mechanical investigations of native cell membranes. For this, I needed to make a preparation of exposed native membranes, separated from the entire cell, and arranged on a neutral support.

The method was designed to fit two additional requirements: i) the operation had to be simple and reproducible; ii) the membrane had to be localized easily (it is not visible by bright-field microscopy).

For this purpose, I designed a cell culture holder (see Fig. 1A and Fig. S1) to connect the cells to a motor with micrometer precision, and a new protocol to prepare optically-sharp arrows from common glass coverslips (Fig. S2). The target cell is brought in contact with the apex of the arrow and squeezed for ~3 min. Then, the cell culture is rapidly moved away. The membrane that went in contact with the arrow is torn from the cell as a consequence of the interaction between the membrane itself and the polylysine coating of the arrow.

Remarkably, the membrane remains on top of the flat corner of the arrow, like the footprint of the squeezed cell. The extracted membrane is therefore poised for various investigations, in fact it is exposed to the buffer which can include specific ligands that can activate membrane proteins involved in signal transduction, or in metabolic and bioenergetics processes.

I tested 5 cell types of various shapes and dimensions: one human epithelial cell line (HEK293), two human brain cancer cell lines (U87, U251) and two types of primary neurons (Hippocampal and dorsal root ganglia neurons (DRG) from rats). The proposed method was successful for all but the HEK293. The method fails with cell types that do not adhere well to the cell culture coverslip, so that they remain attached to the arrow after compression, without breaking. Improving the adhesion of the cells to the cell culture will expand the usable cell types for this method. The success rate, *i.e.* the production of samples suitable for AFM investigations, was ~80%.

3.2. Topographical characterization of native membranes at room temperature

A natural instrument of investigation that operate in almost-physiological conditions is the AFM, but a non-trivial task is the localization of the region of interest when it is optically invisible. In the method presented here the localization is straightforward: in fact, the membrane is in the very same corner of the arrow (Fig. 2A and B).

I performed AFM imaging of the intracellular side of the membrane of U87, U251, Hippocampal and DRG cells using cantilevers with spring constant of 0.08 N/m in intermittent contact mode. The isolation method worked unexpectedly well with Hippocampal neurons, the AFM image (Fig. 2C) revealed that the upper membrane is completely separated from the cell, and it covers the area where the cell got in contact with the arrow. The membrane surface is highly flat and it

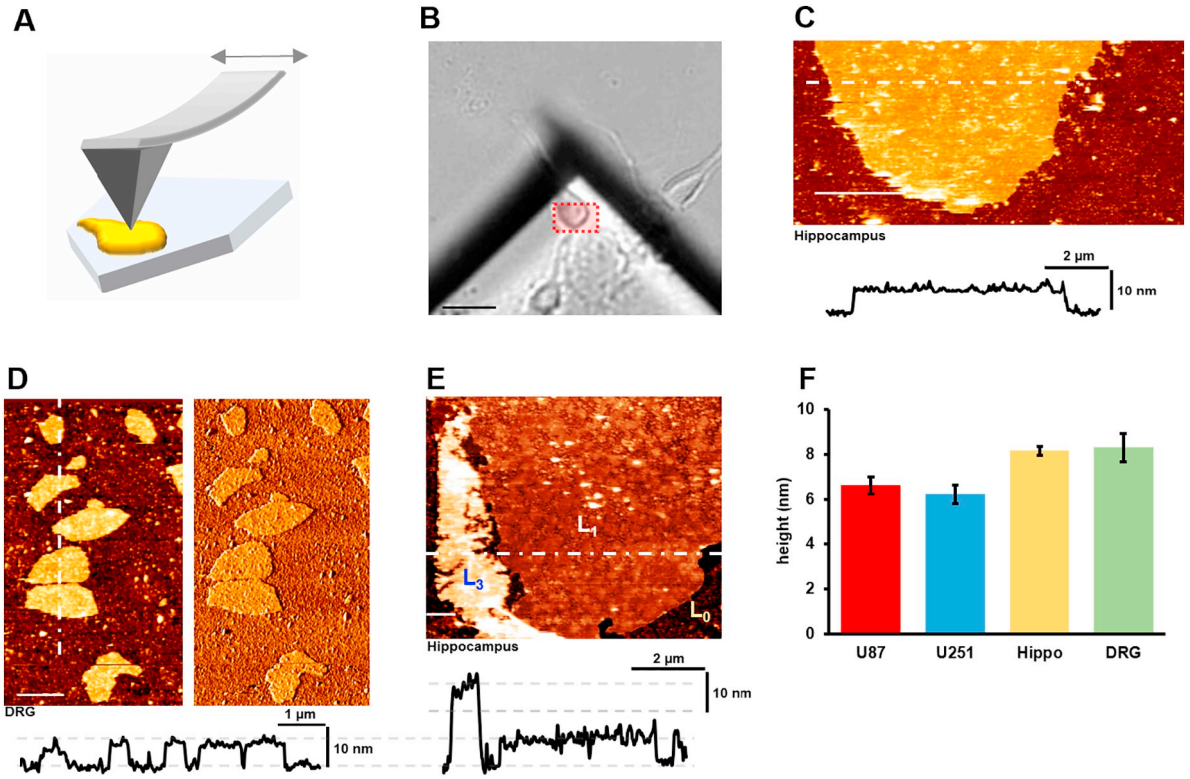

Fig. 2. (A) Scheme of the imaging process. (B) Hippocampal neuron during compression, the red area represents the area imaged in (C) on the glass arrow, after the removal of the cell culture (scalebar 15 µm). (C) AFM topography image of the upper membrane of a hippocampal neuron (scalebar 4 µm) and the z-profile under the dotted line. (D) AFM topography and phase image of a DRG membrane (scalebar 1 µm). (E) AFM image of a hippocampal membrane showing three different levels: L_0 glass, L_1 single bilayer, L_3 triple bilayer (folded). (F) the histogram reports the average membrane height and the standard error of the mean of n = 10,000/3 z-positions/samples for each cell type (see Section 2.7 for the detailed procedure).

displayed no cytoskeletal feature within the investigated dimensions (10 nm-10 µm range) unlike previously reported with other methods or cell types [10,14]. A higher resolution image indicate the presence of 30 nm-size complexes, most likely of proteic nature [16] (Fig. S4). DRG's membrane surfaces are qualitatively similar to Hippocampal ones, with the exception that the isolated membranes form island of ~2 µm^2 (Fig. 2D) instead of a continuous and complete layer of ~50 µm^2. U87 and U251 membranes showed an intermediate behavior: continuous regions interspersed with more fragmented islands (Fig. S4). The reasons of these different behaviors may be ascribed to a different membrane composition, or a different anchoring to the cytoskeleton that prevents a complete separation. Even with the same cell type there was some variability in the way the cell membrane is torn. For instance, the membrane near the border that did not adhere well to the polylysine, showed to favor a multi-bilayer conformation (Fig. 2E) rather than floating freely in the solution. The dynamics of the membrane transfer is complicated, but it is clearly the behavior of a fluid layer that adapts to the shape of the support, differently from a crystalline membrane of comparable thickness [32].

I perform also extensive characterization of the polylysine coated glass, which resulted to be affected by the violent separation of the membrane. In particular I tested the glass roughness (see Section 2.7) in three conditions: i) before the isolation, ii) after the isolation far from the membrane, iii) after the isolation in proximity of the membrane. Condition (i) and (ii) didn't show particular differences, while condition (iii) showed a 2-fold increase in the measured roughness. As suggested by Heuser [9], polylysine attracts the freely floating proteins in the solution. The hypothesis is that after the breakage of the cell, the cytosolic proteins diffuse around the site of the breakage, adhering to the coated glass and forming a layer on top of the polylysine. This hypothesis is supported by the Fig. S4 which shows a portion of flat glass close to a region of more rough glass. The flat small region can be interpreted as an area that was shielded during the breakage. Therefore, the blob-like features on top of the membrane are presumably authentic and due to protein complexes, but they cannot be further resolved with the reported experimental conditions.

I measured the membrane height of the four cell types according to the procedure explained in Section 2.7. The height distribution of the membrane in a single sample is typically Gaussian (Fig. S3). The height measures are then averaged over 3 samples: mean and standard error of the mean is reported in Fig. 2F. The height of hippocampal and DRG membranes are of 8.2 nm and 8.3 nm respectively, they are ~2 nm thicker than the U87 (6.2 nm) and U251 (6.6 nm). The measured membrane heights are between 50% and 100% thicker than the well characterized model membranes dipalmitoylphosphatidylcholine (DPPC) or dioleoylphosphatidylcholine (DOPC) [24] that are 4–5 nm thick, and more similar to purple membrane [33].

3.3. Nanomechanical properties of the membranes

After a precise determination of the position of the membrane, I could perform the puncturing of the bilayer, recording the resulting force-distance curves. The shape of the approach curves showed an initial elastic deformation (Fig. 3A blue arrow) followed by an abrupt jump (5–8 nm; Fig. 3A red arrow). The reversible compression of the bilayer only partially accounts for the reported elastic deformation, other contributions are probably due to some soft layer deposited on the tip and collected during scanning. The jump, on the other hand, clearly represents the membrane rupture that displays a step comparable with the height of the membrane.

I observed the presence of an additional rupture event in a non-negligible percentage of force curves (sometimes up to 20%, Fig. S5),

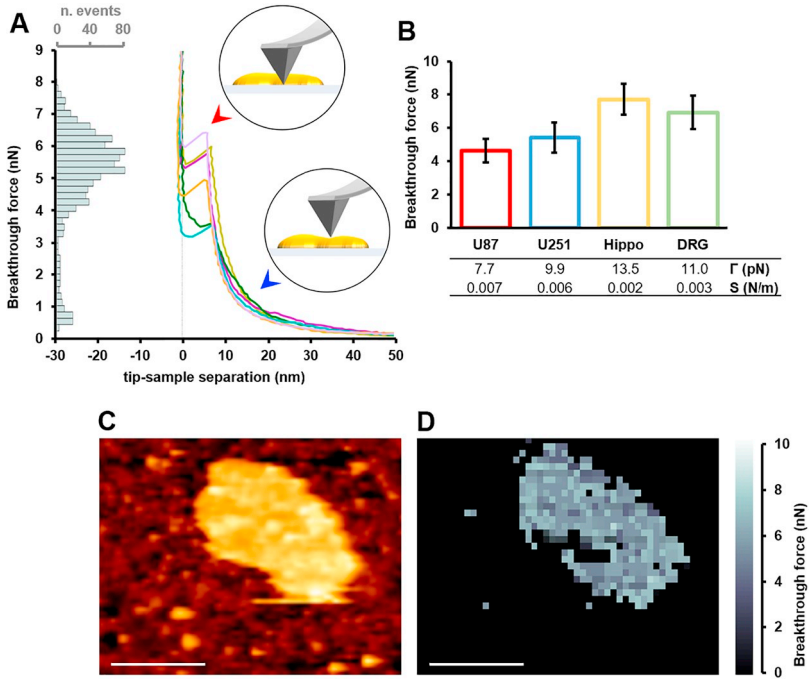

Fig. 3. (A) Force-distance indentation curves of U251 and the distribution of the rupture events. (B) average rupture forces and standard deviation of the distribution. The table presents the line tension Γ and the spreading pressure S calculated with the nucleation model (see Section 2.7). (C) AFM topographical image of DRG membrane before the (D) force map of the rupture events in the same region (scalebar 1 μm, 0 pN is intended for regions where no Breakthrough force was detected).

which is due to an extra lipid bilayer formed on top of the cantilever tip [26]. The curves showing two rupture events were not considered in the quantitative analysis.

Fig. 3B shows the average Breakthrough force of 800–1000 spectra for the four cell types and the standard deviation of the force distribution. To minimize the variability induced by the tip changes, new cantilevers were used in each experimental session. Hippocampal membranes revealed to pierce at force values distributed around 7.7 nN, that is almost twice the force necessary to pierce the U87 membranes which break at 4.6 nN. DRG and U251 pierce at values in between, 6.9 nN and 5.4 nN respectively. The full-width half maximum (FWHM) of the four force distributions is, on the other hand, more similar among cell types showing 20% absolute variation at most.

This isolation method in combination with a new module for the software Fodis [30] (see Section 2.7), can generate also force-map images for a multiparametric characterization of the membranes (Fig. 3C and D). The analysis that I performed at 24 °C revealed a single Gaussian distribution of the piercing forces for all the cell types, suggesting the presence of a unique liquid phase [27].

The Breakthrough force is just a proxy of the thermodynamic quantities of the lipid bilayer. For a more detailed analysis of the biophysical parameters of these native membranes, I applied the nucleation model [21] that was originally developed for synthetic preparations [27,31]. Thanks to the method presented here, the nucleation model can now be applied to native membranes, for quantifying the real line tension Γ and spreading pressure S. The line tension Γ is measured in pN and it indicates the energy per unit of length (*i.e.* the unsaturated bonds of the periphery of the membrane), while the spreading pressure S is the combination of the interfacial energies per unit of area of the membrane. In a configuration like the one presented here, where the pieces of membranes are exposed to the solution from one side and to the polylysine from the other, Γ is the quantity that is minimized when the patches are circular (*i.e.* reducing the perimeter), while S is a measure of the tendency of spreading on the surface. The two neuron types have higher line tension compared to the two tumor cell lines but less than a half spreading pressure (values reported in Fig. 3B), indicating that a higher line tension is related to a lower tendency to diffuse. These measurements provides values in the range of previous experiments [27,34], and particularly close to model membranes of mixtures of lipids (DOPC/sphingomyelin/cholesterol), but not to pure DOPC or DPPC which have 2-to-3 fold lower line tension and spreading pressure. Furthermore, this comparison shows that the experiments that involve model membranes should be performed preferentially with mixtures of lipids when the precondition is to mimic the nanomechanics of real cell membranes.

4. Discussion

I developed a new approach for imaging the cytoplasmic side of the cell membrane and for quantifying its nanomechanical properties. In this approach, the upper cell membrane is separated from the entire cell, therefore it is poised for various investigations. I used the AFM to characterize the topology and to probe the mechanics of these native preparations.

The approach was in this way applied to an endothelial cell type, two brain tumor cell lines and two neuron types, and it has proved to be successful for all the cells that attach well to the culture coverslip. Specific culturing protocols are required for those cells that only loosely bind to the substrate.

Overall, these measurements are consistent with previous reports on synthetic membranes, but they provide additional information on the native state that are now easily accessible.

The average membrane thickness reveals to be constant within the same cell type, but it differs by some nanometers over the tested cell types. The presence of extracellular matrix residues that may affect the height measure cannot be excluded *a priori*, but their presence in the upper part of the cultured cells should be modest if not negligible. The height of the two tumor cell lines is similar to the well characterized purple membrane, and 25% thinner than the neuron cell membrane.

The topological features are only partially corrupted by the substrate roughness, but to reach the goal of imaging diffusive single proteins in their native membrane it is necessary to use High speed-AFMs in serial dedicated investigations [35–37].

The Breakthrough force is higher in the neural cell types compared to the tumor cells, which suggests a higher rigidity of the membrane. This is in agreement with the measurements on synthetic lipid mixtures [28] and the higher cholesterol content of the neurons [38].

The single peak of the Breakthrough force distributions suggests the

presence of a unique liquid phase in all the tested cells, as opposed to what has recently been shown in T-cells and HeLa cells where both the liquid ordered and liquid disordered phase was identified through fluorescence microscopy techniques [39]. It cannot be excluded that the AFM puncturing approach is not precise enough to resolve the coexistence of the two close phases (in terms of Breakthrough force) [28].

The nucleation model applied on native membranes allows to gather precise information on membrane packing, stability as well as intermolecular interactions among lipid molecules and proteins. The obtained values indicate that the neural membrane is more compact if compared to a more diffusive tumor membrane. In this regard, it is important to point out that the native membrane is deeply different from the model membranes that were tested in the past. Half of the weight of a native membrane is indeed due to membrane proteins [40]. The environment is highly diverse, therefore the biophysical parameters that was obtained here consider the overall contribution of lipids and proteins, leading to more robust values for computational lipidomics. To my knowledge, the sample preparation has always been problematic in previous unroofing techniques [13]. The single-cell method proposed here minimizes the sources of variability like large scale sonication or blotting, giving a success rate around 80%. The success rate becomes even more important when the unroofing needs to be operated *ex/in vivo*. To date, this method can directly be tuned for application on *ex vivo* thin tissues, but it is not immediately applicable *in vivo*. To overcome this problem, in the preparation process, the AFM should be substituted by a micromanipulator and the cells of interest should be accessible by the glass arrow. This kind of improvements could lead to an interesting tool for fast screening purposes of diseases that affect the cell membranes.

There could be interesting applications also in complementary fields like single-molecule force spectroscopy (SMFS) or bioactive surface studies. Müller and collaborators has indeed recently found that we can expect a different behavior in the unfolding of proteins in a native environment [41], therefore this single-cell unroofing could be an ideal platform for such unfolding investigations. While having the possibility to deposit a real membrane on top of the desired artificial nanostructure could help to study some microscopic phenomena at the nanoscale, for instance, the antimicrobial activity of nanodots [42].

In conclusion, the method described here can be used to study membrane topology and mechanics at the nanoscale level, the scale at which important processes such as mechanosensing and membrane fusion take place, providing clues on their biophysical constraints.

Transparency document

The Transparency document associated with this article can be found, in online version.

Acknowledgments

The author thanks Prof Vincent Torre for the support and the suggestions. The author thanks Manuela Lough for checking the English. The author thanks Simone Mortal, Andrea Pedroni and Sourav Maity for the useful discussions.

This research did not receive any specific grant from funding agencies in the public, commercial, or not-for-profit sectors.

Appendix A. Supplementary information

Supplementary information to this article can be found online at https://doi.org/10.1016/j.bbamem.2018.09.019. The software Fodis can be found at https://github.com/nicolagalvanetto/Fodis.

References

[1] J.D. Robertson, The ultrastructure of cell membranes and their derivatives, Biochem. Soc. Symp. 16 (1959) 3–43.
[2] H. Fricke, The electric capacity of suspensions with special reference to blood, J. Gen. Physiol. 9 (1925) 137–152, https://doi.org/10.1085/jgp.9.2.137.
[3] H. Davson, J.F. Danielli, The permeability of natural membranes, The Permeability of Natural Membranes, 1943 https://www.cabdirect.org/cabdirect/abstract/19452200240 , Accessed date: 6 February 2018.
[4] M.V. Nermut, The “cell monolayer technique” in membrane research, Eur. J. Cell Biol. 28 (1982) 160–172.
[5] M. Clarke, G. Schatten, D. Mazia, J.A. Spudich, Visualization of actin fibers associated with the cell membrane in amoebae of Dictyostelium discoideum, PNAS 72 (1975) 1758–1762.
[6] M.V. Nermut, L.D. Williams, Freeze-fracturing of monolayers (capillary layers) of cells, membranes and viruses: some technical considerations, J. Microsc. 110 (1977) 121–132, https://doi.org/10.1111/j.1365-2818.1977.tb00023.x.
[7] J.E. Heuser, T.S. Reese, M.J. Dennis, Y. Jan, L. Jan, L. Evans, Synaptic vesicle exocytosis captured by quick freezing and correlated with quantal transmitter release, J. Cell Biol. 81 (1979) 275–300, https://doi.org/10.1083/jcb.81.2.275.
[8] C.F. Peitsch, S. Beckmann, B. Zuber, iMEM: isolation of plasma membrane for cryoelectron microscopy, Structure 24 (2016) 2198–2206, https://doi.org/10.1016/j.str.2016.09.016.
[9] J. Heuser, The production of “cell cortices” for light and electron microscopy, Traffic 1 (2000) 545–552, https://doi.org/10.1034/j.1600-0854.2000.010704.x.
[10] N. Morone, T. Fujiwara, K. Murase, R.S. Kasai, H. Ike, S. Yuasa, J. Usukura, A. Kusumi, Three-dimensional reconstruction of the membrane skeleton at the plasma membrane interface by electron tomography, J. Cell Biol. 174 (2006) 851–862, https://doi.org/10.1083/jcb.200606007.
[11] K.A. Sochacki, G. Shtengel, S.B. van Engelenburg, H.F. Hess, J.W. Taraska, Correlative super-resolution fluorescence and metal-replica transmission electron microscopy, Nat. Methods 11 (2014), https://doi.org/10.1038/nmeth.2816 (nmeth.2816).
[12] J. Usukura, A. Yoshimura, S. Minakata, D. Youn, J. Ahn, S.-J. Cho, Use of the unroofing technique for atomic force microscopic imaging of the intra-cellular cytoskeleton under aqueous conditions, J. Electron Microsc. 61 (2012) 321–326, https://doi.org/10.1093/jmicro/dfs055.
[13] E. Usukura, A. Narita, A. Yagi, S. Ito, J. Usukura, An unroofing method to observe the cytoskeleton directly at molecular resolution using atomic force microscopy, Sci. Rep. 6 (2016), https://doi.org/10.1038/srep27472 (srep27472).
[14] F. Sato, H. Asakawa, T. Fukuma, S. Terada, Semi- in situ atomic force microscopy imaging of intracellular neurofilaments under physiological conditions through the “sandwich” method, Microsc. (Oxford) 65 (2016) 316–324, https://doi.org/10.1093/jmicro/dfw006.
[15] S. Janel, E. Werkmeister, A. Bongiovanni, F. Lafont, N. Barois, Chapter 9 - CLAFEM: Correlative light atomic force electron microscopy, in: T. Müller-Reichert, P. Verkade (Eds.), Methods in Cell Biology, Academic Press, 2017, pp. 165–185, , https://doi.org/10.1016/bs.mcb.2017.03.010.
[16] L. Picas, F. Rico, M. Deforet, S. Scheuring, Structural and mechanical heterogeneity of the erythrocyte membrane reveals hallmarks of membrane stability, ACS Nano 7 (2013) 1054–1063, https://doi.org/10.1021/nn303824j.
[17] E.M. Schmid, M.H. Bakalar, K. Choudhuri, J. Weichsel, H.S. Ann, P.L. Geissler, M.L. Dustin, D.A. Fletcher, Size-dependent protein segregation at membrane interfaces, Nat. Phys. 12 (2016) 704–711, https://doi.org/10.1038/nphys3678.
[18] T. Bhatia, J. Agudo-Canalejo, R. Dimova, R. Lipowsky, Membrane nanotubes increase the robustness of Giant vesicles, ACS Nano (2018), https://doi.org/10.1021/acsnano.8b00640.
[19] Z. Al-Rekabi, S. Contera, Multifrequency AFM reveals lipid membrane mechanical properties and the effect of cholesterol in modulating viscoelasticity, PNAS 115 (2018) 2658–2663, https://doi.org/10.1073/pnas.1719065115.
[20] Y.F. Dufrêne, T. Boland, J.W. Schneider, W.R. Barger, G.U. Lee, Characterization of the physical properties of model biomembranes at the nanometer scale with the atomic force microscope, Faraday Discuss. 111 (1999) 79–94, https://doi.org/10.1039/A807637E.
[21] S. Loi, G. Sun, V. Franz, H.-J. Butt, Rupture of molecular thin films observed in atomic force microscopy. II. Experiment, Phys. Rev. E 66 (2002) 031602, , https://doi.org/10.1103/PhysRevE.66.031602.
[22] R.P. Gonçalves, G. Agnus, P. Sens, C. Houssin, B. Bartenlian, S. Scheuring, Two-chamber AFM: probing membrane proteins separating two aqueous compartments, Nat. Methods 3 (2006), https://doi.org/10.1038/nmeth965 (nmeth965).
[23] S. Garcia-Manyes, F. Sanz, Nanomechanics of lipid bilayers by force spectroscopy with AFM: a perspective, Biochim. Biophys. Acta Biomembr. 1798 (2010) 741–749, https://doi.org/10.1016/j.bbamem.2009.12.019.
[24] Z.V. Leonenko, E. Finot, H. Ma, T.E.S. Dahms, D.T. Cramb, Investigation of temperature-induced phase transitions in DOPC and DPPC phospholipid bilayers using temperature-controlled scanning force microscopy, Biophys. J. 86 (2004) 3783–3793, https://doi.org/10.1529/biophysj.103.036681.
[25] U. Bhojoo, M. Chen, S. Zou, Temperature induced lipid membrane restructuring and changes in nanomechanics, Biochim. Biophys. Acta Biomembr. 1860 (2018) 700–709, https://doi.org/10.1016/j.bbamem.2017.12.008.
[26] S. Garcia-Manyes, G. Oncins, F. Sanz, Effect of ion-binding and chemical phospholipid structure on the nanomechanics of lipid bilayers studied by force spectroscopy, Biophys. J. 89 (2005) 1812–1826, https://doi.org/10.1529/biophysj.105.064030.
[27] S. Chiantia, J. Ries, N. Kahya, P. Schwille, Combined AFM and two-focus SFCS study of raft-exhibiting model membranes, ChemPhysChem 7 (2006) 2409–2418, https://doi.org/10.1002/cphc.200600464.
[28] R.M.A. Sullan, J.K. Li, C. Hao, G.C. Walker, S. Zou, Cholesterol-dependent nanomechanical stability of phase-segregated multicomponent lipid bilayers, Biophys. J.

99 (2010) 507–516, https://doi.org/10.1016/j.bpj.2010.04.044.
[29] D. Nečas, P. Klapetek, Gwyddion: an open-source software for SPM data analysis, Open Physics. 10 (2012) 181–188, https://doi.org/10.2478/s11534-011-0096-2.
[30] N. Galvanetto, A. Perissinotto, A. Pedroni, V. Torre, Fodis: software for protein unfolding analysis, Biophys. J. 114 (2018) 1264–1266, https://doi.org/10.1016/j.bpj.2018.02.004.
[31] A.J. García-Sáez, S. Chiantia, P. Schwille, Effect of line tension on the lateral organization of lipid membranes, J. Biol. Chem. 282 (2007) 33537–33544, https://doi.org/10.1074/jbc.M706162200.
[32] K. Schouteden, N. Galvanetto, C.D. Wang, Z. Li, C. Van Haesendonck, Scanning probe microscopy study of chemical vapor deposition grown graphene transferred to Au(111), Carbon 95 (2015) 318–322, https://doi.org/10.1016/j.carbon.2015.08.033.
[33] M. Stark, C. Möller, D.J. Müller, R. Guckenberger, From images to interactions: high-resolution phase imaging in tapping-mode atomic force microscopy, Biophys. J. 80 (2001) 3009–3018, https://doi.org/10.1016/S0006-3495(01)76266-2.
[34] J.D. Moroz, P. Nelson, Dynamically stabilized pores in bilayer membranes, Biophys. J. 72 (1997) 2211–2216, https://doi.org/10.1016/S0006-3495(97)78864-7.
[35] I. Casuso, J. Khao, M. Chami, P. Paul-Gilloteaux, M. Husain, J.-P. Duneau, H. Stahlberg, J.N. Sturgis, S. Scheuring, Characterization of the motion of membrane proteins using high-speed atomic force microscopy, Nat. Nanotechnol. 7 (2012) 525–529, https://doi.org/10.1038/nnano.2012.109.
[36] J. Preiner, A. Horner, A. Karner, N. Ollinger, C. Siligan, P. Pohl, P. Hinterdorfer, High-Speed AFM Images of Thermal Motion Provide Stiffness Map of Interfacial Membrane Protein Moieties, (2014), https://doi.org/10.1021/nl504478f.
[37] Y. Ruan, K. Kao, S. Lefebvre, A. Marchesi, P.-J. Corringer, R.K. Hite, S. Scheuring, Structural titration of receptor ion channel GLIC gating by HS-AFM, Proc. Natl. Acad. Sci. (2018) 201805621, , https://doi.org/10.1073/pnas.1805621115.
[38] H.I. Ingólfsson, T.S. Carpenter, H. Bhatia, P.-T. Bremer, S.J. Marrink, F.C. Lightstone, Computational lipidomics of the neuronal plasma membrane, Biophys. J. 113 (2017) 2271–2280, https://doi.org/10.1016/j.bpj.2017.10.017.
[39] D.M. Owen, D.J. Williamson, A. Magenau, K. Gaus, Sub-resolution lipid domains exist in the plasma membrane and regulate protein diffusion and distribution, Nat. Commun. 3 (2012), https://doi.org/10.1038/ncomms2273.
[40] G.M. Cooper, The Cell: A Molecular Approach, 2nd ed., (2000).
[41] J. Thoma, S. Manioglu, D. Kalbermatter, P.D. Bosshart, D. Fotiadis, D.J. Müller, Protein-enriched outer membrane vesicles as a native platform for outer membrane protein studies, Commun. Biol. 1 (2018) 23, , https://doi.org/10.1038/s42003-018-0027-5.
[42] G. Benetti, E. Cavaliere, A. Canteri, G. Landini, G.M. Rossolini, L. Pallecchi, M. Chiodi, M.J. Van Bael, N. Winckelmans, S. Bals, L. Gavioli, Direct synthesis of antimicrobial coatings based on tailored bi-elemental nanoparticles, APL Mater. 5 (2017) 036105, , https://doi.org/10.1063/1.4978772.

BBA – Biomembranes

Supplementary Figures

Single-cell unroofing: probing topology and nanomechanics of native membranes

Nicola Galvanetto

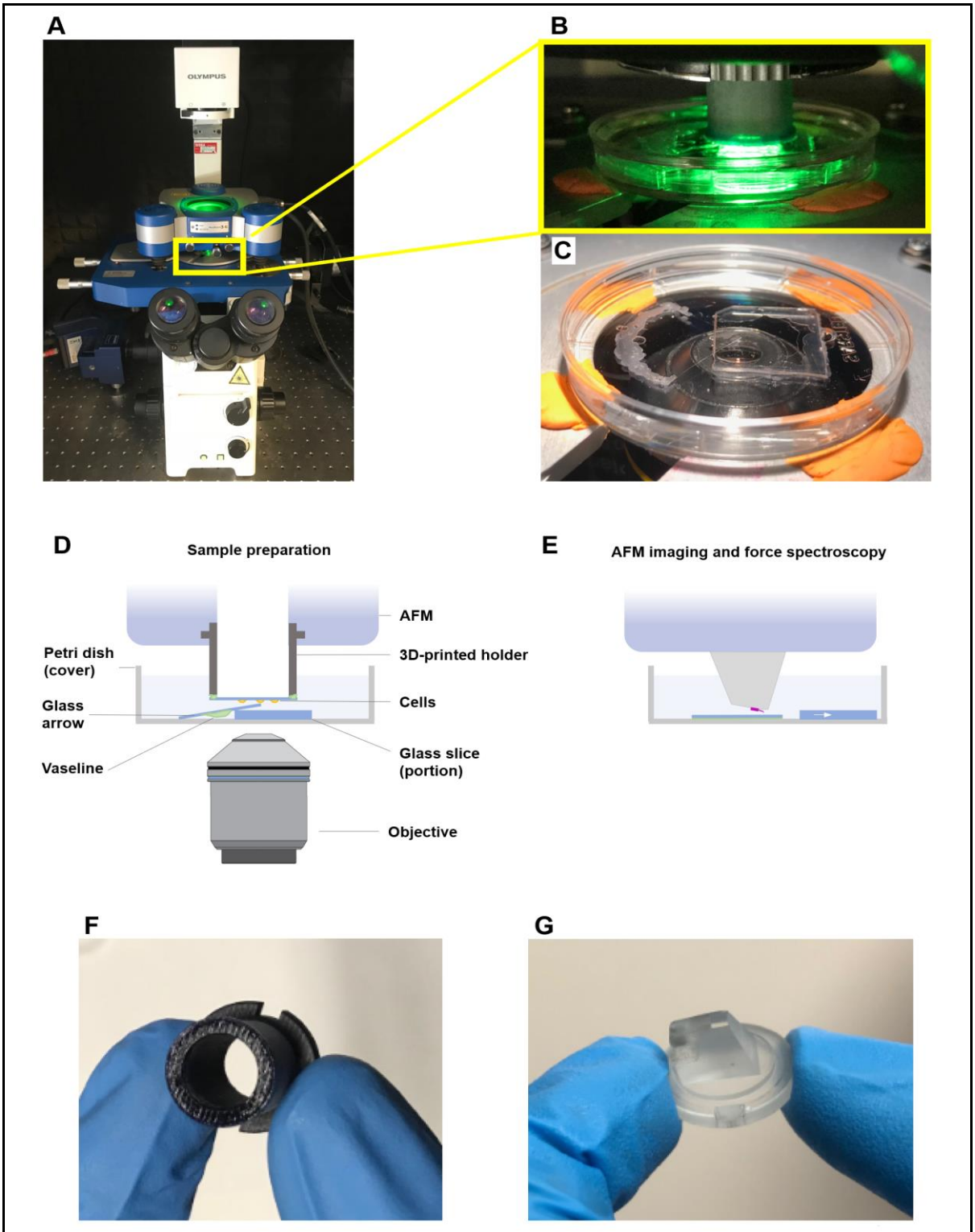

Supplementary Figure 1

Details of the Setup

(A) photo of the setup used: the Olympus microscope and the JPK AFM. (B) magnification of the components drawn in (D). (C) configuration of the tilted glass arrow and glass slice in (D). (D) scheme of the experiment during compression of the cells. (E) scheme of the configuration during AFM imaging or Force Spectroscopy. (F) 3D printed cell culture holder in comparison with (G) the cantilever holder.

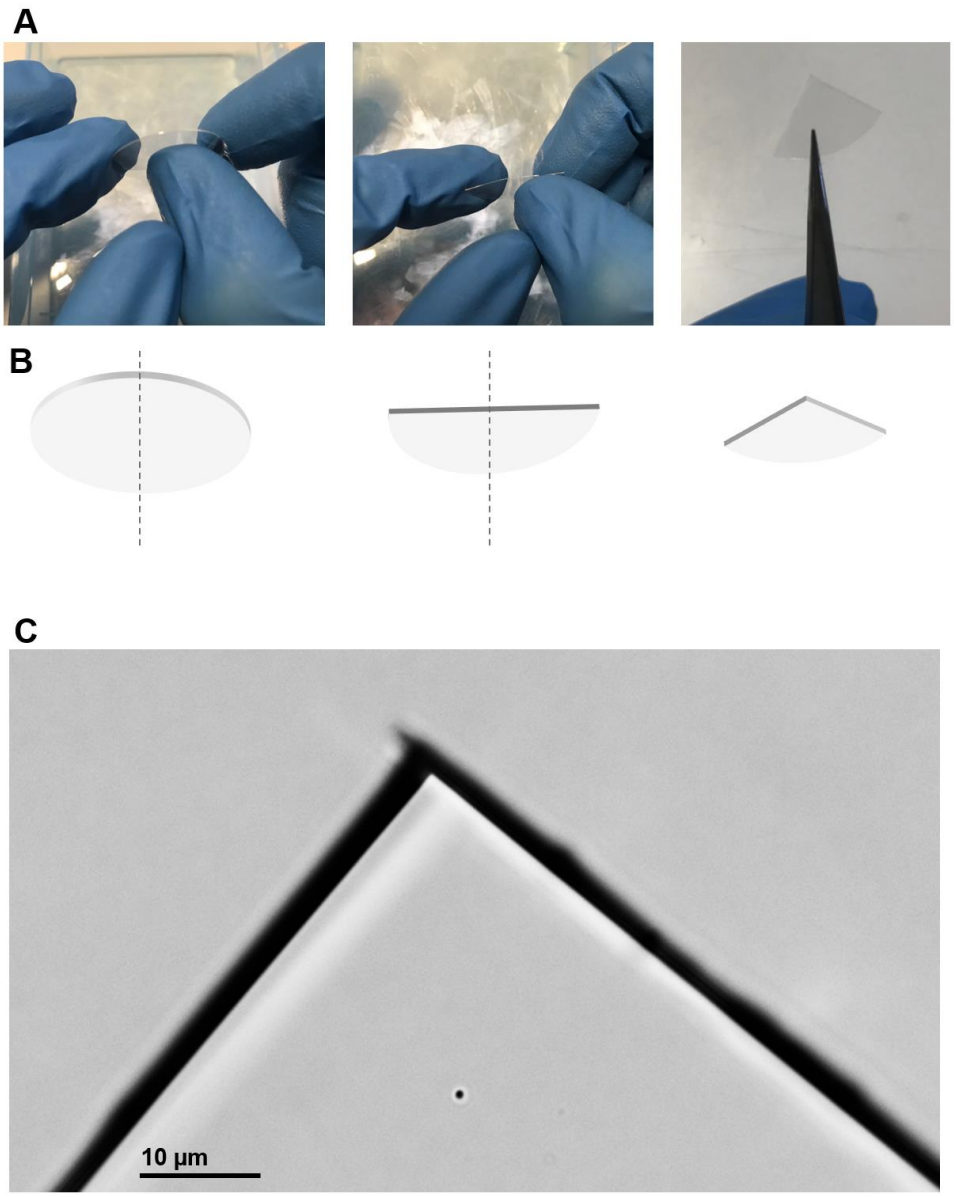

Supplementary Figure 2

Glass Arrows Preparation

(A) the 3 steps for the preparation of the glass arrow from a 24 mm coverslip (see Materials and Methods). Step 1 ((A) left): the round coverslip is broken in 2 pieces pushing with the thumb in the middle of the coverslip. Step 2 ((A) center): the half-coverslip is broken in other 2 pieces pushing with the thumb in the middle of the half-coverslip. Step 3 ((A) right): the sharpness of the apex is checked with the microscope (C). (B) scheme of the coverslip stages during the preparation in (A). (C) the apex of the glass arrow results to be optically sharp, as opposed to a cut with the typical diamond pen that shows 5 µm-size scratches along the edge.

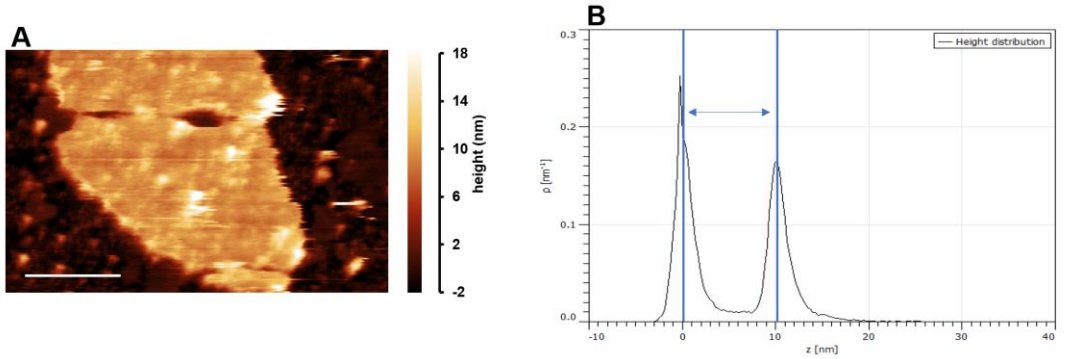

Supplementary Figure 3

Height Measurements

(A) AFM image (scalebar 1 µm) and corresponding (B) height distribution in Gwyddion. The reported height in Figure 2F is the difference between the means of the two bells.

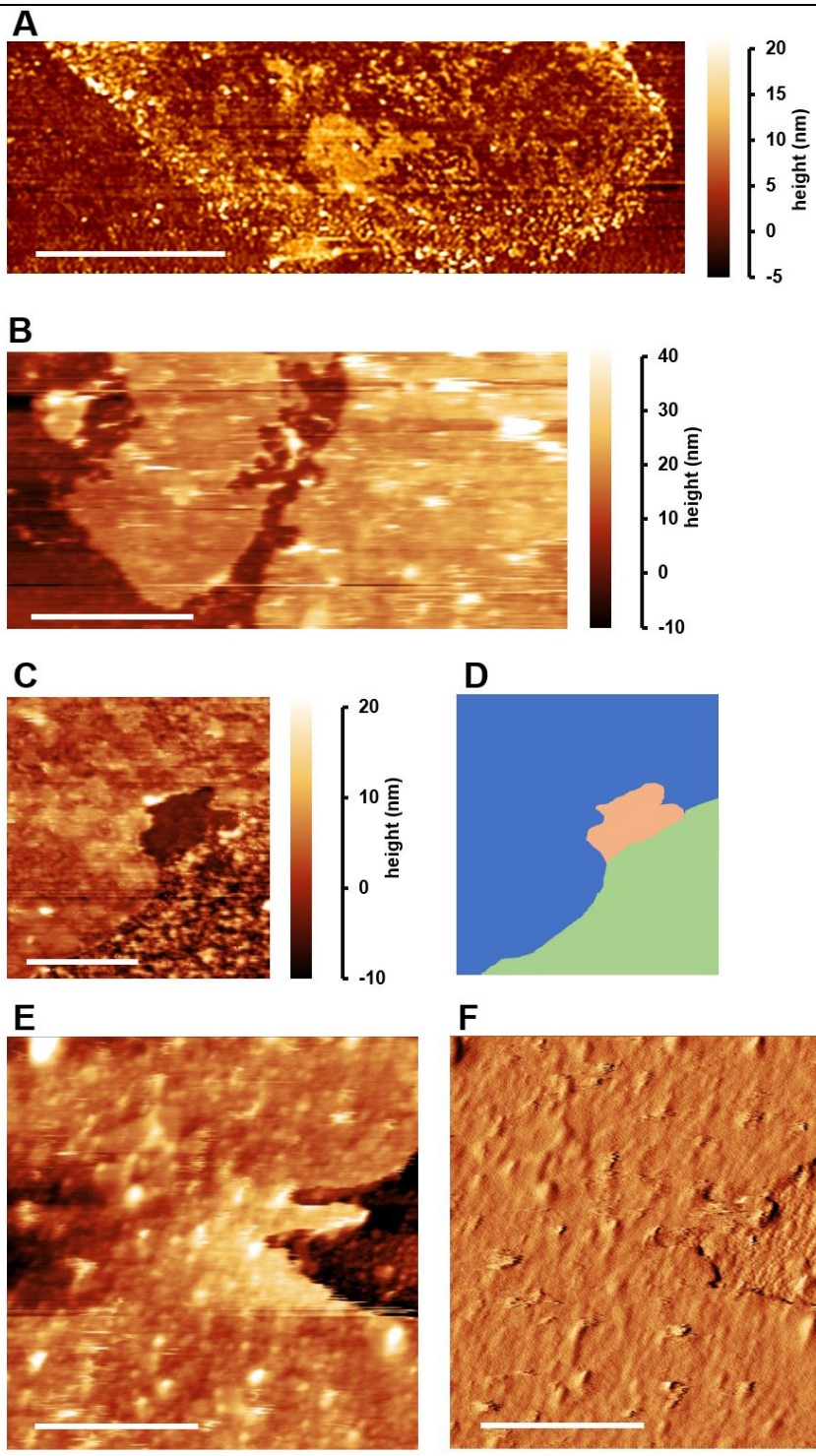

Supplementary Figure 4

AFM Imaging

(A) AFM image of a U251 cell membrane (scale bar 4 µm). (B) AFM image of a U87 cell membrane (scale bar 4.5 µm). (B) AFM image of a Hippocampal cell membrane (scale bar 2 µm) displaying three different surface features (D): (blue) surface of the membrane, (green) rough glass and (orange) smooth glass. I interpret the roughness in the green portion as the deposition of the cytosolic proteins of the broken cell, the orange portion was instead shielded during the unroofing process. (E) High resolution AFM image and (F) error signal of a Hippocampal membrane border (scale bar 500 nm).

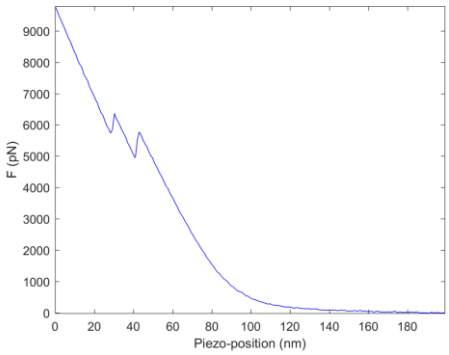

Supplementary Figure 5

Two-step Spectrum

Force-distance curve showing a two-step curve that indicate the presence of an extra bilayer of lipids.

Automatic classification of single-molecule force spectroscopy traces from samples containing heterogeneous mixtures of proteins

Nina I. Ilieva[1], Nicola Galvanetto[1], Michele Allegra[1,3], Vincent Torre[1] and Alessandro Laio[1,2]

[1] *Scuola Internazionale Superiore di Studi Avanzati (SISSA), via Bonomea 265 - 34136 Trieste, Italy*
[2] *The Abdus Salam International Centre for Theoretical Physics (ICTP), Strada Costiera 11,IT-34151 Trieste, Italy*
[3] *Institut de Neurosciences de la Timone UMR 7289, Aix Marseille Université, CNRS, 13005 Marseille, France*

Abstract

New experimental techniques allow harvesting millions of single molecule force spectroscopy (SMFS) traces from patches of a native cell membrane, potentially providing substantial information about its protein composition. However, extracting such information is a non-trivial data analysis challenge: only a small fraction of the recorded traces corresponds to the unfolding of a protein, the number of different protein types may be of the order of hundreds, and limited prior knowledge (if any) about the identity of the proteins is available. Here, we introduce a data analysis pipeline which filters out irrelevant traces (typically, 99% of the total), and finds among the remaining ones clusters of similar traces, plausibly associated with the unfolding of specific membrane proteins. We illustrate the performance of our method on a dataset of $\sim$ 400,000 traces extracted from a patch of rod membrane. Despite a daunting signal-to-noise ratio in the data, we are able to identify $\sim$ 20 clusters of traces, two of which likely correspond to Rhodopsin and the CNG channel - two proteins that are known to be present in the rod membrane.

1 Introduction

Atomic force microscopy (AFM)-based single molecule force spectroscopy (SMFS) is a powerful tool for studying proteins at the single molecule level. In a typical AFM-SMFS experiment, the protein is bonded on one side to a surface, and attaches on the other side to the AFM tip [1]. As the tip retracts from the surface, the protein gets stretched and unfolded. The resulting force and extension values are stored in the form of a force-extension (F-x) curve. In a single experimental session, thousands of F-x curves are generated, therefore a dataset can easily contain more than 10^5 curves. F-x curves, also called traces, are direct representations of the protein unfolding pathway and can be used to fingerprint specific proteins [2, 3, 4]. Labor intensive sample preparations allowed to perform AFM-SMFS on non-purified proteins directly in their native cell membranes [5, 6]. These methods normally aim at studying one single specific protein at a time. More recently, new methods seem to offer the possibility to analyze the native membrane environment as a whole on a wide range of cell types [7]. In these experiments, the majority of traces do not represent meaningful unfolding events, and if they do, they likely represent the unfolding of different proteins, since a native membrane hosts hundreds of different proteins. Available data analysis tools [8, 9, 10, 11], which work well for AFM-SMFS traces coming from experiments performed in controlled conditions with purified proteins, perform poorly when applied to set of traces of unknown protein composition like those collected from native cell membranes. The most important stumbling block is possibly trace selection, because in the case of membrane proteins, complete unfolding is observed in less than 1% of the traces [10].

In this work, we introduce a procedure which allows the classification of highly heterogeneous SMFS datasets. The core idea in our procedure is detecting sets of traces with recurrent F-x patterns, emerging in a vast population of traces corresponding to statistically isolated events. To find these patterns we used density-peak clustering [12], an approach which allows detecting the maxima in multidimensional probability distributions using as input only the distance between each pair of data points (*the traces*, in the case of this work). We estimate the distance between pairs of traces using a modified version of the metric introduced by Marsico et al [9].The procedure we developed is fully automatic. In addition, it allows the processing of large amount of data in a reasonable computational time. It takes ~ 9 minutes to process 10^5 traces on a workstation with 16 CPUs.

We first show that our method can discriminate a single set of meaningful traces, corresponding to the unfolding of a protein, from a set of traces containing noise. We then show that the approach can discriminate between different types of meaningful traces, corresponding to the unfolding of different proteins. To this aim we first analyze a dataset containing subsets of traces corresponding to the unfolding of four different proteins. Next, we test our method on a highly-heterogeneous dataset of $\sim$ 400,000 traces from experiments performed in the native plasma membrane of the rod outer segment under physiological conditions.

2 Results

2.1 Algorithm overview and workflow.

The workflow of the algorithm we developed consists of the four major blocks depicted in Figure 1. The first block, "Cutting & filtering", aims at removing the physically irrelevant parts of the original trace, clearing the space to meaningful unfolding events. The filtering consists in discriminating spurious traces (Figure 1b). In the second block, a quality score is computed for each trace based on the features of its contour length (L_c) histogram. Depending on the score, a trace selection is performed, significantly reducing the total number of traces. For each pair of the remaining traces, a similarity distance, almost identical to the one used by Marsico et al [9], is computed and density-peak clustering is applied to classify the emerging recurrent F-x patterns into separate clusters (Figure 1d). In what follows, we provide a detailed description of each block of the algorithm.

2.2 Cutting and filtering.

Initially, each F-x curve is processed in order to remove all irrelevant parts of the signal. Typically, a F-x curve contains a *contact* and a *non-contact* part. The contact part comes from the interactions between the AFM tip and the membrane surface. This part starts with highly negative forces due to the upwards bending of the cantilever in the beginning of the retraction cycle. The non-contact part (or the tail) is noise coming from the free motion of the cantilever that is no longer in contact with the surface. This part is used to set the baseline of zero force. We remove the negative contact part and the tail of each trace as follows. For each trace, we find the first point at extension larger than 0 nm, followed by $n_{cont} = 20$ (all the parameters and their values are listed in Table 1) consecutive force measures having positive values. We mark this point as the *starting point* because this is where the positive contact part begins. We exclude from the analysis the signal preceding the starting point. In order to identify the non-contact part, we start from the end of the trace and move backwards until the force exceeds the range compatible with the free motion of the cantilever. In detail, we

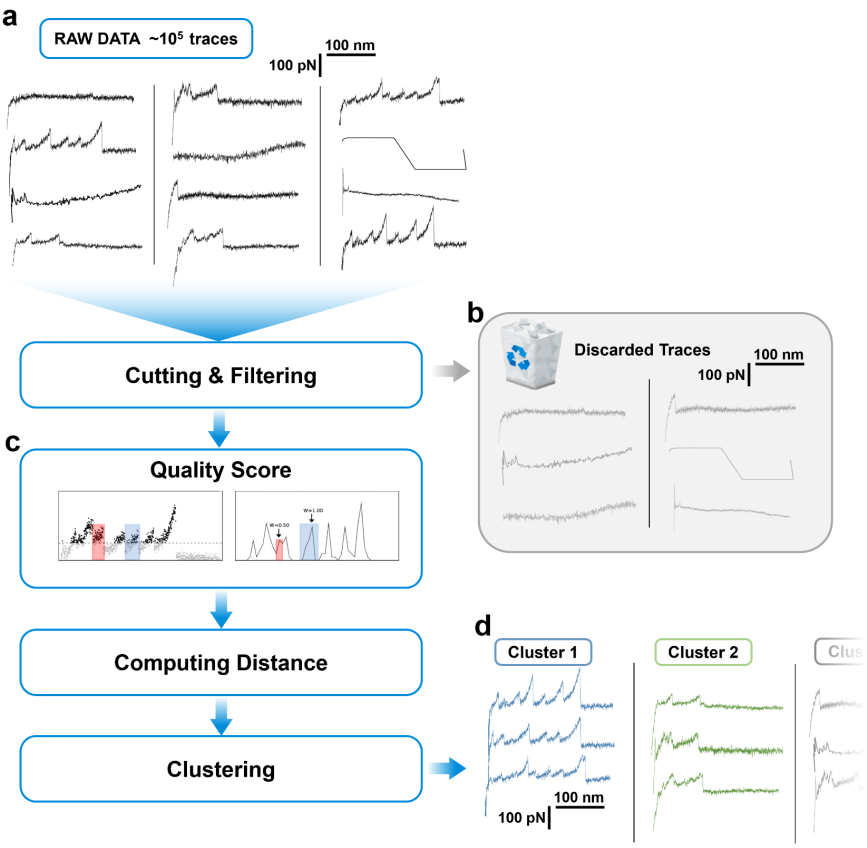

Figure 1: Block scheme of the algorithm.

estimate the standard deviation of the force σ_{NOISE} in 10 manually selected tails. This gives $\sigma_{NOISE} = 5.67$ pN. We then perform a linear fit to the last 8 nm of each trace, extending the window stepwise in the backward direction by 2 nm (hence considering the last 10 nm, 12 nm, 14 nm, etc.; see Figure S1) . At each step we compute the standard deviation from the fit and check whether it exceeds the cutting threshold, $\sigma_{cut} = 4\sigma_{NOISE}$. If not, we continue, otherwise we stop and cut the trace there. We assume that at this point the last force peak has been reached and the non-contact part has ended. In our procedure, the position of the last force peak determines the trace length.

At this point we store the traces on a regular grid with width $\Delta x_{interp} = 1$ nm, and we perform filtering, which aims at selecting only traces which are likely to correspond to the unfolding of a protein. In Figure S2 we show some examples of traces discarded by our procedure. A trace is discarded if it does not contain a detectable contact point, e.g. if the starting point of the contact part is blurred; if the points occupy an anomalously wide force range; if after the tail removal, the trace is shorter than a minimal length $L_{min} = 50$ nm and if the trace contains abnormal deflection points (with values larger than $x_{abn} = 5000$ nm or/and $F_{abn} = 5000$ pN), namely if the entire signal is shifted upwards with respect to the zero force baseline. The non-contact part in relevant traces is normally flat with fluctuations of the force compatible with σ_{NOISE}. By detecting the position of the last force peak, we obtain the total length of the non-contact part. This allows to compute its standard deviation from a horizontal zero-force line. If this deviation exceeds the threshold $\sigma_{tail} = 2\sigma_{NOISE}$, the trace is considered spurious and is discarded.

2.3 Quality score.

We then compute a quality score which we use for further selecting the meaningful F-x curves. The score we propose quantifies how well the experimental data satisfy the worm-like chain (WLC) model, which is the standard model used for the analysis of F-x curves [2, 3, 4, 6]. This choice excludes possibly meaningful traces corresponding to an unfolding not described by this model. In future applications one can consider removing or modifying this filter. According to the WLC model, a F-x curve represents the unfolding of different domains, each unfolding curve (each "tooth" in the pattern) being described by

$$F(x) = \frac{k_B T}{l_p}\left(\frac{1}{4}\left(1 - \frac{x}{L_c}\right)^{-2} + \frac{x}{L_c} - \frac{1}{4}\right) \tag{1}$$

where F is force, x is extension, k_B is Boltzmann's constant, T is temperature, l_p is the persistence length and L_c is the contour length of the domain. Usually, the WLC model is *assumed* and one retrieves the L_c corresponding to different domains by means of an L_c histogram [10, 11]. The WLC equation is inverted to find an L_c value for any x, and the resulting L_c values are plotted in a histogram. Ideally, the L_c histogram should consist of narrow peaks centered at the L_c values corresponding to the contour lengths of each domain. Thus, the L_c values corresponding to the maxima of the histogram are taken to be the contour length values for each domain. L_c histograms of meaningful traces are characterized by the presence of a few maxima, well separated by deep minima. We will define a score that quantifies how well the data agree with this expectation.

For each point in the F-x curve we compute L_c value by solving Equation 1. We use a persistence length $l_p = 0.4$ nm, which is considered appropriate for membrane proteins [3]. The L_c is computed in this manner in the force range from $F_{min}^{WLC} = 30$ to $F_{max}^{WLC} = 500$ pN which is the range of validity of the model [10].

A critical parameter for our algorithm is the bin width used for computing the histogram. Since the L_c value estimated by Equation 1 is unavoidably affected by noise, if the bin width is too small, the histogram is noisy. On the opposite, if the bin width is too large, peaks corresponding to the unfolding of different domains get merged. We have chosen a rather large bin size of 8 nm, a value corresponding to approximately 20 a.a., which is close to the typical length of a single transmembrane helix in membrane proteins [13]. The choice was also guided by visual inspection of the L_c histograms of proteins of known structure. We discuss how the results depend on the choice of this parameter in the Materials and Methods section.

Once we have the histogram, we find all maxima and minima. A maximum is considered meaningful if it is generated by more than 5 points and it includes more than 1% of the force measures of a trace.

Next, we compute score W quantifying the consistency of each maximum with the WLC model. We assume that a high quality peak has its two surrounding minima falling under $\frac{1}{2}$ of the peak height. We define $f_{left} = P_{left}/P_{max}, f_{right} = P_{right}/P_{max}$ where P_{max}, P_{left} and P_{right} are the probability densities of the maximum, of the minimum at its left and of the minimum at its right. The ideal trace will yield $f = \frac{1}{2}(f_{left} + f_{right}) \sim 0$. We embed this requirement by estimating the score of the peak as $W = \exp(-2f^2)$. If, for example, $P_{left} = 1$, $P_{right} = 2$ and $P_{max} = 16$ one gets $W = 0.98$. If instead $P_{left} = 13$ and $P_{right} = 14$, the peak has a low quality and one gets $W = 0.24$. In Figure S3 we provide a few examples of F-x curves, their L_c histograms and the W-score for some peaks.

Subsequently, we assign the corresponding peaks scores to all points in each trace. A score is assigned to a point in two steps: we assign the peak's score to all points in the L_c histogram belonging to the peak. If a point has a force smaller than 30 pN it is not assigned to any peak, since the WLC model is not valid for small forces. We therefore assign to it the same score of the first successive point whose force is larger than 30 pN. We apply this criterion only for points that are within 75 nm from the last point assigned to the peak (Figure S4). We selected this value by visual inspection of the traces, estimating the maximum widths of force peaks.

Finally, we sum up the scores for all points and we obtain the global score or the quality score of the trace, S_w. The higher the global score, the higher the overall quality of that trace. The ratio between the global score S_w and the trace length L is used to select high quality traces for subsequent analysis. If this ratio is smaller than 0.5, the trace is discarded (Figure S2 f). This is the same as saying: if more than half of the trace is inconsistent with the WLC model, it is a low quality trace and we are not interested in analyzing it. On the contrary, if more than half of the trace is consistent with the WLC model, it is possibly a meaningful trace. We will see that the final results we obtain are quite robust with respect to small variations in the value of this parameter. Therefore, the score/length threshold is not a critical parameter of our approach.

2.4 Compute distances.

The final goal of our procedure is finding in an automatic manner meaningful F-x curves bearing a specific unfolding pattern and grouping them into clusters based on their similarity to each other. We use the distance introduced by Marsico et al [9], which is based on dynamic programming alignment score, to evaluate the similarity between two traces. The distance

between traces a and b, denoted by d_{ab} is:

$$d_{ab} = 1 - \frac{S_D(N_a, N_b)}{N_{max}} \tag{2}$$

where $S_D(N_a, N_b)$ is the global alignment score, N_a is the length of trace a, N_b is the length of trace b, and $N_{max} = max(N_a, N_b)$. In our method, we modified the original scoring function used to evaluate match/mismatch score as follows:

$$M(i,j) = \begin{cases} 1 - \frac{|F_a(i) - F_b(j)|}{F_{scoring}} & if \quad |F_a(i) - F_b(j)| < F_{scoring} \\ -\frac{|F_a(i) - F_b(j)|}{F_{scoring}} & otherwise \end{cases} \tag{3}$$

where $F_a(i)$ and $F_b(j)$ are the forces in points i and j in traces a and b, and $F_{scoring} = 4\sigma_{NOISE}$. The difference between this scoring function and the one used in ref. [9] is that in the latter the force difference was divided by the average of the maximum force values ΔF_{max} in the two traces, and not by a single value $F_{scoring}$, equal for all the traces. If this choice is made, when two widely different traces both have high ΔF_{max}, their difference may be weighted less than the difference between two similar traces with low ΔF_{max}. In other words, the distance magnitude depends on ΔF_{max}, leading to low distance values for traces with high ΔF_{max}. Note that in ref. [9] this problem was absent, since the ΔF_{max} values were approximately uniform for all traces in the dataset. We are using the same gap penalties δ_1 and δ_2 like in ref. [9] (Table 1).

In order to make the method computationally more efficient, we compute the distance only between traces that differ by no more than 2 peaks in their L_c histograms or by no more than 20 % in terms of their trace length difference.

2.5 Density peak clustering.

To group the traces in clusters, we use the density peak clustering (DPC) algorithm [12]. In the datasets we are analyzing meaningful clusters correspond to small subsets of the traces, while most of the traces are statistically isolated events. In such a situation, partitioning algorithms like K-means are not fully appropriate, as classify in clusters all the traces, including isolated ones. DPC is suitable because it exclude automatically the outliers, which by definition do not belong to a density peak. The algorithm can be summarized in the following steps:

1. First, one computes the densities, representing the density of data points in the neighborhood of each point. The densities are computed with the k-nearest neighbor (k-NN) density estimator [14], as the ratio between k and the volume occupied by the k nearest neighbors:

$$\tilde{\rho}_i = \frac{k}{\omega_d r_{k,i}^d} \tag{4}$$

where d is the intrinsic dimension (ID) of the dataset [15], ω_d is the volume of the d-sphere with unitary radius and $r_{k,i}$ is the distance of point i from its k-th nearest neighbor. In DPC, the cluster membership of a data point is determined uniquely by the rank of its density, and not by the exact value of the density. Therefore, without loss of generality, instead of estimating the density by Equation 4, we estimate it as:

$$\rho_i = -\log r_{k,i} \tag{5}$$

It is easy to verify that the rank of ρ_i is equal to the rank of $\tilde{\rho}_i$, as the two are related by a simple monotonic transformation. Using this definition of the density we are not required to estimate the intrinsic dimension of the dataset. In addition, we multiply ρ_i by the score-length ratio of trace i. By doing so we assign bigger weight to the traces which satisfy better the WLC model.

2. One then finds the minimum distance between point i and any other point with higher density, δ_i:

$$\delta_i = min_{j:\rho_j>\rho_i}(d_{ij}) \tag{6}$$

where d_{ij} is the distance between points i and j. This will be used to idenitify local maxima of ρ_i.

3. Next, one finds the cluster centers, identified as density peaks, namely points with high values of ρ_i and δ_i. To identify the peaks, following ref. [12] we compute for each point $\gamma_i = \rho_i\delta_i$. Points with high values of γ_i are good cluster center candidates. One then sorts in descending order all points by the value of γ_i. The first point is a cluster center. The second point is also a cluster center, unless if it is at a distance smaller than r_{cut} from the first center, where r_{cut} is a free parameter of the approach (see below). One then considers the third point, which is a cluster center, unless if it is at a distance smaller than r_{cut} from the two points with higher γ. This test is then performed for all the points, finding in this manner all the cluster centers, which, by construction, will be further than r_{cut} from all the points with a higher γ.

4. Subsequently, following ref. [12] all points that are not centers are assigned to the same cluster of the nearest point with higher density.

In the standard implementation of DPC the distance between a cluster member and the cluster center can be arbitrarily large, if the density peak has an elongated shape. This is not appropriate for the analysis of SMFS traces, where the similarity between all the traces belonging to a cluster is essential. We therefore assume all the clusters are spherical, and consider meaningful the assignation to a cluster of a trace only if its distance from the cluster center is smaller than r_{cut} and smaller than its distance to any other cluster center. To determine an appropriate value for the parameter r_{cut} we performed a careful visual inspection on sets of traces characterized by an increasing distance from a high-quality trace. We concluded that at distances larger than 0.3 we can no longer be confident that two traces are likely to correspond to the same protein. We therefore fix $r_{cut} = 0.3$ and determine the size of the cluster core accordingly. In the following, to simplify the description of the results, we discard from the analysis clusters with less than 10 members.

2.6 Benchmark on the dataset 'Oocyte'

Dataset Oocyte contains 4,128 traces, 101 of which were selected based on their contour length and visual inspection and attributed to the unfolding of the membrane protein CNGA1 [4] thanks to molecular tags (see Materials and Methods for details). After filtering the traces with our procedure, their number was reduced to 459, which is approximately 11% of the total amount of traces. 67% of the previously selected CNG traces passed the filters. The traces were divided into 9 clusters. All selected CNG traces were found in cluster 2 and therefore, cluster 2 is the CNG cluster. With the data that are available, we cannot relate the remaining 8 clusters to proteins or further investigate their molecular origin.

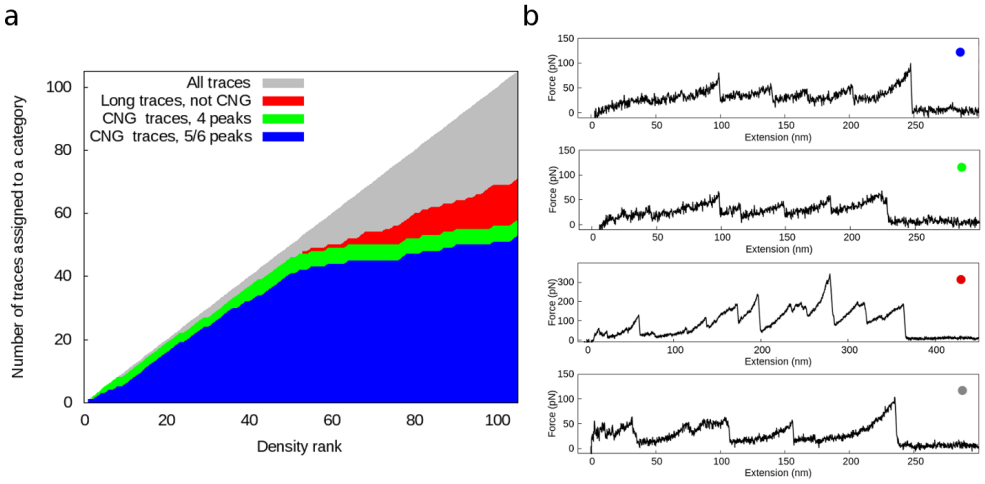

Figure 2: Graphical representation of the CNG cluster content. a. The cluster members are ranked by density in descending order. The blue area shows the manually selected CNG traces with 5 or 6 force peaks; the green area - manually selected CNG traces with 4 peaks; the red area - traces with contour length greater than 350 nm; the gray area corresponds to all traces assigned to the cluster. b. Representative traces for the different groups in panel a. The painted dot in the top right corner indicates the group affiliation.

We then analyzed more in detail the content of the CNG cluster. In Figure 2a we plot the cluster members ranked by their density in a descending order. The highest density traces are the CNG traces with 5 to 6 peaks (the blue area) followed by the CNG traces with 4 peaks (the green area). In Figure 2b we represent each group with a single F-x curve. When we looked more closely to the highest density region in Figure 2a, we noticed a thin gray line representing high density traces that haven't been included in the selection. We looked at these traces and found out that they are very similar to the cluster center of the CNG cluster (Figure S5). Therefore, these traces can be considered CNG traces which escaped manual selection. Remarkably, our procedure was able to detect previously unknown CNG traces and group them together in the right cluster.

2.7 Benchmark on the dataset 'Mixed'

Dataset Mixed contains four groups of selected F-x curves, representing the unfolding of four different proteins (see Materials and Methods for details). Each group is depicted in Figure 3a. Since all the traces of this dataset are manually selected, 77% of the traces passed the filters. In Figure 3b we show the distribution of the traces in the two-dimensional space of two representative descriptors, commonly used to discriminate among F-x curves: the maximum contour length (approximately the total length of the curve from the contact to the detachment of the polymer) and the average force of the peaks. This representation does not allow distinguishing the four groups: indeed, the traces belonging to groups 2, 3 and 4 occupy approximately the same region in that space of these descriptors.

Figure 3c shows that with our procedure the vast majority of traces belonging to each group was correctly assigned to a separate cluster. Our approach is therefore capable of reconstructing the ground truth classification in a group of traces which are not discriminated by standard descriptors. More in detail, the total number of clusters we obtained was 5. Cluster 1 contains the traces belonging to group 2, representing the unfolding of the tandem globular polyprotein Alpha3D+4xNUG2. Cluster 2 contains the CNG traces belonging to group 1. In cluster 3 we find the traces belonging to group 4. Only one or at most two traces

from each group were misassigned. The traces from group 3 are split in two clusters: $\sim 70\%$ are found in cluster 4 and $\sim 25\%$ in cluster 5 (Figure S6). Given that the force pattern is the same in the two clusters and the cluster core is more robust in cluster 4, cluster 4 should be considered as the cluster matching group 3. These results demonstrate that our algorithm is able to distinguish different unfolding patterns arising in the same dataset and to properly assign the corresponding F-x curves to different clusters without knowing *a priori* the protein composition.

2.8 Analysis of the dataset 'Rod'

Dataset Rod motivates our work since it poses a challenge to the traditional methods for AFM-SMFS data analysis. The analysis of this dataset can be considered blind, since the traces are collected in experiments performed in the plasma membrane of the rod outer segment (rod OS) under native conditions, and no preprocessing or selection was performed on the traces before our analysis. It contains 386,912 F-x curves, two orders of magnitude more than the dataset 'Oocyte'. After the removal of the non-contact part of each trace, filtering and score-based trace selection, the total number of traces is reduced to 14,910, $\sim 4\%$ of the initial amount of data.

With our approach we find 18 clusters. The nine most populated clusters are shown in Figure 4b. The other nine clusters are shown in Figure S7. In order to visualize the distribution of the most abundant traces in the relevant clusters, we used also here the maximum contour length and the mean peaks' force as descriptors (Figure 4a). In dataset 'Rod', by using these descriptors it is impossible to discriminate the different clusters, since they form a continuous distribution.

On the contrary, different patterns emerge in our clusters depicted in Figure 4b. Cluster 1 hosts traces with 3 to 4 major peaks and contour length $L_c \sim 80$ nm. In cluster 2 we find traces with 4, up to 6, force peaks and L_c values in the range 200-220 nm. Compared with the other clusters, cluster 3 hosts the longest traces with $L_c \sim$ 240-250 nm and 4 to 5 major force peaks. The traces in cluster 7 are shorter, $L_c \sim$ 130-140 nm, and have 3 to 4 force peaks. Cluster 9 contains traces with 2 to 3 major peaks and $L_c \sim$ 130-140 nm. Cluster 13 includes traces with L_c in the interval between 130 and 150 nm and 3 peaks. In cluster 14, the traces have 3 to 4 main force peaks and contour length 120-130 nm. The contour length of the traces in cluster 15 is ~ 100 nm and the main peaks are 3. Cluster 18 includes traces with $L_c \sim$ 180-190 nm and up to 3 force peaks.

Since two of the manually selected groups in dataset Mixed are originally from dataset Rod, we would like to see if these traces still form separate clusters. Indeed, some of the traces included in group 3 are found in the core of cluster 7. Instead, traces from group 4 are not found in any cluster core, which is consistent with the low quality of cluster 3 in dataset Mixed (Figure 3c).

Given that two of the dominant proteins in the plasma membrane of the rod OS are rhodopsin and the CNG channel, one might expect to find a rhodopsin cluster and a CNG cluster. The contour length of rhodopsin with the intact S-S bond is ~ 95 nm while it is $\sim$ 120 nm when fully stretched [16]. With our procedure we found two clusters with maximum contour length values between 100 and 120 nm: clusters 14 and 15 (Figure 4b), which might correspond to the unfolding of rhodopsin. The wild type CNGA1 channel of the Xenopus has a slightly different sequence than the bovine one overexpressed in the oocytes [4]. We expect the contour length of the fully-stretched CNG channel in the rod OS to be around 260 nm. The most likely candidate for the CNG cluster is cluster 3 which includes traces

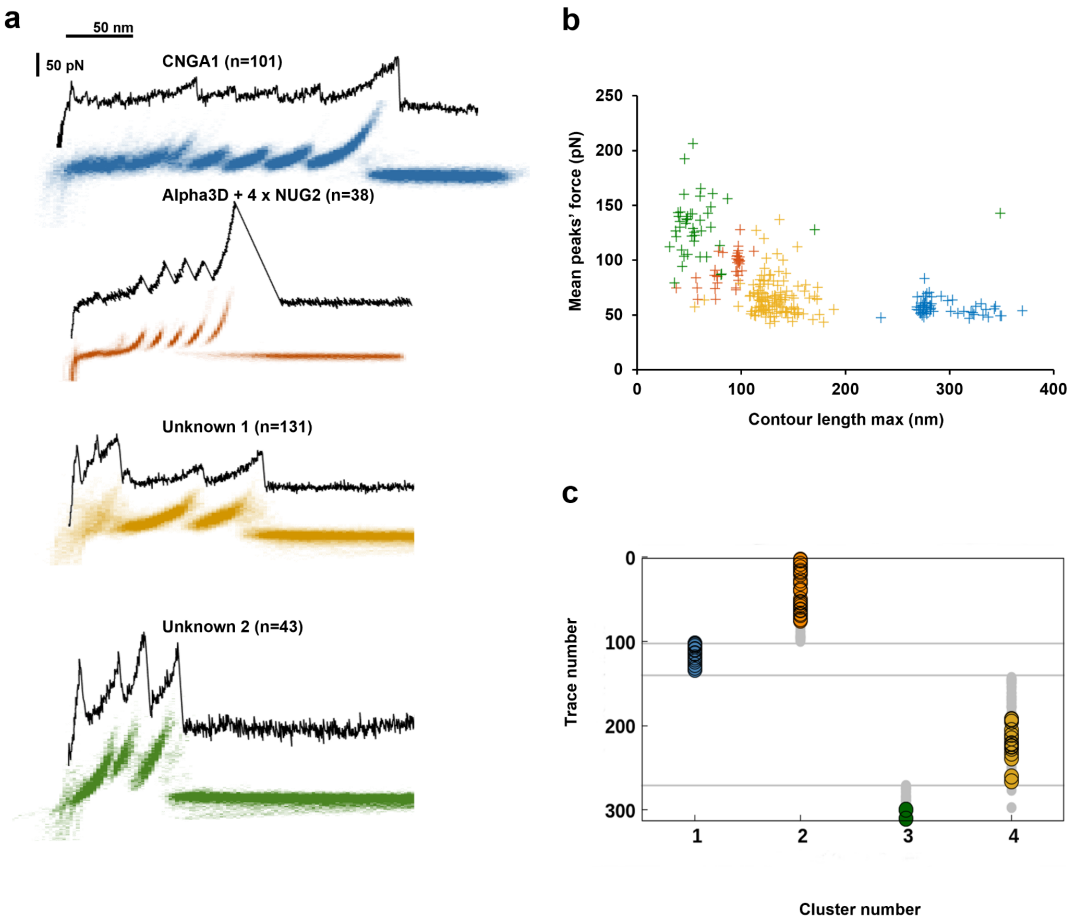

Figure 3: Results of the cluster analysis in dataset Mixed. a. F-x curves (black) and density plots (colored) of the four groups of traces included in dataset Mixed. The different colors indicate different groups of traces, i.e. different proteins. In blue, the traces representing the unfolding of the CNGA1 channel (Group 1); in red, the traces representing the unfolding of the globular tandem Alpha3D+4xNUG2 (Group 2); in yellow and green, two groups of traces with intra-group high level of similarity by visual inspection, associated with the unfolding of two unknown proteins extracted from dataset Rod (Group 3 and Group 4). b. 2D scatter plot representation of the traces in dataset Mixed: maximal contour length vs. average force of the peaks. c. Cluster assignation of the traces in dataset Mixed according to our procedure. The colors are the same as in plot a. Gray points represent all cluster members. Colored points represent only the cluster members at maximum distance 0.3 from the cluster center. Panel c illustrates that the clusters found by our approach are almost fully consistent with the ground truth classification in four groups, which are separated by the horizontal lines.

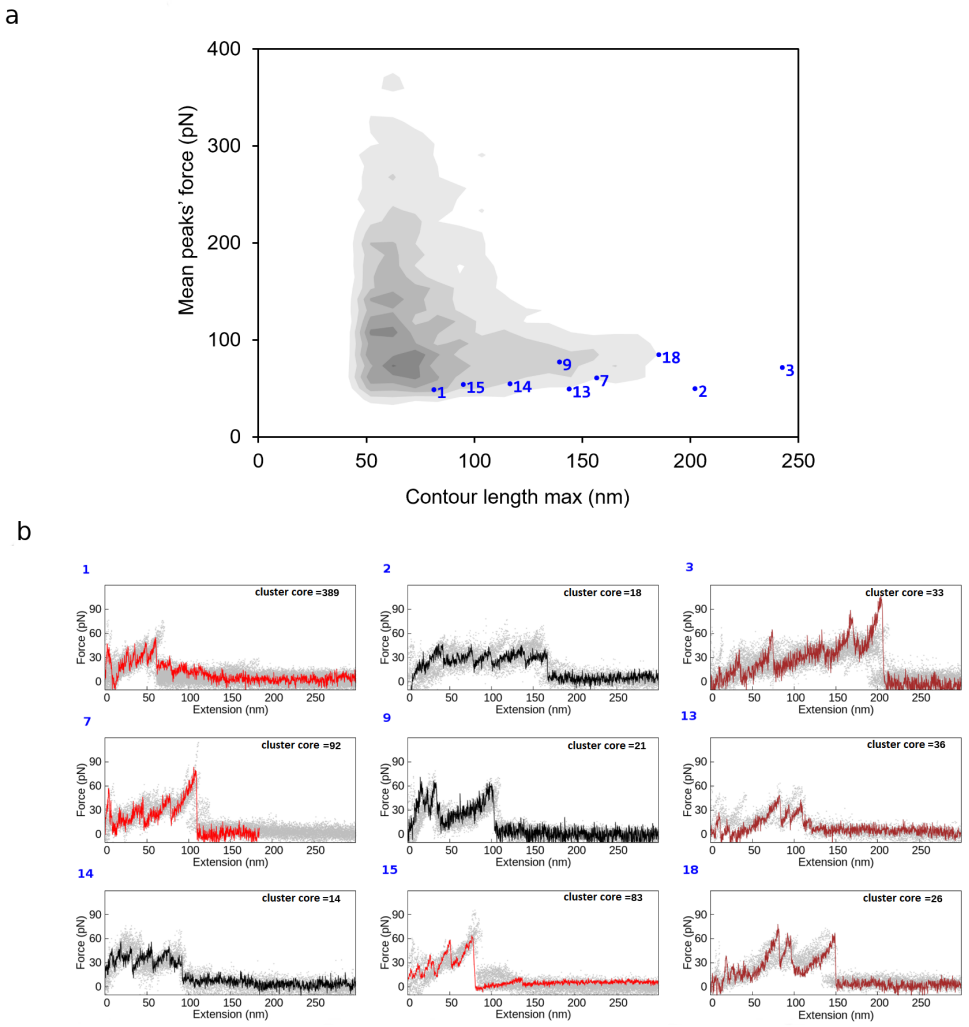

Figure 4: Results of the cluster analysis in dataset Rod. a. Isoline density plot of the ∼15,000 traces that survived the quality filter. The blue numbers indicate the position of the representative trace shown in panel b. b. Representative trace (solid lines) of each cluster with other traces belonging to the cluster (points) in the nine most populated clusters. The different color (red, brown, black) indicates the different cluster size. Red corresponds to the most populated clusters, brown to the one with intermediate size and black to the lowest populated clusters. The blue numbers in the top left corner indicate the cluster number. The cluster core size is given in the top right corner of each panel.

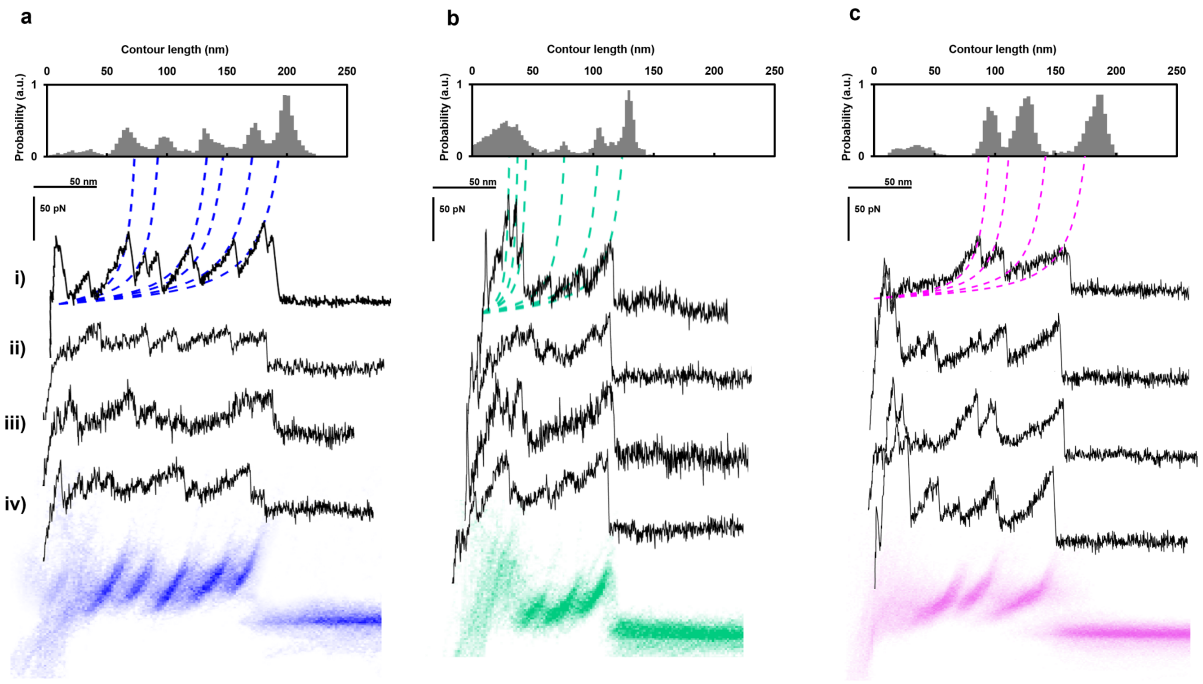

Figure 5: a, b, c. Various representations of cluster 2,9 and 18 found in dataset Rod. Contour length histograms showing the most frequent unfolding barriers (top); example of traces belonging to the clusters (middle); density plot of the clusters (enriched with the fingerprint-roi tool in Fodis [11]) (bottom). i) and ii) present all the relevant peaks while iii) and iv) show alternative unfolding pathways that are clustered together.

with L_c values up to 250 nm (Figure 4b).

In Figure 5, we show traces with unknown molecular origin, assigned to clusters 2, 9 and 18. The traces in cluster 2 (Figure 5a) are ∼200 nm long and they have 5 major unfolding peaks with spacing around 25 nm. The peaks show a certain variability in the occurrence, particularly in the range 100 nm $< L_c <$ 170 nm. Figure 5b displays the traces in cluster 9 with a highly conserved peak at L_c=130 nm and two minor peaks at 105 nm and 75 nm. As opposed to cluster 2, cluster 9 shows conservation of high force peaks at small L_c values ($<$ 50 nm) suggesting the presence of important unfolding events at the very beginning. We can't resolve them very well because they are hidden by the typical non-specific adhesion in the initial part of the curves. Cluster 18 (Figure 5c) instead shows three highly conserved peaks at L_c values 95, 120 and 190 nm, with force peaks occasionally appearing below 50 nm. The 50 nm gap between the second and the third peak is quite unusual in membrane proteins unfolding.

These results demonstrate that our method is capable of grouping into clusters traces with clean and well-defined force peaks (like in Figure 5a i) and ii)), as well as traces which might represent alternative unfolding pathways of the same protein (Figure 5a iii) and iv)). Of course, obtaining these clusters opens the problem of their biochemical interpretation, which in a complex environment such as a native membrane can be a non-trivial task. We therefore hope that this work will stimulate a dedicated research effort.

3 Discussion

To the best of our knowledge, no automatic procedure which allows the unsupervised classification of AFM-SMFS traces is currently available. The method proposed here is a step forward in this direction. Our approach is designed to face a specific challenge: analyzing the huge amount of data obtained by AFM-SMFS experiments on native membrane patches. Our method does not require any previous knowledge on the sample composition and the proteins contour length. In previous approaches [8, 9, 10, 11], the most significant filtering step is based on the expected contour length of the protein under investigation. Such an approach requires knowledge of the sample composition. It reduces tremendously the number of analyzed traces but is not suitable for data obtained from native cell membranes.

An important step in our procedure is trace selection based on a quality score which measures the consistency of each trace with the WLC model. By filtering traces according to this criterion one can miss some meaningful patterns that deviate from the WLC. If a model characterizing the force-extension features of these patterns was available, one could retain also traces consistent to that model. Dedicated experiments in controlled conditions like the ones performed by Takahashi et al [17] may offer a route to study these deviations. We also remark that by using a bin width of 8 nm for computing the L_c histograms, we are allowing for significant deviations of the persistence length [19], such that anomalous patterns may still survive the filtering. In other words, traces not perfectly adhering to the WLC model but still exhibiting the sawtooth pattern with well-defined peaks will survive the filter.

Following ref. [9], we use dynamic programming alignment to measure how similar to each other two traces are. In order to group similar traces into clusters, we use density-peak clustering [12]. The major advantages of this approach are that it does not require knowledge on the number of clusters in advance, and is able to distinguish "density peaks" formed by sets of similar traces from the background noise, formed by traces associated with isolated unfolding events.

We benchmarked our method on a data set containing a manually selected sample of CNG traces and $\sim$ 40 times more unevaluated traces. Our method successfully detected the CNG traces and grouped them in a separate cluster. Furthermore, the method proved to be able to distinguish between four groups of traces corresponding to the unfolding of four different proteins. Finally, we analyzed a dataset consisting of $\sim$ 400,000 traces of unidentified molecular origin from experiments in the plasma membrane of the rod outer segment. Our program turned out to be efficient taking only $\sim$ 30 minutes to process the entire data set revealing several unknown unfolding patterns calling for further molecular identification.

It is important to underline that the method is mainly aimed at finding statistically meaningful sets of similar traces which are likely to correspond to the unfolding of the same protein. After a meaningful pattern has been found, it is useful to adopt more conventional methods based on fingerprinting (like in Fodis [11]) to enrich the clusters with other traces, that can be initially discarded due to the filtering procedure.

We should also underline that the method is not designed to distinguish different unfolding pathways of the same protein. The filtering and the clustering procedure are by far too coarse for this scope. After the clusters have been found, one can further investigate them by one of the approaches in refs. [8, 9, 10, 11], which are much more appropriate for this scope.

In short, the present manuscript describes a method capable of extracting from a large amount of SMFS traces – in the order of millions – subsets of traces with a high reciprocal similarity. Despite limitations, the approach outperforms visual/manual selection, which

would be inconceivable for datasets of this size.

4 Materials and Methods

4.1 Experimental data

We tested our procedure on three sets of traces.

4.1.1 Dataset 'Oocyte'

The first data set contains 101 traces ascribed to the unfolding of the CNGA1 channel and 4,027 other traces generated in the same experiments. CNGA1 channels were expressed in *Xenopus laevis* oocytes with sample preparation, experimental procedure and selection described in ref. [4]. SMFS experiments were performed in the oocytes membrane with the AFM (NanoWizard 3, JPK). The cantilever was calibrated before the start of each experiment; its spring constant was ~ 0.08 N/m. The AFM tip was pushed into the surface and a force of 1 nN was applied for 0.5 s to enhance the non-specific binding to the proteins. The tip was retracted from the surface at pulling speed 500 nm/s. The selection of the CNG traces was based on two criteria: the contour length of the curves and their force pattern: according to the interpretation of the experimental data made in ref. [4], the last peak in the CNG traces has a L_c value larger than 220 nm and all CNG traces share a common unfolding fingerprint. The unfolding fingerprint consists of a peak at L_c around 100 nm corresponding to the unfolding of the cyclic nucleotide-binding (CNB) domain attached to the C-terminus; 3 or 4 force peaks between L_c 120 nm and 250 nm corresponding to the unfolding of the six transmembrane helices and the detachment peak. The 101 CNG traces include traces that satisfy these criteria and some other traces that miss a peak in the middle or the last peak assuming different unfolding pathways as suggested in ref. [4].

4.1.2 Dataset 'Rod'

The second data set comes from pulling SMFS experiments performed in the native plasma membrane of the rod outer segment (OS) of *Xenopus laevis* retinas. A detailed experimental protocol is provided in ref. [6]. Briefly, the AFM (NanoWizard 3, JPK) was used with cantilever with spring constant 0.08 N/m. The cantilever was calibrated before each experiment. The AFM tip was pushed into the sample surface with 1 nN force and held for 0.5 s. It was then retracted at constant speed 500 nm/s.

The plasma membrane hosts a variety of membrane proteins among which the CNG channels and rhodopsin are the most common [6]. As a consequence the dataset is highly heterogeneous and poses a challenge to traditional analysis tools. The entire dataset contains 386,912 F-x curves of unidentified molecular origin.

4.1.3 Dataset 'Mixed'

The third data set contains a mixture of four manually selected groups of F-x curves corresponding to the unfolding of different proteins.

1. Group number 1 includes the 101 manually selected CNGA1 traces included in dataset Oocyte.

2. Group number 2 includes 38 F-x curves representing the unfolding of a tandem globular polyprotein (Alpha3D + 4xNUG2) [20]. These experiments were performed by Marc-Andre LeBlanc and are available online on Dryad [21].

3. Group number 3 includes 131 traces from dataset Rod representing the unfolding of an unknown protein. To build this group we selected a template trace belonging to the dataset by visual inspection, and used the tool 'Fingerprint ROI' in the software Fodis [11] to mark the sawtooth pattern of the template, and find traces similar to that template.

4. Group number 4 includes 43 traces from dataset Rod representing the unfolding of another unknown protein and was made following the same protocol used for group number 3.

4.2 Robustness of the approach with respect to variations of the parameters

Parameter	Reference value	Description
Cutting and filtering		
n_{cont}	20	Minimum number of points with positive force values used to find the starting point in the contact part
σ_{NOISE}	5.67 pN	Standard deviation of the force where it is considered noise
σ_{cut}	$4\sigma_{NOISE}$	Threshold used for non-contact part removal
σ_{tail}	$2\sigma_{NOISE}$	Threshold used to detect spurious tails
L_{min}	50 nm	Threshold on the trace length used to discard short traces
x_{abn}	5,000 nm	Extension values above x_{abn} are considered abnormal
F_{abn}	5,000 pN	Force values above F_{abn} are considered abnormal
Δx_{interp}	1.0 nm	Grid spacing used to represent the traces
Estimating the WLC quality score		
l_p	0.4 nm	Persistence length
F_{min}^{WLC}	30 pN	Lower bound limit of the WLC force range
F_{max}^{WLC}	500 pN	Upper bound limit of the WLC force range
P_{peak}	1 %	Threshold for considering relevant a peaks in the L_c histogram
bin width	8 nm	L_c bin width used for the L_c histogram
Score threshold	0.5	Threshold on the quality score-length ratio used for trace selection
Computing distances		
δ_1	0.002 Δx_{interp}	Gap penalty in the first 10 nm of a trace; used in the dynamic programming alignment
δ_2	0.8 Δx_{interp}	Gap penalty in the rest of the trace; used in the dynamic programming alignment
$F_{scoring}$	$4\sigma_{NOISE}$	Match/mismatch threshold used in the distance computation
Clustering		
k	6	Number of nearest neighbors in the density estimator
r_{cut}	0.3	Cutoff distance. Only traces closer than r_{cut} to a cluster center are assigned to a cluster.

Table 1: Parameters appearing in the different blocks of the algorithm in Figure 1 and their corresponding reference values.

In Table 1 we list all the parameters in our method with their reference values. We performed extensive tests on the relevance of these parameters and in what follows we describe the effect of changing some of them. The results are summarized in Table 2. In this Table, we report the results obtained with our algorithm by varying one parameter at a time. We report in each case the number of common traces and the Normalized Mutual Information (NMI) between the reference clustering partition (obtained with the parameters in Table 1) and the clustering partition obtained by varying the parameter in the first column. The NMI plays the role of a correlation coefficient between clustering partitions: is equal to 1 if two partitions are fully consistent, except for a permutation of the cluster labels.

A first important parameter is σ_{NOISE}, the variance of the force in the non-contact part of a trace. σ_{NOISE} is used to define several other parameters: σ_{cut}, used to remove the non-contact part of a trace, σ_{tail}, used to detect traces with problematic tails and $F_{scoring}$, used in the distance computation. We remind that σ_{NOISE} is not a free parameter, since it can be computed directly from the traces. It mostly depends on the cantilever spring constant. Thus, it varies between different experiments. As shown in Table 1, if one varies it from 6 pN to 8 pN the number of common traces is only 260, approximately one third of the total. The small number of common traces indicates that it is important estimating the value of σ_{NOISE} properly. The NMI is 0.917, a value which indicates that the clustering classification of the common traces is consistent.

We also tested the dependence of the results on the σ_{cut} value. By increasing σ_{cut} we are making the cutting criterion more strict, which might lead to incorrect non-contact part recognition, namely to removal of relevant parts of the spectra. As a result high quality traces selected in the reference might get discarded. In fact, we find 440 common traces with the reference. Also in this case, the NMI is very high, indicating that the common traces are classified basically in the same manner.

Next, we considered the "peak width" parameter, used to assign score to all points belonging to a peak properly. We changed it from 75 to 50 nm. By making the peak width smaller, the overall global score decreases. As a result, the number of traces passing the score-based selection slightly decreases. Consistently, we observe a decrease in the number of common traces. The NMI remains quite high indicating good correlation between the final clustering results.

The persistence length is a key parameter in the WLC model. The reference value, 0.4 nm is the one most commonly used for membrane proteins, even if in the literature there are examples of SMFS data analysis using different l_p values, from 0.2 nm up to 0.9 nm [18, 19]. To test the dependence of the final results on the l_p value, we changed l_p to 0.5 nm. As a consequence, we observe more significant deviations of the final results from the reference, which is not surprising given that the choice of l_p alters the quality of the WLC fit.

Another important parameter in our approach is the bin width of the L_c histogram. The choice of the reference value, 8 nm, is commented in the Results section. Here, we performed tests with bin widths 7 and 9 nm. The number of common traces is 374 in the first case and 515 in the second case. The NMI values remain high. The traces that are selected change if one varies L_c, but the cluster classification is remarkably robust also with respect to this parameter.

Our procedure is also robust with respect to variations in the score-based threshold used for trace selection, the value of k_{NN} used in the density estimation, and the cutoff radius used for clustering. In all these cases the number of common traces is well preserved and the NMI indicate that the clusters are practically unchanged with respect to the reference.

Parameter	N. traces	N. common	NMI
Reference	781		
$\sigma_{NOISE} = 8$ pN	823	264	0.917
$\sigma_{cut} = 5\sigma_{NOISE}$	740	440	0.964
peak width=50 nm	688	350	0.993
$l_p = 0.5$ nm	804	398	0.962
bin width=7 nm	764	374	0.953
bin width=9 nm	787	515	0.968
$k_{NN} = 4$	742	540	0.980
$k_{NN} = 8$	757	652	0.994
$k_{NN} = 10$	902	645	0.994
Score threshold=0.4	1009	712	0.988
Score threshold=0.6	673	619	0.99803
$r_{cut} = 0.4$	629	613	0.993

Table 2: Normalized mutual information and number of common traces measured for different parameters setup and the reference setup of Table 1.

References

[1] Andreas Engel and Hermann E Gaub. Structure and mechanics of membrane proteins. *Annu. Rev. Biochem.*, 77:127–148, 2008.

[2] Matthias Rief, Mathias Gautel, Filipp Oesterhelt, Julio M. Fernandez, and Hermann E. Gaub. Reversible unfolding of individual titin immunoglobulin domains by afm. *Science*, 276(5315):1109–1112, 1997.

[3] F. Oesterhelt, D. Oesterhelt, M. Pfeiffer, A. Engel, H. E. Gaub, and D. J. Müller. Unfolding pathways of individual bacteriorhodopsins. *Science*, 288(5463):143–146, 2000.

[4] Sourav Maity, Monica Mazzolini, Manuel Arcangeletti, Alejandro Valbuena, Paolo Fabris, Marco Lazzarino, and Vincent Torre. Conformational rearrangements in the transmembrane domain of cnga1 channels revealed by single-molecule force spectroscopy. *Nature communications*, 6:7093, 2015.

[5] Shiho Kawamura, Moritz Gerstung, Alejandro T Colozo, Jonne Helenius, Akiko Maeda, Niko Beerenwinkel, Paul S-H Park, and Daniel J Müller. Kinetic, energetic, and mechanical differences between dark-state rhodopsin and opsin. *Structure*, 21(3):426–437, 2013.

[6] Sourav Maity, Nina Ilieva, Alessandro Laio, Vincent Torre, and Monica Mazzolini. New views on phototransduction from atomic force microscopy and single molecule force spectroscopy on native rods. *Scientific reports*, 7(1):12000, 2017.

[7] Nicola Galvanetto, Sourav Maity, Nina Ilieva, Alessandro Laio, and Vincent Torre. Unfolding and identification of membrane proteins from native cell membranes. *bioRxiv*, 2019.

[8] M Kuhn, H Janovjak, M Hubain, and DJ Müller. Automated alignment and pattern recognition of single-molecule force spectroscopy data. *Journal of microscopy*, 218(2):125–132, 2005.

[9] Annalisa Marsico, Dirk Labudde, Tanuj Sapra, Daniel J. Muller, and Michael Schroeder. A novel pattern recognition algorithm to classify membrane protein unfolding pathways

with high-throughput single-molecule force spectroscopy. *Bioinformatics*, 23(2):e231–e236, 2007.

[10] Patrick D Bosshart, Patrick LTM Frederix, and Andreas Engel. Reference-free alignment and sorting of single-molecule force spectroscopy data. *Biophysical journal*, 102(9):2202–2211, 2012.

[11] Nicola Galvanetto, Andrea Perissinotto, Andrea Pedroni, and Vincent Torre. Fodis: software for protein unfolding analysis. *Biophysical journal*, 114(6):1264–1266, 2018.

[12] Alex Rodriguez and Alessandro Laio. Clustering by fast search and find of density peaks. *Science*, 344(6191):1492–1496, 2014.

[13] Albert L. Lehninger. *Lehninger principles of biochemistry*. Worth Publishers: New York, 2000.

[14] Naomi S Altman. An introduction to kernel and nearest-neighbor nonparametric regression. *The American Statistician*, 46(3):175–185, 1992.

[15] Elena Facco, Maria dErrico, Alex Rodriguez, and Alessandro Laio. Estimating the intrinsic dimension of datasets by a minimal neighborhood information. *Scientific reports*, 7(1):12140, 2017.

[16] K Tanuj Sapra, Paul S-H Park, Slawomir Filipek, Andreas Engel, Daniel J Müller, and Krzysztof Palczewski. Detecting molecular interactions that stabilize native bovine rhodopsin. *Journal of molecular biology*, 358(1):255–269, 2006.

[17] Hirohide Takahashi, Felix Rico, Christophe Chipot, and Simon Scheuring. α-helix unwinding as force buffer in spectrins. *ACS nano*, 12(3):2719–2727, 2018.

[18] Hongbin Li, Wolfgang Linke, Andres Oberhauser, Mariano Carrin-Vzquez, Jason Kerkvliet, Hui Lu, Piotr Marszalek and Julio Fernandez. Reverse engineering of the giant muscle protein titin *Nature*, 418:998–1002, 2002.

[19] Atom Sarkar, Sofia Caamano, and Julio M Fernandez. The elasticity of individual titin pevk exons measured by single molecule atomic force microscopy. *Journal of Biological Chemistry*, 280(8):6261–6264, 2005.

[20] Patrick R Heenan and Thomas T Perkins. Feather: Automated analysis of force spectroscopy unbinding and unfolding data via a bayesian algorithm. *Biophysical journal*, 115(5):757–762, 2018.

[21] Patrick R Heenan and Thomas T Perkins. Data from: Feather: automated analysis of force spectroscopy unbinding and unfolding data via a bayesian algorithm. https://datadryad.org/resource/doi:10.5061/dryad.1615c2p, 2018.

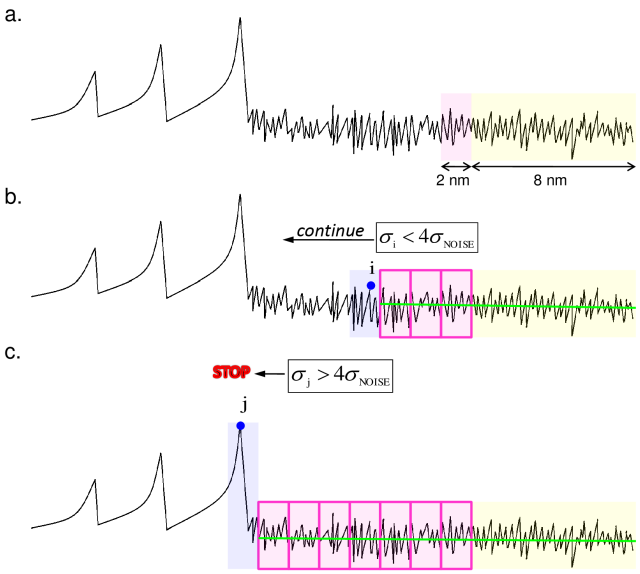

Figure S1: A schematic representation of the removal procedure of the non-contact part of a F-x curve. a. A drawing of a F-x curve. The last 8 nm in the non-contact part of the tail are highlighted in yellow. The following extension of 2 nm is highlighted in pink. b. The green line represents the linear fit to the last 8 nm (highlighted in yellow) of the tail plus three extensions of 2 nm each (highlighted in pink). The standard deviation of the noise is denoted as σ_{NOISE} and the threshold used to cut the traces is $4\sigma_{NOISE}$. The highlighted blue area shows the upcoming 2 nm window in which the standard deviation of the point i, σ_i is compared to the $4\sigma_{NOISE}$ threshold. σ_i is smaller than $4\sigma_{NOISE}$ and the procedure continues. c. The standard deviation of the point j, σ_j is larger than $4\sigma_{NOISE}$ and the procedure stops. The point j is the last point included in the trace. All points coming after j are removed.

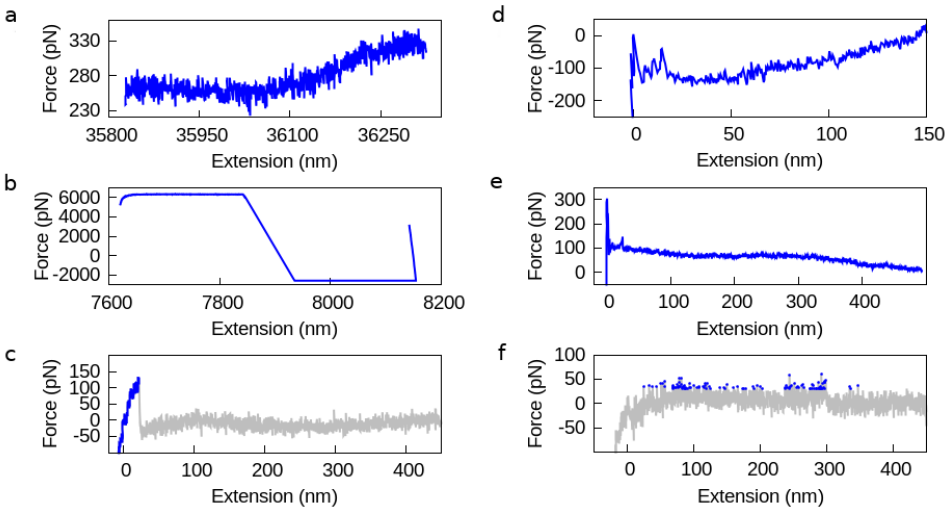

Figure S2: Discarded traces. a. A trace with undetectable contact point; b. A recording failure of a trace; c. A trace shorter than 50 nm after the removal of the non-contact part (highlighted in gray); d,e. Traces with abnormal deflection of the baseline; f. A trace with score-length ratio smaller than 0.5. The points which can be adequately described by the WLC model are shown in blue.

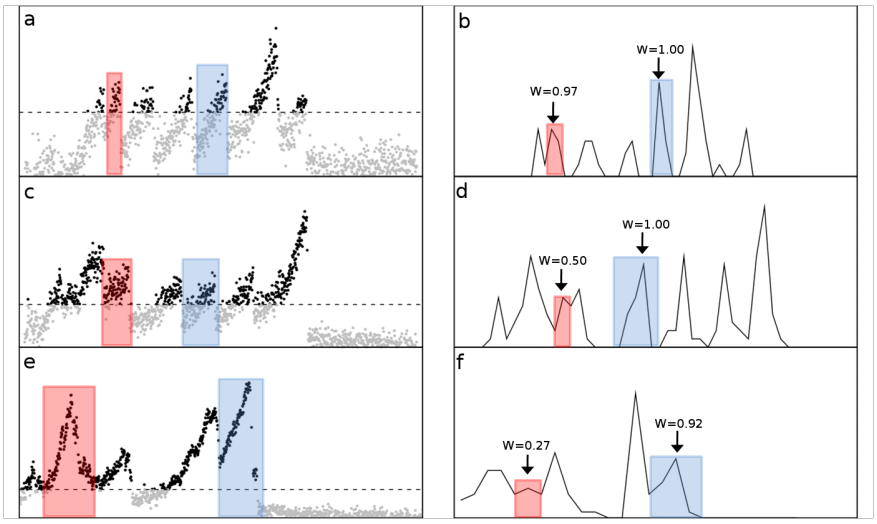

Figure S3: Examples showing the relation between the original F-x curves, their L_c histograms and the peaks WLC consistency scores, W. Panels a,c and e are showing three F-x curves. The dotted line crosses the curves at the 30 pN threshold set by the WLC model. All points above the line (the black points) are used to compute the corresponding L_c histograms, shown in panels b, d and f. Panels b, d and f show the corresponding L_c histograms, and the W-score of the peaks highlighted in red and blue, both in the histograms and in the original curves.

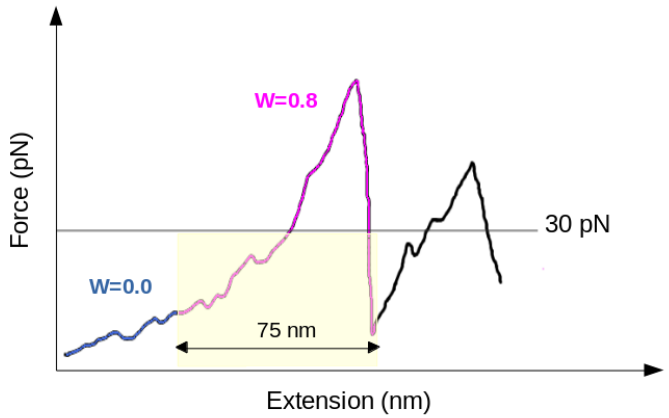

Figure S4: A scheme representing the second step in the score assignation process. At this step the peak score, depicted in pink is assigned also to points belonging to the peak but with forces below 30 pN and at distance 75 nm from the last peak point (the yellow area). The 30 pN threshold is set by the WLC model limitations. The 75 nm range was chosen based on visual inspection of the traces, looking at the maximum extension of relevant force peaks.

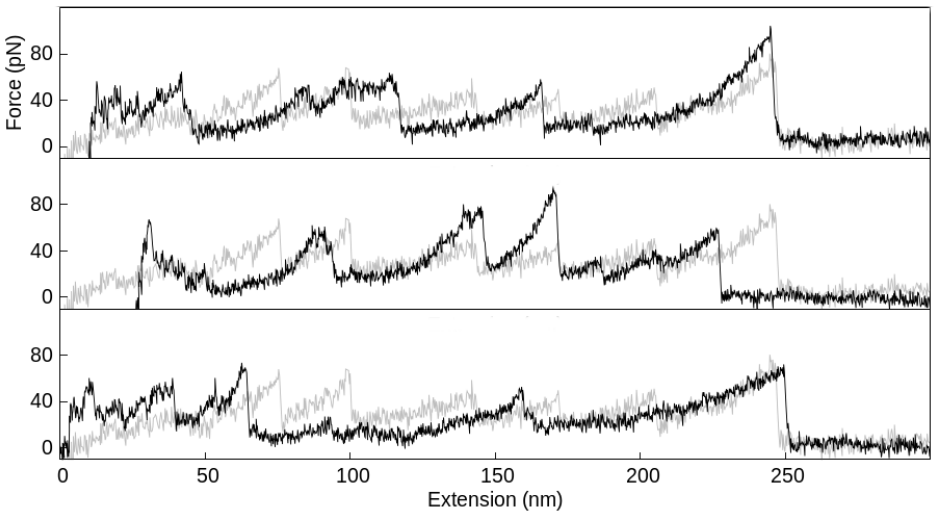

Figure S5: Potential CNG traces, which escaped the visual inspection of the traces in dataset 'Oocytes'. From top to bottom: three high density traces (depicted in black) assigned to the CNG cluster by our procedure plotted with the CNG cluster center (depicted in gray).

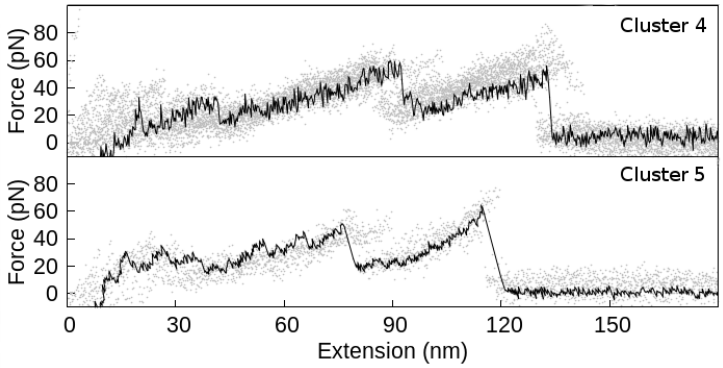

Figure S6: Graphical representation of clusters 4 and 5, which encompass the traces from group 3 in dataset 'Mixed'.

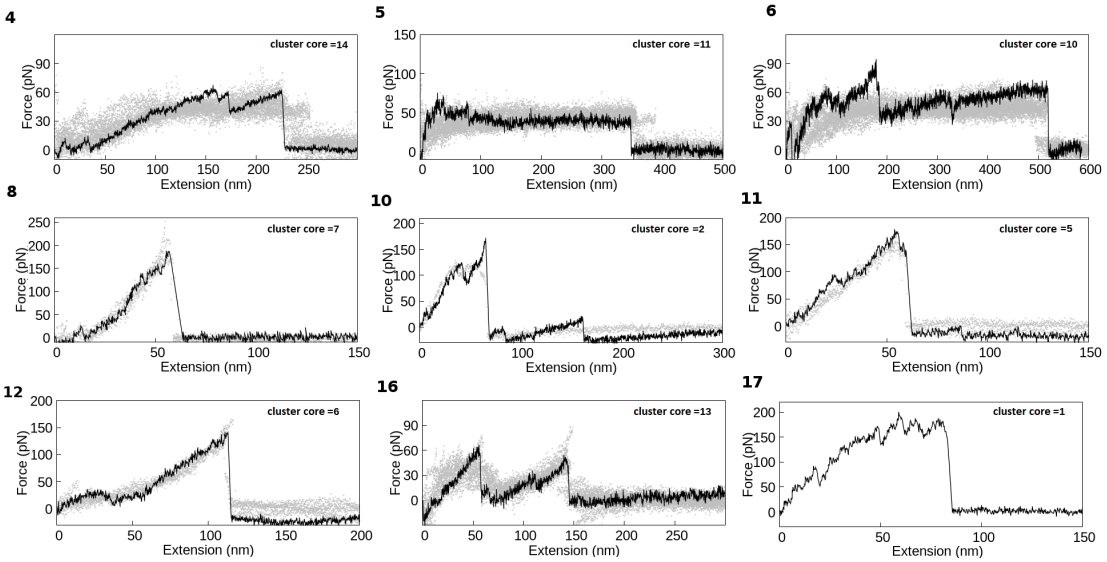

Figure S7: Low population clusters found in dataset Rod. Cluster representative trace (solid lines) with a cloud of similar cluster members (with points). The cluster number is indicated on top of each plot; the cluster core size is given in the top right corner of each panel.

Unfolding and identification of membrane proteins from native cell membranes

Nicola Galvanetto[1,], Sourav Maity[2], Nina Ilieva[1], Zhongjie Ye[1], Alessandro Laio[1,3], Vincent Torre[1]*

[1] International School for Advanced Studies (SISSA), via Bonomea 265, Trieste 34136, Italy. [2]Moleculaire Biofysica, Zernike Instituut, Rijksuniversiteit Groningen, Nijenborgh 4, 9747 AG Groningen, Netherlands. [3]The Abdus Salam International Centre for Theoretical Physics (ICTP), Strada Costiera 11 - 34151 Trieste, Italy.
**email: nicola.galvanetto@sissa.it*

Abstract

Is the mechanical unfolding of proteins just a technological feat applicable only to synthetic preparations or is it applicable to real biological samples? Here, we describe a method providing all the necessary steps to deal with native membranes, from the isolation of the plasma membrane of single cells, to the characterization and identification of the embedded membrane proteins. We combined single-molecule force spectroscopy with an automatic pattern classification of the obtained Force-distance curves, and we provide a Bayesian identification of the unfolded proteins. The Bayesian identification is based on the cross-matching of Mass Spectrometry datasets with proteomic databases (Uniprot, PDB). We applied this method to four cell types where we classified the unfolding of 5-10% of their total content of membrane proteins. The ability to mechanically probe membrane proteins directly in their native membrane enables the phenotyping of different cell types with almost single-cell level of resolution.

Introduction

Much of what we know about the mechanics of cell membranes[1–3] and polymers[4,5] comes from atomic force microscopy (AFM) and to its ability to work at the nanoscale. Single-molecule force spectroscopy (SMFS) in particular uses an AFM to apply a force able to unfold directly a single molecule or a protein. The obtained force-distance (F-D) curves encode the unfolding pathway of the molecule, allowing the identification of folded and unfolded regions from the analysis of the sequence of force peaks[8]. SMFS has been mostly used to study the mechanics of purified proteins in solution or reconstituted in a lipid bilayer. However, the information that is possible to extrapolate from the F-D curves (e.g. mechanical stability[9,10], structural heterogeneity[11]) depends on the physical and chemical properties of the cell membrane[12,13], therefore it is desirable to unfold membrane proteins in their original membrane.

The obvious questions are: is the mechanical unfolding of proteins just a technological feat applicable only to synthetic preparations or is it applicable to real biological samples? If this is technically feasible, how can we identify the molecular structure of the unfolded protein among the plethora of native membrane proteins? What additional information can we get?

In the present manuscript we describe a methodology, both experimental and theoretical, to unfold and recognize membrane proteins obtained from native cell membranes (Fig. 1 a). Firstly, we developed a technique to extract the membrane from single cells. Secondly, by using AFM-based SMFS we obtained hundreds of thousands of F-d curves in experiments using real biological membranes. Thirdly, we developed a filtering and clustering procedure based on pattern recognition that is able to detect clusters of similar unfolding curves among the thousands of F-d curves. Fourthly, we implemented a Bayesian meta-analysis of mass spectrometry libraries that allowed us to identify the candidate proteins. This Bayesian identification is further refined by cross-analyzing additional databases so to have very few

candidates for the obtained clusters of F-d curves. We focused on native membrane proteins from hippocampal neurons, dorsal root ganglia (DRG) neurons, and the plasma and disc membrane of rod outer segments, which represent the only native sample that were approached in the past[14]. We validate the identification using the known unfolding of two proteins from rod OSs: cyclic nucleotide gated (CNG) channels[12] and rhodopsin molecules[15].

Besides the identification, the proposed methodology generates as by-product the phenotyping of the membrane proteins content of specific cells that may become relevant in biomedical applications.

Results

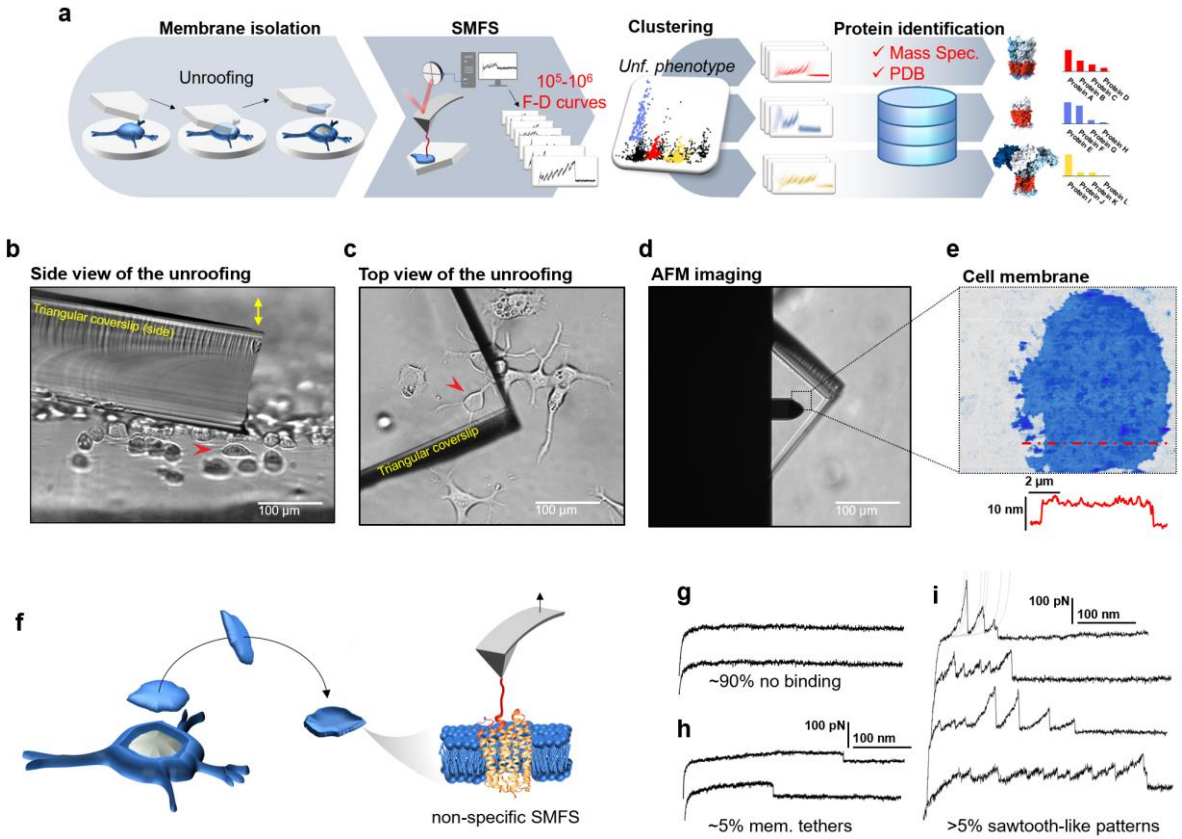

Figure 1 | Experimental method for single-cell membrane isolation and protein unfolding. ***a****, workflow of the method in four steps: isolation of the apical membrane of single cells; AFM-based protein unfolding of native membrane proteins; identification of the persistent patterns of unfolding and generation of the mechanical phenotype; Bayesian protein identification with mass spectrometry, Uniprot and PDB.* ***b****, side view and* ***c****, top view of the cell culture and the triangular coverslip approaching the target cell (red arrow) to be unroofed.* ***d****, positioning of the AFM tip in the region of unroofing.* ***e****, AFM topography of the isolated cell membrane with profile.* ***f****, cartoon of the process that leads to SMFS on native membranes. Examples of F-D curves of* ***g****, no binding events;* ***h****, membrane tethers that generate constant viscous force during retraction;* ***i****, sawtooth-like patterns, typical sign of the unfolding of a protein.*

Unfolding proteins from isolated cell membranes.

In order to study the unfolding of membrane proteins from their native environment, we optimized an unroofing method[16] to isolate the apical part of cell membranes containing primarily membrane proteins with negligible contamination of cytoplasmic proteins (Supplementary Fig. 1). We sandwiched a single cell or neuron between two glass plates, i.e. the culture coverslip and another mounted on the AFM itself (see Fig. 1b-c, triangular

coverslip). The triangular coverslip is coated with polylysine which favors membrane adhesion. When adhesion is reached, a rapid separation of the plates, driven by a loaded spring, permits the isolation of the apical membrane of the cell (see Fig. 1d-e, Supplementary Fig. 1). The method is reliable (n=42, ~80% success rate) with cell types grown on coverslips (epithelial cells and neurons). With non-adherent cells, like freshly isolated rods, we isolated the membrane with a lateral flux of medium[17] (see Methods).

After membrane isolation, we imaged the membrane with the AFM (Fig. 1f) and we verified that the isolated membrane patches have a height of 5-8 nm with rugosity in the order of 1 nm. Then, we performed standard SMFS[18] with non-functionalized tips collecting 301,654 curves on the hippocampal membrane, 213,468 curves on DRG, 386,128 on rods and 221,565 on rod discs. Of the obtained curves, the ~90% shows no binding (Fig. 1 g), ~5% shows plateau ascribable to membrane tethers[19](Fig. 1 h), while the remaining >5% displays the common sawtooth-like shape that characterizes the unfolding of proteins[18,20](Fig. 1 i). Indeed, F-D curves representing unfolding events are constituted by a sequence of rising concave phases followed by vertical jumps, where the rising phases fit the worm-like chain (WLC) model with a persistence length of ~0.4nm indicating the stretching of an unstructured aminoacidic chain[21]. In these cases the AFM tip binds non-specifically the underlying proteins through physisorption[8].

The architecture of membrane proteins and their unfolding.

The Protein Data Bank (PDB) contains 8662 entries that are also annotated in the Orientation of Proteins in Membrane (OPM)[22,23] providing the information of the position of each aminoacid relative to the cell membrane. The OPM is therefore a useful resource from which we extrapolated statistics on the architecture of membrane proteins. We categorized all these 8662 proteins in eight different classes based on their architecture (Fig. 2 a, see Methods for details). 53% of the resolved membrane proteins are peripheral membrane proteins anchored to the membrane, of which the two thirds are located extracellularly (class VIII of Fig. 2 a), thus not accessible by the AFM tip in our experiments (Fig.1). The intracellular peripheral membrane proteins (class VII) can be unfolded only if they tightly bound to the membrane. The remaining 47% of these proteins are transmembrane proteins of which only the 7% have both the C- and the N-terminus in the extracellular side (class VI). Of the eight classes shown in Fig. 2 a, five (I-V) have already been investigated in purified conditions[12,14,18,24,25] and the obtained F-d curves display the usual sawtooth-like, i.e. the piece-wise WLC behavior that is present also in our F-d curves. Class VIII is not expected to be present in our experiments as it cannot attach to a cantilever approaching from the intracellular side, while proteins of Class VI and VII can be pulled by a cantilever approaching from the cytoplasmic side.

Analysis of SMFS data from native cell membranes

Membrane proteins, when pulled, generate their own characteristic pattern of unfolding which is used for their selection[26,27]. Visual inspection shows that the obtained F-d curves contain recurrent patterns of unfolding similar to those obtained in purified conditions when pulled from either the C or N-terminus[18,24,25]. However, the attachment to either the C and N-terminus and the resulting complete unfolding of a single protein is not the only possible event that occur in our experiments. On the basis of the architectural analysis, we have considered three additional cases: i) the simultaneous attachment of two or more proteins to the tip[28], ii) the incomplete unfolding of the attached protein[14], iii) the binding of the AFM tip to a loop of the protein instead of to a terminus end (Fig. 2 c-f).

i) Attachment of multiple proteins (Fig. 2 d): the blind movements of the tip apex (radius of curvature 10-20 nm) leads the tip landing in random configurations on the sample so that it could bind simultaneously to multiple proteins. Since the ratio between non-empty curves over all curves is ~ 5 %, it follows that the binding probability is also close to 5%: the probability to bind 2 proteins at the same time is therefore its square (~0.25%). The attachment of multiple proteins occurs 20 times less frequently than the single attachment, and it will happen with combinations of different protein species and the resulting F-d curves will not have a recurrent

pattern. Furthermore, when the two chains are unfolded together, the resulting spectrum is the sum of the two individual spectra: that causes deviations of the measured persistence length in the part of the curve where both chains are stretched (Supplementary Fig. 2). The simultaneous unfolding of multiple proteins is also characterized by the doubling of the peaks and evident changes in the range of the forces and persistence length (Fig. 2 d and g, Supplementary Fig. 2).

ii) Incomplete unfolding of the protein (Fig. 2 e): if the tip prematurely detaches from the terminus, the resulting F-d curve will display a similar but shorter pattern compared to a complete unfolding (Fig. 3 c). The fraction of curves that prematurely detaches is reported to be ~23% of the fully unfolded proteins[14], but this value could vary from protein to protein.

iii) Binding of the AFM tip to a loop (Fig. 2 f): the unfolding from a loop is equivalent to the attachment of multiple proteins because the tip unfolds two chains at the same time. However, if the attachment of the cantilever tip to a loop occurs with some consistency—like with the C- or the N-terminus—we will obtain a recurrent pattern with the features described in case i) (deviation of persistence length during intersection, 2 major levels of unfolding force).

We have heuristics to identify all these cases (see also Supplementary Fig. 2), and in particular case i) and ii) are expected to be governed by stochasticity so that the corresponding F-d curves occur *without recurrent patterns* and therefore we focused on the detection of F-d curves with clear recurrent patterns.

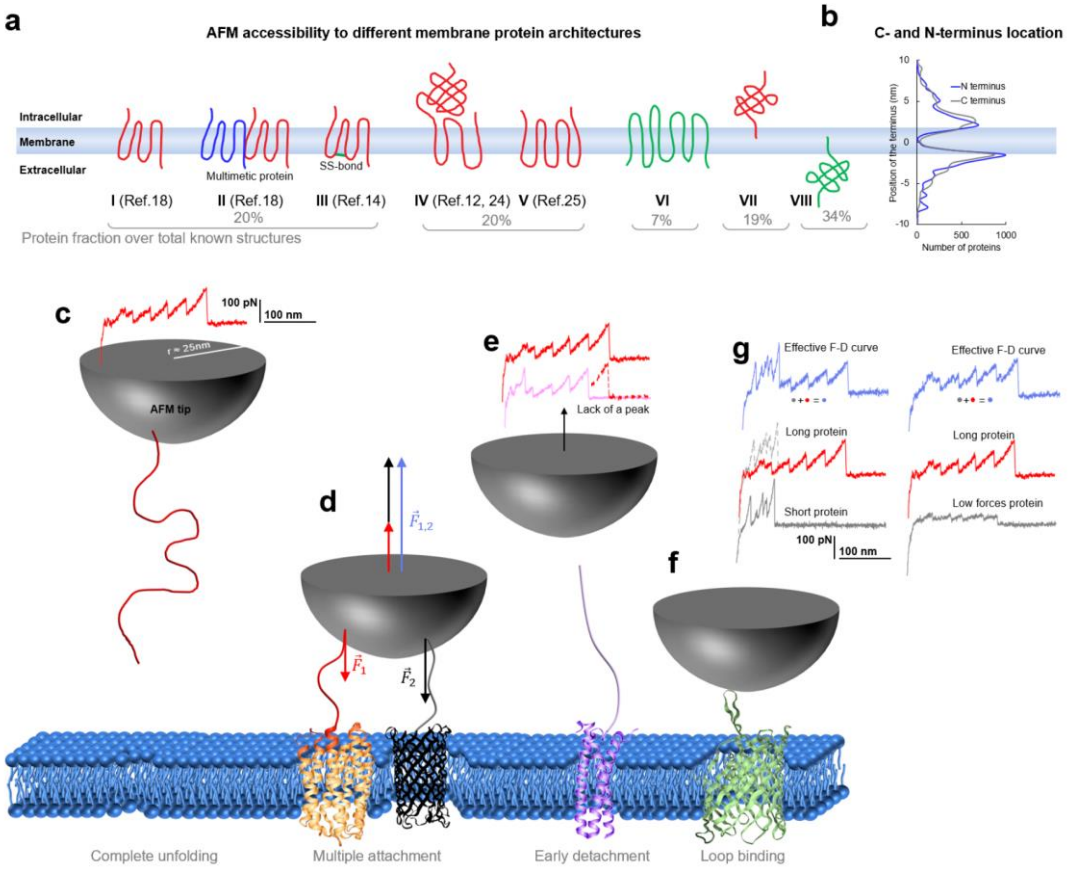

Figure 2 | ***Membrane proteins architectures.*** ***a****, eight classes of membrane proteins and their fraction over all resolved proteins present in the PDB-OPM.* ***b****, position of the termini relative to the center cell membrane along the axis perpendicular to the membrane. Cartoon representing* ***c****, complete unfolding of a membrane protein and its F-D curve,* ***d****, simultaneous unfolding of two proteins and the balance of the forces involved.* ***e****, incomplete unfolding of a protein,* ***f****, unfolding from a cytoplasmic loop.* ***g****, prototypical F-D curves of a multiple unfolding/ unfolding from a loop.*

Finding the unfolding patterns of native membrane proteins.

The ideal methodology to find the recurrent patterns of unfolding in the data coming from native membranes is an unsupervised procedure able to filter out the stochastic events, and to identify clusters of dense patterns of any shape without setting their number *a priori*. For this purpose, we designed a pattern classification pipeline combining the density peak clustering[29] benchmarked for SMFS data {Ref. to Nina's thesis} with a final pattern recognition method used to determine the cluster population. This pipeline can detect statistically-dense patterns of unfolding within large datasets with a desktop computer (see Methods). This pipeline does not require to pre-set neither the number of clusters to be identified nor the dimension of the F-d curves and can be applied without prior knowledge of the sample composition.

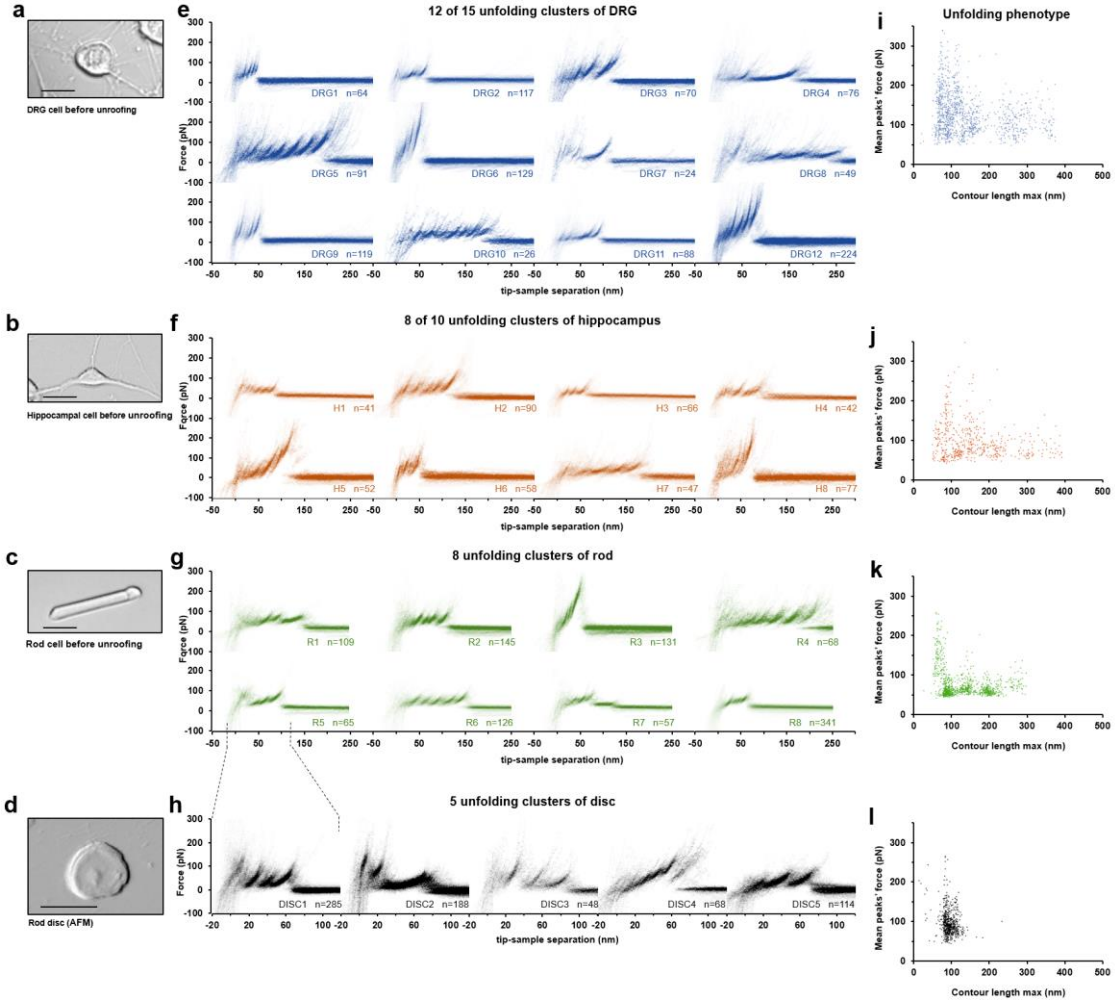

Figure 3 | Unfolding clusters in native cell membranes. *Bright field image of* ***a,*** *dorsal root ganglia neuron;* ***b*** *hippocampal neuron;* ***c*** *rot before unroofing (scale bar 15 µm).* ***d****, AFM error image of an isolated disc (scale bar 1 µm).* ***e, f, g, h****, superimposition of clustered F-D curves plotted as density maps.* ***i, j, k, l****, unfolding phenotype in the compact representation of all the clustered F-D curves in maximum contour length vs. average unfolding force space (DRG: n = 1255; hippocampus: n = 563; rod: n = 1039; disc: n = 703).*

We found 15, 10, 8 and 5 clusters (Fig.3 e-h) of F-d curves from DRG, hippocampal neurons, rod outer segments and rod discs membranes respectively. We identified four major classes of clusters based on their unfolding behavior. Short curves with increasing forces: DRG12, H5, H8 and R3 shows repeated peaks (ΔLc 10-20 nm, distance between consecutive peaks) of increasing force that reaches also 400 pN in force; these clusters resemble the

unfolding behavior of tandem globular proteins[4]. Long and periodic curves: R6, H7 or DRG10 display periodic peaks of ~100 pN and with a ΔLc of 30-40 nm whose unfolding patterns are similar to what seen in the LacY[20]. Short curves: the majority of the identified clusters like DRG1, H3, R8 and all clusters from the rod discs have curves less than 120 nm long and with constant or descending force peaks. The F-d curves of these clusters share various features with the opsin family proteins unfolded in purified conditions[8], e.g. a conserved unfolding peak at the beginning (at contour length < 20 nm) associated to the initiation of the denaturation of the protein. We found also "unconventional" clusters such as DRG7, DRG8 and R7: DRG8 exhibiting initial high forces and with variable peaks followed by more periodic low forces; while cluster R7 has a conserved flat plateau at the end of the curve of unknown origin. This last class displays features in common with the hypothesized unfolding from a loop or from multiple proteins.

The clustering allows also a representation of the output of the experiments in a single and compact display (Fig. 3 i-l) defining what we call the 'unfolding phenotype' of a specific cell membrane, which is peculiar of the cell type. We assigned to each F-D curve different parameters related to the geometrical features that are physically relevant (maximal contour length (Lc max), average unfolding force, average ΔLc, etc.). In this way, it is possible to phenotype the membrane protein landscape across cell types by visualizing the ensemble of all the clusters (see Supplementary Fig. 4).

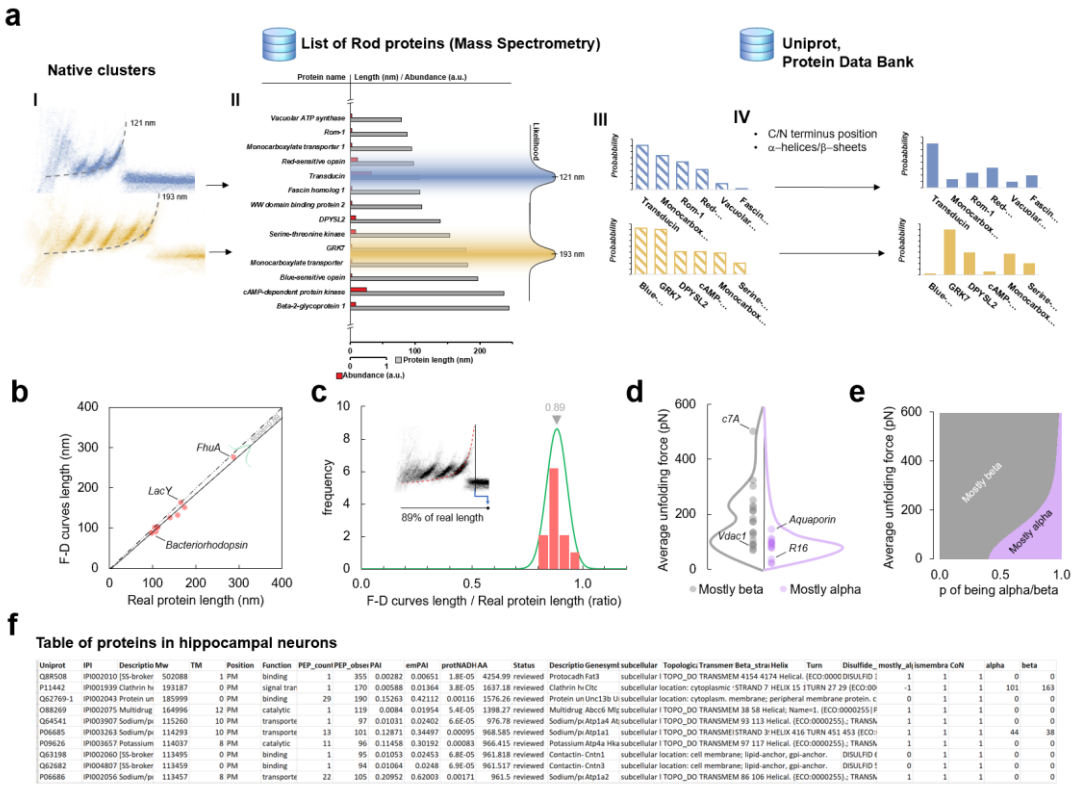

Uniprot	IPI	Descriptio	Mw	TM	Position	Function	PEP_coun	PEP_obse	PAI	emPAI	protNADH	AA	Status	Descriptio	Genesyml	subcellular	Topologic	Transmem	Beta_stra	Helix	Turn	Disulfide_	mostly_al	membra	CoN	alpha	beta
Q8R508	IPI002010	55-broker	502088	1	PM	binding	1	355	0.00282	0.00651	1.8E-05	4254.99	reviewed	Protocadh	Fat3	subcellular	TOPO_DO	TRANSMEM	4154	4174	Helical. (ECO:0000	DISULFID	1	1	1	0	0
P11442	IPI001939	Clathrin h	193187	0	PM	signal trar	1	170	0.00588	0.01364	3.8E-05	1637.18	reviewed	Clathrin h	Cltc	subcellular	location:	cytoplasmic	STRAND	7	HELIX	15	TURN	27	29 (ECO:00		-1	1	1	101	163
Q62769-1	IPI002043	Protein un	185999	0	PM	binding	29	190	0.15263	0.42112	0.00116	1576.26	reviewed	Protein un	Unc13b	subcellular	location:	cytoplasm.	membrane;	peripheral	membrane	protein. c		0	1	1	0	0
O88269	IPI002075	Multidrug	164996	12	PM	catalytic	1	119	0.0084	0.01954	5.4E-05	1398.27	reviewed	Multidrug	Abcc6	Mfg	subcellular	TOPO_DO	TRANSMEM	38	58	Helical; Name=1. (ECO:0000255	F	1	1	1	0	0
Q64541	IPI003907	Sodium/pi	115260	10	PM	transporte	1	97	0.01031	0.02402	6.6E-05	976.78	reviewed	Sodium/pi	Atp1a4	At	subcellular	TOPO_DO	TRANSMEM	93	113	Helical. (ECO:0000255);:	TRANSA	1	1	1	0	0
P06685	IPI003263	Sodium/pi	114293	10	PM	transporte	13	101	0.12871	0.34497	0.00095	968.585	reviewed	Sodium/pi	Atp1a1	subcellular	TOPO_DO	TRANSME	STRAND	3	HELIX	416	TURN	451	453 (ECO:		1	1	1	44	38
P09626	IPI003657	Potassium	114037	8	PM	catalytic	11	96	0.11458	0.30192	0.00083	966.415	reviewed	Potassium	Atp4a	Hka	subcellular	TOPO_DO	TRANSMEM	97	117	Helical. (ECO:0000255);:	TRANSA	1	1	1	0	0
Q63198	IPI002060	55-broker	113495	0	PM	binding	1	95	0.01053	0.02453	6.8E-05	961.818	reviewed	Contactin-	Cntn1	subcellular	location:	cell membrane;	lipid-anchor,	gpi-anchor.		DISULFID	0	1	1	0	0
Q62682	IPI004807	55-broker	113459	0	PM	binding	1	94	0.01064	0.0248	6.9E-05	961.517	reviewed	Contactin-	Cntn3	subcellular	location:	cell membrane;	lipid-anchor,	gpi-anchor.		DISULFID	0	1	1	0	0
P06686	IPI002056	Sodium/pi	113457	8	PM	transporte	22	105	0.20952	0.62003	0.00171	961.5	reviewed	Sodium/pi	Atp1a2	subcellular	TOPO_DO	TRANSMEM	86	106	Helical. (ECO:0000255);:	TRANSA	1	1	1	0	0

Figure 4 | Likelihoods and priors for the Bayesian identification. ***a****, workflow of the Bayesian steps: selection due to total length and abundance (mass spectrometry), refinement with structural and topological information (PDB and Uniprot).* ***b****, Comparison of the real length of the protein vs. the measured maximal contour length of the F-D curves in 14 SMFS experiments on membrane proteins.* ***c****, Likelihood function of the observed maximal length of the clusters obtained from* ***b****.* ***d****, Comparison of the force necessary to unfold beta sheets and alpha helices in 22 SMFS experiments.* ***e****, Likelihood function of the observed unfolding forces obtained from* ***d****.* ***f****, example of table entries resulting from the combination of mass spectrometry, Uniprot and PDB (Supplementary data).*

Bayesian identification of the unfolded patterns.

Having identified clusters of F-d curves from native membranes, the next question is: *which is the membrane protein whose unfolding corresponds to the identified clusters in Fig. 3?* In order to answer to this question, we developed a Bayesian method providing a limited list of candidate proteins on the basis of the information present in the data from Mass Spectrometry of the sample under investigation and other proteomic databases (Uniprot, PDB). The Bayesian identification (Fig. 4 a.) is based on two steps: firstly, the crossing of information between the cluster under investigation and the results of Mass Spectrometry analysis of the sample (hippocampal neurons, discs, etc.); secondly, a refinement of the preliminary candidates using additional information (structural and topological) present in the PDB and Uniprot databases.

The first step leverages the contour length of the last peak of the clusters (Lc_{max}; Fig. 4 a I). The SMFS-literature contains 14 examples of unfolded membrane proteins allowing a comparison between the Lc_{max} of the measured F-d curves and the real length of the same protein completely stretched (Fig.4 b). On the basis of these experiments, we extrapolated the first likelihood function of our Bayesian inference (Fig. 4 c) indicating that, on average, the Lc_{max} corresponds to 89% of the real length of the protein (R^2=0.98). By searching for proteins with this total length in the Mass Spectrometry data from the same samples[30–32] and by using their abundance (Fig. 4 a II) we obtained a first list in which we could assign a probability to each candidate.

The refinement to the first step (Fig. 4 a III) is obtained by combining the information on the molecular structure of the proteins (Fig. 4 a IV) extracted from the PDB and Uniprot. We created a table containing all the membrane proteins present in the Mass Spec data from the sample under investigation (hippocampal neurons, rods, etc.) reporting their abundance, number of amino acids, subcellular location, orientation of the N- and C-terminus, topology, fraction of α-helices and β-sheets, and presence of SS-bonds (Fig. 4 f, Supplementary Tables). The Bayesian approach assigns to the candidate proteins a probability also based on the location of the C- and N-terminus, and on the fact that unfolding β-sheets typically requires larger forces than in the case of α-helices (see Fig. 4 d). Indeed, from this force distribution we obtained the second likelihood function (Fig. 4 e) of our model.

There are proteins for which it is available a precise annotation of their topology (usually the most abundant proteins), in these cases we can be more precise assigning them an effective contour length (Lc_{max}) based on the real structure, and also identifying whether they are unfolded from the C- or the N-terminus.

Disulfide bonds (i.e. covalent bonds between non-adjacent cysteines) are known to have a high breaking force[33], till 1 nN. As a result, the mechanical unfolding of the protein with SS-bonds is usually not sufficient to break the bonds, generating a cluster with a shorter Lc_{max}[14,33]. The effective length of the protein with disulfide bonds is therefore reduced of the length enclosed between two consecutive bonded cysteines. The crossing with the Uniprot database that contains the information of the disulfide bonds allowed us to recalculate the effective total length of the proteins in our lists.

The framework of the lists is shown in Fig. 4 f, while the tables with all the information can be found in the Supplementary data of the article.

Following the Bayesian inference, we developed a method to estimate the probability of the candidate proteins for all the unfolding clusters found in hippocampal neurons, rod membranes and discs (Fig. 5 a-c). Starting from no information on the nature of these unfolding events, the software provides a list of known proteins which are the candidates of the molecules unfolded in the clusters of Fig.3. The software not only provides the candidates, but assign to each known protein a probability based on the Bayesian inference (Fig.4). Therefore, by simply crossing and exploiting the large information available in various databases, we identified a restricted number of molecular candidates for the identified unfolding clusters (Fig. 5). The more accurate assignations happen when a protein has a very high abundance (e.g. rhodopsin in discs and rods) or when there are few proteins of the same mass (length) of the identified protein.

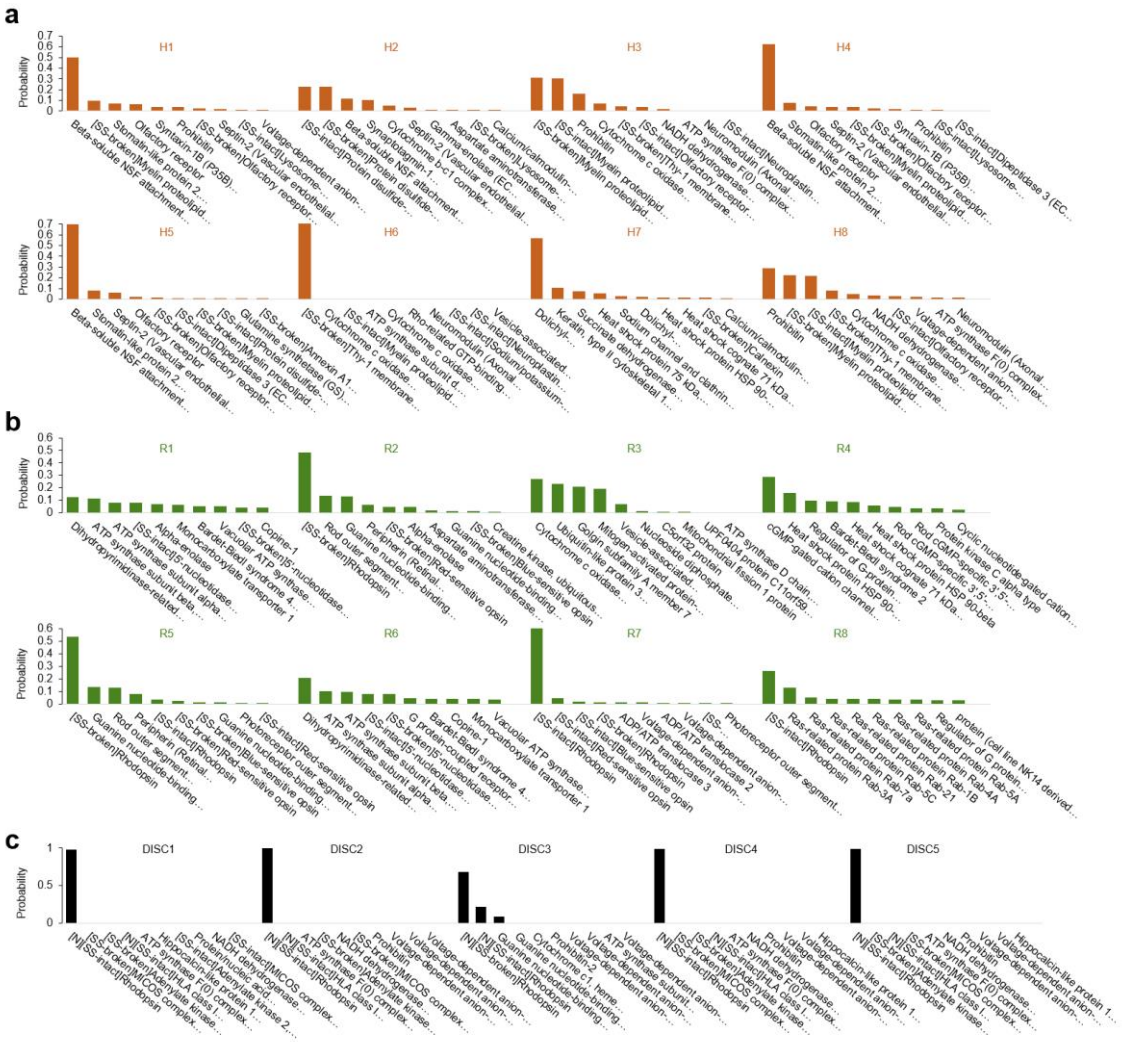

Figure 5 | Bayesian identification of the unfolding clusters. *Most probable candidates for the unfolding clusters found in* ***a****, hippocampal neurons;* ***b****, rods;* ***c****, rod discs.*

If the available data of Mass Spec from disks is complete—or almost complete—the proposed method will identify the proteins corresponding to the identified clusters with a probability close to 1.

To verify this analysis, we looked for an orthogonal validation of the proposed method, based on the results of two membrane proteins unfolded in native membranes, i.e. the cyclic nucleotide gated channel yet unfolded in semi-purified conditions[12] and hypothesized in previous experiments in the plasma membrane of rod outer segments[34], and the rhodopsin unfolded in discs[14,34]. The unfolding pattern from the C-terminus of the CNGA1 in semi-purified conditions[12] displays 5 major unfolding barriers starting from 100 nm and with a periodicity of ~30 nm, which are features similar to those observed in cluster R4. The CNGA1 is a highly abundant protein in the rod membrane, and indeed the Bayesian identification assign a probability of 29% for cluster R4 mostly due to a combination of the correct Lc window and its high abundance. We engineered a chimera of the CNG with N2B on the C-terminus that we overexpressed in the hybrid conditions explained in ref. [12]. These experiments generated an unfolding cluster with the same unfolding barrier shifted of ~ 85 nm, i.e. the length of the N2B, which confirmed also the fact that we were unfolding from the C- terminus (Supplementary Fig. 5 a-f).

With rhodopsin we reproduced the experiments performed in discs in ref. [14,34]. In discs we obtained 5 unfolding clusters of which DISC1 and DISC3 match the rhodopsin unfolding patterns of Tanuj et al. (see Supplementary Fig. 5 g-l), while DISC2, DISC4 and DISC5—

according to our identification—represent alternative unfolding pathways for rhodopsin. The identity of these clusters was demonstrated by enzymatic digestion with endoproteinase Glu-C that caused a truncation in the C-III loop of the rhodopsin molecule. The experiments performed after enzymatic digestion showed a 40-fold reduction of the F-D curves with a length comparable with rhodopsin, confirming the molecular origin of our unfolding clusters.

Discussion

The method here illustrated describes all the necessary steps to obtain F-d curves from biological membranes of cell types that grow in adhesion, and provides an automatic way to obtain clusters of F-d curves representing the unfolding of the membrane proteins present in the sample. We describe also a Bayesian approach able to provide a list of known proteins as candidates to be the unfolded protein. The Bayesian approach depends on the information present in Mass Spectrometry data and on the PDB and Uniprot databases. Therefore, the list of candidate proteins is expected to be refined as these databases will become richer and more complete, and the quality of Mass Spectrometry data will be improved. Let us discuss, now, the advantages and the weaknesses of the proposed method.

The possibility to perform SMFS experiments in natural samples obtained from native cells provides a clear breakthrough in the field of protein unfolding bypassing purification and reconstitution. In addition, the comparison of F-d curves obtained from the same protein in its natural environment and after purification will provide new insights on the role of the physico-chemical environment of the mechanical properties of proteins, a very important issue not yet properly investigated.

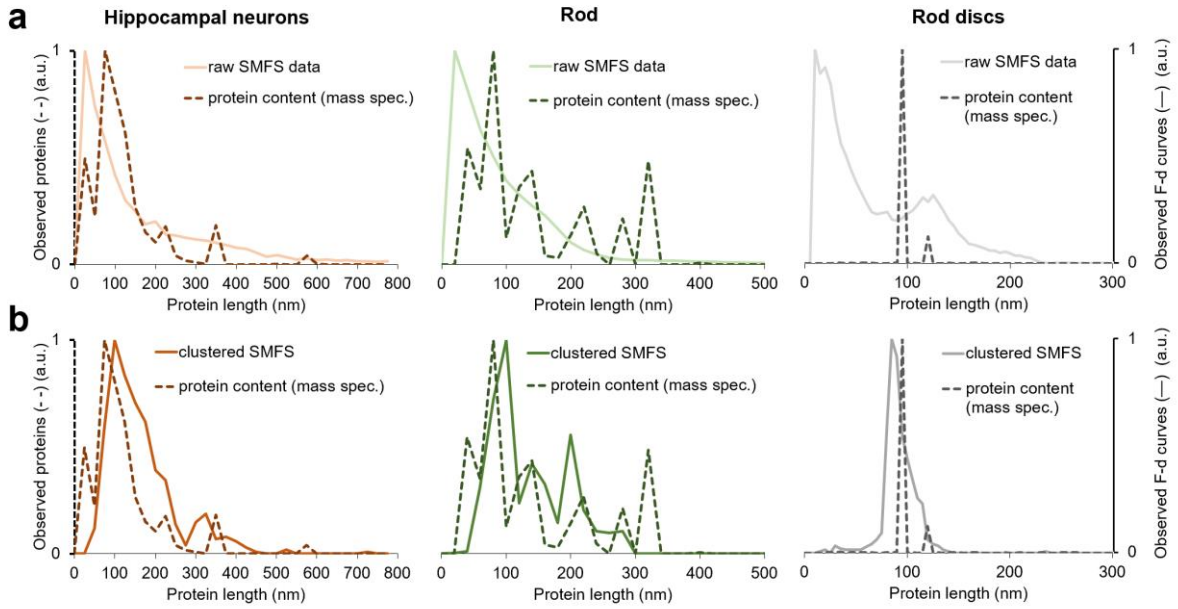

Figure 6 | Comparison of mass spectrometry protein detection vs. SMFS data. *Number of proteins / number of F-d curves observed for each length interval.* ***a****, normalized distribution of membrane proteins observed by mass spectrometry (broken lines) and distribution of the raw F-d curves.* ***b****, distribution of the clustered F-d curves of Fig. 3 approximate the distribution of the observed membrane proteins by mass spec. To the distributions of the F-d curves was applied the length correction of Fig. 4 c.*

One of the most relevant follow-ups of the method here proposed is the possibility to characterize molecules coming from a very limited amount of native material (membranes isolated from 1 to 10 cells). The unfolding phenotype is a univocal tool to characterize the sample under investigation (see Fig.3 and Supplementary Fig. 4) and this approach could be

extended to characterize membrane proteins in cells in healthy and sick conditions. Indeed, it is remarkable that the distribution of the detected proteins in our SMFS experiments (solid lines in Fig.6) is similar to that obtained in the Mass Spec experiments using millions of cells (broken lines). This is also an *ex post* confirmation of the goodness of using the mass spectrometry data in the Bayesian inference, and that our clustering method selects correctly the protein unfolding events.

In our experiments we collected a limited number of F-d curves—some hundreds of thousands—and by increasing their number by 10- or 100-fold, we expect to improve the total number of detected clusters—as those in Fig.3—possibly close to 100. As the total number of different membrane proteins from a native sample is on the order of hundreds, we expect to detect and characterize a significant fraction of the total membrane proteins present in the sample. Improvements of the proposed method, primarily by increasing its throughput, could potentially provide a new screening method with clinical applications: indeed, the characterization of the changes of the unfolding phenotype caused by a disease will provide a better understanding of the malfunction of membrane proteins. Moreover, the proposed method is able to explore the variety of proteins present in a sample with an accuracy almost similar to that obtained by Mass Spec, but using a much simpler apparatus.

The proposed method has some inherent limitations: indeed, the molecular identity of the unfolded proteins is guessed by a Bayesian estimator, which can be improved, but cannot be firmly established as in experiments with purified proteins. A possible way to obtain a better and more reliable identification of the proteins in the membrane is to couple the SMFS analysis of the native sample with a high-resolution AFM imaging of the same samples or, alternatively, we envision the use of the AFM cantilever as a mass sensor[35,36] of the unfolded proteins that could permit to exclude F-d curves where there is a mismatch between mass and length. However, in both cases, current technology is at least one order of magnitude away from the resolution needed.

The proposed method for clustering F-d curves is automatic but it is not fully unsupervised indeed Block 3 - in which we evaluate the quality of the F-d curve - assumes that a good F-d curve is piece-wise close to WLC. Block 5 of clustering method requires also a refinement which is done by the experimenter. The development of an unsupervised and fully automatic clustering method is under way.

Another major limitation of the proposed method—in its present form—is the possibility to merge in the same cluster the unfolding of proteins with a different molecular identity: indeed, from the Mass Spec data it is clear that different proteins have the same—or approximately the same—molecular weight and the total unfolded length Lc. this issue is rather significant for short proteins, I,e, those with values of Lc between 50 nm and 200 nm. In order to overcome this limitation, it will be desirable to couple SMFS with some chemical information on the unfolded protein. In our opinion, this will be a desirable achievement, which will make a substantial improvement to the method here proposed.

Acknowledgments

We thank dr. Kosaku Shinoda for support in the emPAI calculation. We thank Prof. Anna Menini who provided the mTMEM16A-GFP and mTMEM16A-GFP plasmids. We thank Prof. Guidalberto Manfioletti who provided the peGFP-N1 plasmid.

References

1. Al-Rekabi, Z. & Contera, S. Multifrequency AFM reveals lipid membrane mechanical properties and the effect of cholesterol in modulating viscoelasticity. *PNAS* **115**, 2658–2663 (2018).
2. Casuso, I. *et al.* Characterization of the motion of membrane proteins using high-speed atomic force microscopy. *Nature Nanotechnology* **7**, 525–529 (2012).
3. García-Sáez, A. J., Chiantia, S. & Schwille, P. Effect of Line Tension on the Lateral Organization of Lipid Membranes. *J. Biol. Chem.* **282**, 33537–33544 (2007).
4. Carrion-Vazquez, M. *et al.* Mechanical and chemical unfolding of a single protein: A comparison. *PNAS* **96**, 3694–3699 (1999).
5. Sarkar, A., Caamano, S. & Fernandez, J. M. The Elasticity of Individual Titin PEVK Exons Measured by Single Molecule Atomic Force Microscopy. *J. Biol. Chem.* **280**, 6261–6264 (2005).
6. Scheuring, S. & Sturgis, J. N. Chromatic Adaptation of Photosynthetic Membranes. *Science* **309**, 484–487 (2005).
7. Baumgartner, W. *et al.* Cadherin interaction probed by atomic force microscopy. *Proceedings of the National Academy of Sciences* **97**, 4005–4010 (2000).
8. Engel, A. & Gaub, H. E. Structure and Mechanics of Membrane Proteins. *Annual Review of Biochemistry* **77**, 127–148 (2008).
9. Otten, M. *et al.* From genes to protein mechanics on a chip. *Nat Meth* **11**, 1127–1130 (2014).
10. Thoma, J., Burmann, B. M., Hiller, S. & Müller, D. J. Impact of holdase chaperones Skp and SurA on the folding of β-barrel outer-membrane proteins. *Nat Struct Mol Biol* **22**, 795–802 (2015).
11. Hinczewski, M., Hyeon, C. & Thirumalai, D. Directly measuring single-molecule heterogeneity using force spectroscopy. *PNAS* **113**, E3852–E3861 (2016).
12. Maity, S. *et al.* Conformational rearrangements in the transmembrane domain of CNGA1 channels revealed by single-molecule force spectroscopy. *Nature Communications* **6**, 7093 (2015).
13. Thoma, J. *et al.* Protein-enriched outer membrane vesicles as a native platform for outer membrane protein studies. *Communications Biology* **1**, 23 (2018).
14. Tanuj Sapra, K. *et al.* Detecting Molecular Interactions that Stabilize Native Bovine Rhodopsin. *Journal of Molecular Biology* **358**, 255–269 (2006).
15. Kawamura, S., Colozo, A. T., Müller, D. J. & Park, P. S.-H. Conservation of Molecular Interactions Stabilizing Bovine and Mouse Rhodopsin. *Biochemistry* **49**, 10412–10420 (2010).
16. Galvanetto, N. Single-cell unroofing: probing topology and nanomechanics of native membranes. *Biochimica et Biophysica Acta (BBA) - Biomembranes* **1860**, 2532–2538 (2018).
17. Clarke, M., Schatten, G., Mazia, D. & Spudich, J. A. Visualization of actin fibers associated with the cell membrane in amoebae of Dictyostelium discoideum. *PNAS* **72**, 1758–1762 (1975).
18. Oesterhelt, F. *et al.* Unfolding Pathways of Individual Bacteriorhodopsins. *Science* **288**, 143–146 (2000).
19. Chu, C., Celik, E., Rico, F. & Moy, V. T. Elongated Membrane Tethers, Individually Anchored by High Affinity α4β1/VCAM-1 Complexes, Are the Quantal Units of Monocyte Arrests. *PLoS ONE* **8**, e64187 (2013).
20. Serdiuk, T. *et al.* YidC assists the stepwise and stochastic folding of membrane proteins. *Nat Chem Biol* **12**, 911–917 (2016).
21. Li, H. *et al.* Reverse engineering of the giant muscle protein titin. *Nature* **418**, 998–1002 (2002).
22. Lomize, M. A., Pogozheva, I. D., Joo, H., Mosberg, H. I. & Lomize, A. L. OPM database and PPM web server: resources for positioning of proteins in membranes. *Nucleic Acids Research* **40**, D370–D376 (2012).

23. Lomize, A. L., Pogozheva, I. D. & Mosberg, H. I. Anisotropic Solvent Model of the Lipid Bilayer. 2. Energetics of Insertion of Small Molecules, Peptides, and Proteins in Membranes. *Journal of Chemical Information and Modeling* **51**, 930–946 (2011).
24. Thoma, J., Bosshart, P., Pfreundschuh, M. & Müller, D. J. Out but Not In: The Large Transmembrane β-Barrel Protein FhuA Unfolds but Cannot Refold via β-Hairpins. *Structure* **20**, 2185–2190 (2012).
25. Sapra, K. T. *et al.* One β Hairpin after the Other: Exploring Mechanical Unfolding Pathways of the Transmembrane β-Barrel Protein OmpG. *Angewandte Chemie International Edition* **48**, 8306–8308 (2009).
26. Marsico, A., Labudde, D., Sapra, T., Muller, D. J. & Schroeder, M. A novel pattern recognition algorithm to classify membrane protein unfolding pathways with high-throughput single-molecule force spectroscopy. *Bioinformatics* **23**, e231–e236 (2007).
27. Spoerri, P. M. *et al.* Structural Properties of the Human Protease-Activated Receptor 1 Changing by a Strong Antagonist. *Structure* **26**, 829-838.e4 (2018).
28. Walder, R. *et al.* Rapid Characterization of a Mechanically Labile α-Helical Protein Enabled by Efficient Site-Specific Bioconjugation. *Journal of the American Chemical Society* **139**, 9867–9875 (2017).
29. Rodriguez, A. & Laio, A. Clustering by fast search and find of density peaks. *Science* **344**, 1492–1496 (2014).
30. Chen, P. *et al.* Proteomic analysis of rat hippocampal plasma membrane: characterization of potential neuronal-specific plasma membrane proteins. *Journal of Neurochemistry* **98**, 1126–1140 (2006).
31. Kwok, M. C. M., Holopainen, J. M., Molday, L. L., Foster, L. J. & Molday, R. S. Proteomics of Photoreceptor Outer Segments Identifies a Subset of SNARE and Rab Proteins Implicated in Membrane Vesicle Trafficking and Fusion. *Molecular & Cellular Proteomics* **7**, 1053–1066 (2008).
32. Panfoli, I. *et al.* Proteomic Analysis of the Retinal Rod Outer Segment Disks. *Journal of Proteome Research* **7**, 2654–2669 (2008).
33. Ainavarapu, S. R. K. *et al.* Contour Length and Refolding Rate of a Small Protein Controlled by Engineered Disulfide Bonds. *Biophysical Journal* **92**, 225–233 (2007).
34. Maity, S., Ilieva, N., Laio, A., Torre, V. & Mazzolini, M. New views on phototransduction from atomic force microscopy and single molecule force spectroscopy on native rods. *Scientific Reports* **7**, (2017).
35. Boisen, A. & Thundat, T. Design & fabrication of cantilever array biosensors. *Materials Today* **12**, 32–38 (2009).
36. Martínez-Martín, D. *et al.* Inertial picobalance reveals fast mass fluctuations in mammalian cells. *Nature* **550**, 500–505 (2017).
37. Mazzolini, M. *et al.* The phototransduction machinery in the rod outer segment has a strong efficacy gradient. *PNAS* **112**, E2715–E2724 (2015).
38. Butt, H.-J., Jaschke, M. & Ducker, W. Measuring surface forces in aqueous electrolyte solution with the atomic force microscope. *Bioelectrochemistry and Bioenergetics* **38**, 191–201 (1995).
39. Thoma, J. *et al.* Maltoporin LamB Unfolds β Hairpins along Mechanical Stress-Dependent Unfolding Pathways. *Structure* **25**, 1139-1144.e2 (2017).
40. Müller, D. J. *et al.* Stability of Bacteriorhodopsin α-Helices and Loops Analyzed by Single-Molecule Force Spectroscopy. *Biophysical Journal* **83**, 3578–3588 (2002).

Methods

All experimental procedures were in accordance with the guidelines of the Italian Animal Welfare Act, and their use was approved by the SISSA Ethics Committee board and the National Ministry of Health (Permit Number: 630-III/14) in accordance with the European Union guidelines for animal care (d.1.116/92; 86/609/C.E.).

Cell preparation and culture.

Hippocampal and DRG neurons.

Hippocampal and DRG neurons were obtained from Wistar rats (P2-P3) as described in ref. [16]. In short, the animals were anesthetized with CO_2 and sacrificed by decapitation. The dissociated cells were plated at a concentration of 4×10^4 cells/ml onto glass round coverslips (170 µm in thickness) coated with 0.5 mg/ml poly-D-lysine (Sigma-Aldrich, St. Louis, MO, USA) for 1 h at 37°C and washed 3 times in deionized water. It is fundamental to obtain an optimal adhesion of the cells to prevent detachment in the next step (isolation of the cell membrane). The medium used for hippocampal neurons is in Minimum Essential Medium (MEM) with GlutaMAX supplemented with 10% Fetal Bovine Serum (FBS, all from Invitrogen, Life Technologies, Gaithersburg, MD, USA), 0.6% D-glucose, 15 mM Hepes, 0.1 mg/ml apo-transferrin, 30 µg/ml insulin, 0.1 µg/ml D-biotin, 1 µM vitamin B12 (all from Sigma-Aldrich), and 2.5 µg/ml gentamycin (Invitrogen). The medium used for DRG neurons is Neurobasal medium (Gibco, Invitrogen, Milan, Italy) supplemented with 10% Fetal Bovine Serum (FBS, from Invitrogen, Life Technologies, Gaithersburg, MD, USA).

Rods.

Rod cells were obtained from adult male Xenopus laevis as described in ref. [37]. Under infrared illumination, the eyes of dark-adapted frogs after anesthesia with MS-222 were surgically extracted. Eyes were preserved in the Ringer solution (110 NaCl, 2.5 KCl, 1 CaCl2, 1.6 MgCl2, 3 Hepes-NaOH, 0.01 EDTA, and 10 glucose in mM; pH 7.8 buffered with NaOH), and hemisected under a dissecting microscope. The extracted retina was maintained in the Ringer solution.

NG108-15.

Mouse neuroblastoma NG108-15 cells were obtained from Sigma-Aldrich. The cells were grown in Dulbecco's Modified Eagle Medium (DMEM, ThermoFisher) plus 10% Fetal bovine serum (FBS, Gibco), 100 U/ml Penicillin and 100 U/ml Streptomycin. The cells were cultured into a humidified incubator (5% CO2, 37 °C).

Cell transfection.

NG108-15 cells were transiently transfected with 300 ng of each cDNA expression plasmids by using Lipofectamine 2000 Transfection Reagent (ThermoFisher) according to its handbook. Briefly, mTMEM16A-GFP plasmids (with GFP at their C-terminal) expression vector peGFP-N1 plasmid and the Lipo2000 were diluted into Opti-MEM Reduced Serum Medium (Gibco), respectively. 5 mins later, we added the diluted DNA to the diluted Lipo2000 to make the plasmid DNA-lipid complexes. After incubating 30 min, we plated the cells on the 12 mm round coverslips coated with 1x Poly-L-Ornithine (Sigma-Aldrich) in 12 well plate, and in the meanwhile, we added DNA-lipid complexes to the cells. We performed membrane isolation about 48 hours after transfection.

Isolation of cell membranes.

Single-cell unroofing (for cell types that grow in adhesion).

The apical membrane of Hippocampal neurons, DRGs and NG108-15 were isolated with an optimized version of the unroofing method[16]. Briefly, additional empty glass coverslips (24 mm in diameter, 170 µm in thickness) were plasma cleaned for 15 seconds and broken in 4 quarters (with the use of the hands) in order to obtain optically sharp edges, as described in [16]. The coverslip quarters were immersed in 0.5 mg/ml poly-D-lysine for 30 minutes, and then they were immersed in deionized water for 10 seconds before use. A petri dish was filled with Ringer solution (2 ml), where the glass quarter was placed tilted of 7-15 degrees in the middle of it, supported by a 10 x 10 x 1 mm glass slice and Vaseline. The cover of the petri dish was then fixed on the stage of the AFM-inverted microscope setup (JPK Nanowizard 3 on an Olympus IX71).

The cell culture was then mounted on a 3D printed coverslip holder connected to the head stage of the AFM. The AFM head was put on top of the stage in measurement position. The cell culture was immersed into the solution and a target cell was identified and aligned with the underlying corner of the glass quarter. The cell culture was moved towards the corner of the underlying glass with the motors of the AFM until the target cell was squeezed and it doubled its area. At this point the cell is kept squeezed for 3 minutes, then a loaded spring under the AFM is released to abruptly separate the corner from the cell culture, and break the target cell membrane. The glass quarter with the isolated cell membrane was laid down and fixed on the petri dish. The medium was replaced with Ringer's solution without exposing the cell membrane to the air.

Membrane isolation of non-adherent cells.

Cells that do nott grow in adhesion usually do not establish a tight binding with the substrate on top of which they are deposited. For these cells (e.g. rod cells), instead of unroofing, it is more reliable to break the cells with a lateral flux of medium[17].

Isolated and intact rods were obtained by mechanical dissociation of the Xenopus retina in an absorption buffer (150 mM KCl, 25 mM $MgCl_2$, and 10 mM Trizma base; pH 7.5); they were then deposited on cleaved mica as described in ref.[34]. Incubated rods were maintained for 30–45 minutes over the mica in order to be adsorbed by its negatively charged surface. In the meanwhile, the position of the rods in the field of view of the microscope was annotated. The absorption buffer was substituted by a solution containing (in mM): 150 KCl, 10 Tris-HCl, (pH 7.5) and then a lateral flux of medium was applied to the rods until all the cell bodies were removed.

Isolation of rod discs.

Purification techniques with multiple centrifugations are usually required to isolate membrane-only organelles like rod discs or outer membrane vesicles[13]. Rod discs were obtained starting from the extracted retina as described in ref. [34]. Briefly, discs were separated with two series of centrifugations of the sample overlaid on a 15-40% continuous gradient of OptiPrep (Nycomed, Oslo, Norway). 40 µl of the sample were diluted with 40 µl of absorption buffer, and incubated on freshly cleaved mica for 40 minutes. After 40 minutes, the incubation medium was removed and substituted with the solution used in the AFM experiments (150mM KCl, 10mM Tris-HCl, pH 7.5).

AFM imaging and Single-Molecule Force Spectroscopy (SMFS).

AFM experiments was performed using an automated AFM (JPK Nanowizard 3) with 50 µm long cantilevers (AppNano HYDRA2R-NGG, nominal spring constant = 0.84 N/m). We calibrated the AFM cantilevers in the experimental medium before each experiment using the equipartition theorem[38]. The AFM experiments of Hippocampal neurons and DRGs were performed with Ringer's solution (NaCl 145 mM, KCl 3 mM, CaCl2 1.5 mM, MgCl2 1 mM, HEPES 10 mM, pH 7.4); Rod membrane and discs experiments were performed with 150mM KCl, 10mM Tris-HCl, pH 7.5. All experiments were performed at 24 Celsius.

AFM imaging.

The position of the cells before unroofing was annotated in the monitor of the computer in order to start the AFM imaging where the cells was in contact with the substrate (cell membrane is not visible in bright-field). The membrane obtained with single-cell unroofing (hippocampal neurons and DRG) can easily be found in proximity of the glass corner (~80% success rate). In the case of the rod membrane (non-adherent cells), usually different positions need to be scanned before finding a patch of membrane. Rod discs can be identified only via AFM imaging. We performed imaging both in contact mode (setpoint ~0.4 nN) and intermittent-contact mode (lowest possible), but the intermittent-contact mode if preferable because it does not damage the border of the patches of membrane.

AFM-based SMFS (protein unfolding)

we performed automated SMFS on top of the imaged membranes by setting grid positions for the approaching and retraction cycles of the cantilever. All experiments were performed with a retraction speed of 500 nm/s. The membrane proteins present in the sample were attached non-specifically to the cantilever tip by applying a constant force of ~1 nN for 1 second between the AFM tip and the cytoplasmic side of the membrane. This method proved to work with different membrane proteins[14,24,39], and to allow a higher throughput compared to methods that involve a specific attachment between the tip and the protein[18,40–42]..

Automatic classification of SMFS data.

The selection of the F-d curves that represent the unfolding of membrane proteins is usually based on the search for a specific pattern of unfolding in the SMFS data, after a filtering based on the length of the protein under investigation[26,27]. In the case of a native preparation (like ours) that contains a mixture of unknown proteins a) the filtering based on the distance cannot be applied and b) the number of specific patterns to be found is unknown. In order to find recurrent patterns of unfolding in a SMFS dataset we developed an algorithm that consists of five major blocks (Supplementary Fig. 3 a). In the first block, the parts of the F-d curves not related to the unfolding process are removed, and a coarse filtering aimed at the detection of spurious traces is performed. In the second block, a quality score based on the consistency of the experimental data with the worm-like chain (WLC) model is computed and assigned to each trace. This score is used to select physically meaningful traces for further analysis. In the third block, distances between pairs of traces are computed to assess their similarity. The distances are used in the fourth block for density peak clustering. The fifth and final block consists in the refinement and possibly in the merging of some of these clusters. In what follows we provide a detailed overview of each block.

Block 1: filtering.

The standard F-d curve preprocessing was applied to all the data within 'Fodis'[43]. The zero of the force of the curve was determined averaging the non-contact part (baseline after the final peak) and subtracted to all the points of the curve. The piezo position was transformed in tip-sample-separation considering the contribution of the bending of the tip to the extension of the polymer. Given that the F-d curves are subject to noise (due to thermal fluctuations, coming from the instrument, etc.), we smooth the original signals through interpolation on a grid with width δ_{interp}= 1 nm.

A curve is discarded if it does not contain a:

- detectable contact point (i.e. a transition from negative forces to positive forces in respect to the baseline set at zero force);
- if the points occupy force ranges over 5000 pN;

Some of the F-d curves show deviations from the horizontal zero-force line in the non-contact part (wavy final part due to imperfect detachment of the polymer or other noise from the environment). We detect and discard these traces by computing the standard deviation of the tails from the zero-force line. If it exceeds two times σ_{NOISE} (average standard deviation of the baseline of the batch of curves) the trace is discarded.

Block 2: Quality score.

The quality score is used for refine selection of traces with high information content vs. noisy traces. It is based on the description provided by the worm-like chain (WLC) model, which is the standard model in the analysis of SMFS data[33]. The WLC model implies the equation:

$$F(x) = \frac{k_B T}{l_p}\left(\frac{1}{4}\left(1 - \frac{x}{L_c}\right)^{-2} + \frac{x}{L_c} + \frac{1}{4}\right) \quad (1)$$

where F is force, x is extension, k_B is Boltzmann's constant, T is temperature, l_p is persistence length and L_c is contour length. Each unfolding curve in the trace is fitted with the WLC equation and a L_c value, corresponding to the length of the unfolded protein domain is obtained. The L_c values are computed by solving equation (1) for each x and F. An appropriate value for the persistence length l_p for membrane proteins is 0.4 nm as reported in ref. [33]. The WLC model is applicable in the force range 30-500 pN[44].

Once we compute the L_c values, we can build a L_c histogram. Normally, the L_c histogram describing a successful unfolding experiment is characterized by the presence of a few maxima separated by deep minima. We implement these features in the definition of our quality score to distinguish meaningful F-d curves.

An important parameter is the bin width of the L_c histogram. If the bin width is too small the histogram is noisy; if the bin width is too large, peaks corresponding to the unfolding of different domains might be merged. We use bin width 8 nm which is an efficient value for evaluating the goodness of a curve and it allows to consider also curves that deviate from the WLC model (l_p =0.4 nm) but that contain information. Furthermore, the choice of such large bin width is based on visual inspection of the histograms of proteins with known structure. Once the L_c histogram is built, we detect all maxima and minima. A maximum is meaningful if it is generated by more than 5 points and it includes more than 1 % of the force measures of a trace.

For each maximum in the L_c histogram, we compute a score W quantifying the consistency of the peak with the WLC model. A high-quality peak is clearly separated from other peaks of the histogram, therefore it should be surrounded by two minima. We define $f_{left} = \frac{P_{left}}{P_{max}}, f_{right} = \frac{P_{right}}{P_{max}}$ where P_{max} , P_{left} and P_{right} are the probability densities of the maximum, of the left and the right minima. Ideally, $f \sim \frac{1}{2}\left(f_{left} + f_{right}\right)$ should go to 0. We define the peak score as $W = exp(-2f^2)$. According to this definition, if $P_{left} = 1, P_{right} = 2$ and P_{max}=16, W=0.98. Whilst if $P_{left} = 13, P_{right} = 14$, the peak doesn't fit well with the WLC model and W=0.24.

Once a score is computed for each relevant peak in the L_c histogram, that score is assigned to all points in the corresponding trace. This is accomplished in two steps: first, the peak score is assigned to all points in the histogram belonging to that peak. Second, to all points with force values below 30 pN, for which an L_c values cannot be computed due to the model's limitations. To these points, we assign the score of the first successive point with force larger than 30 pN. This criterion applies only to points within 75 nm from the last point assigned to the peak. The peak width value is selected by visual inspection of traces, evaluating the maximum width of their force peaks.

The quality score of a trace, S_w, is the sum of the scores for all points in the trace. The higher the global score, the higher the trace quality. We use the ratio between the quality score and the trace length to select high quality traces. If this ratio is below 0.5, we discard the trace. We assume that if more than half of the trace is inconsistent with the WLC model, it is a low-quality trace and as such we exclude it from the analysis. While if more than half of the trace is in good agreement with the WLC model, it is possibly a meaningful trace.

We point out that the goal of blocks 1–4 is only to find dense recurrent patterns in the SMFS data: in block 5 we reevaluate the F-d curves to form the selections shown in Fig. 3 of the main text.

Block 3: Computing distances

In block 3 we quantify the similarity between the traces in order to find the recurrent pattern of unfolding within the data. To accomplish this goal, we use a modified version of the distance introduced by Marsico et al.[26]. This distance is defined using the dynamic programming alignment score computed for a pair of traces. For two traces, *a* and *b*, the distance d_{ab} is simply:

$$d_{ab} = 1 - \frac{S_D(N_a, N_b)}{N_{max}} \tag{2}$$

where $S_D(N_a, N_b)$ is the global alignment score, N_a is the length of trace *a*, N_b is the length of trace *b*, and N_{max} is the maximum length between the two. We have modified the match/mismatch scoring function used by Marsico et al as follows:

$$M(i,j) = \begin{cases} 1 - \dfrac{|F_a(i) - F_b(j)|}{F_{scoring}} & if\ |F_a(i) - F_b(j)| < F_{scoring} \\ -\dfrac{|F_a(i) - F_b(j)|}{F_{scoring}} & otherwise \end{cases} \tag{3}$$

where $F_a(i)$ and $F_b(j)$ are the forces in points *i* and *j* in traces *a* and *b*, and $F_{scoring} = 4\sigma_{NOISE}$. In the work done by Marsico et al, $F_{scoring}$ is replaced by ΔF_{max}, which is the average of the maximum force values in the two traces. When two widely different traces have high ΔF_{max} their distance will be lower with respect to two traces with low ΔF_{max} but overall higher level of similarity. Namely, the distance magnitude depends on the ΔF_{max} value and traces with high ΔF_{max} have by definition lower distance values. It is important to note that this problem did not occur in Marsico's work since the ΔF_{max} values were uniformly distributed for all traces.

In order to gain computational efficiency, the distance is computed only for traces which differ by no more than 2 peaks in the L_c histograms or by no more than 20 % in their trace length difference.

Block 4: Density peak clustering.

The density peak clustering (DPC) algorithm[29] is used for clustering. This choice is appropriate given that a fraction of traces in the analyzed datasets correspond to statistically isolated events and DPC automatically excludes the outliers. DPC can be summarized in the following steps:

1. We compute the density of data points in the neighborhood of each point using the *k*-nearest neighbor (*k*-NN) density estimator[45]. The density is the ratio between *k* and the volume occupied by the *k* nearest neighbors:

$$\tilde{\rho}_i = \frac{k}{\omega_d r_{k,i}^d} \tag{4}$$

where *d* is the intrinsic dimension (ID) of the dataset[46], ω_d is the volume of the *d*-sphere with unitary radius and $r_{k,i}$ is the distance of point *i* from its *k*-th nearest neighbor. In DPC it is the density rank which is relevant for the final cluster assignation. Therefore, without loss of generality, we compute the density using the following equation:

$$\rho_i = -\log r_{k,i} \tag{5}$$

$\tilde{\rho}_i$ and ρ_i are related by a simple monotonic transformation and thus, have the same rank. By using equation (4) we don't have to compute the intrinsic dimension of the dataset. In order to assign bigger weight to high quality traces, we multiply ρ_i by the score-length ratio of trace *i*.

2. Next, we find the minimum distance between point *i* and any other point with higher density, denoted as δ_i:

$$\delta_i = \min_{j:\rho_j > \rho_i} d_{ij} \tag{6}$$

where d_{ij} is the distance between points *i* and *j*. δ_i is used to identify the local density maxima.

3. We identify the cluster centers as density peaks, e.g. points with high values of both ρ_i and δ_i. For each point we compute the quantity $\gamma_i = \rho_i \delta_i$. Points with high values of γ_i are good cluster center candidates. We sort all points by the value of γ_i in descending order. The first point is a cluster center. The second point is a cluster center unless its distance from the first point is smaller than $r_{cut} = 0.3$ (which represents the distance below which on average two traces are considered as the same pattern). Regarding the third point, it is a cluster center if it is at a distance smaller than r_{cut} from the preceding two points. Following the same logic, all the points are assessed and all cluster centers are identified.
4. All points that are not cluster centers are assigned to the same cluster of the nearest point with higher density.

Block 5: Refinement and merging

The previous blocks, from 1 to 4, were optimized for finding the centers of dense patterns of unfolding in the SMFS data, but not for finding the borders of the clusters. To solve this issue, i.e. finding the F-d curves that are similar to each pattern of unfolding, we used the conventional definition of similarity (degree of superposition of F-d curves in the Force/tip-sample-separation plane) automated in the Fodis software in the tool 'fingerprint_roi'[43].

In brief, we superimposed each cluster center with its two closest neighbors creating the effective 'area of similarity' (AoS) for each cluster. The AoS is defined as the area generated by all the points of the three curves above 30 pN and before the last peak (see Supplementary Fig. 3 b), each point forming a square of 5 nm x 5 pN. Then, the SMFS curves are preliminary filtered based on their length with their final peak falling between 0.7 x *L* and 1.3 x *L* (with *L* length of the cluster center). Each of the remaining F-d curves is compared with the AoS, and the number of its points that fall within the AoS is annotated: this number constitutes the similarity score. As depicted in Supplementary Fig. 3 c, the plot of the scores in descending order interestingly forms a line with two different slopes. The change of the slope empirically defines a threshold that reflects the limit of similarity for each cluster. If two clusters share more than 40% of the traces above the threshold, they are considered the same cluster, thus merged (all the merges are reported in Supplementary Fig. 3 d).

Bayesian identification of F-D curves.

Bayesian inference is widely used in modern science[47,48] because it allows to univocally determine the level of uncertainty of a hypothesis[49]. We used the same framework to determine the molecular identity of the unfolding clusters. In the most general terms, we observed the unfolding cluster C_X, and we want to find the probability that the unfolding of a certain protein $Prot_A$ corresponds to the unfolding cluster C_X, i.e. we want to find the posterior probability $P(Prot_A|C_X)$. In the form of the Bayes theorem:

$$P(Prot_A|C_X) = \frac{P(C_X|Prot_A)P(Prot_A)}{P(C_X)} \quad (7)$$

where $P(Prot_A)$ is the prior, i.e. the probability of $Prot_A$ to be in the sample; $P(C_X|Prot_A)$ is the likelihood, i.e. the probability to find a cluster with the features of C_X coming from the unfolding of $Prot_A$; and $P(C_X)$ is the normalizing factor. In the case of a classical experiment with a single purified protein, $P(Prot_A|C_X)$ is assumed to be equal to 1, but this is not the case for a native environment where there are $Prot_B$, $Prot_C$, etc.

The observables of an unfolding cluster for which we determined the likelihood functions are the contour length of the last detectable peak $Lc_{max,Cx}$ (~ length of the F-d curve), and the average unfolding force of the detected peaks $\bar{F}_{Cx}$, but the method is modular therefore it could incorporate also other observables. The equation (7) becomes:

$$P\left(Prot_A \middle| Lc_{max,Cx}, \bar{F}_{Cx}\right) = \frac{P\left(Lc_{max,Cx}|Lc_{Prot_A}\right) P\left(\bar{F}_{Cx}|\bar{F}_{Prot_A}\right) P(Prot_A)}{N} \quad (8)$$

where $N = \sum_i (P\left(Lc_{max,Cx}|Lc_{Prot_i}\right) P\left(\bar{F}_{Cx}|\bar{F}_{Prot_i}\right) P(Prot_i))$ is the normalizing factor that takes into consideration all the proteins $Prot_i$ present in the sample. In the next paragraph we will describe the determination of the numerator of equation (8).

Determination of prior probability $P(Prot_A)$

The most crucial part of the method is the determination of the list of proteins present in the sample, together with all their properties (length, abundance, secondary structure, topology, etc.). To do so we combined the Mass Spectrometry results of the cells under investigation[30–32] with other structural and topological information available in Uniprot and PDB. The crossing of the databases is done thanks to the unique Uniprot identifier. The complete list of proteins of Hippocampal neurons, Rod outer segments and Rod discs with the information necessary for the Bayesian inference are shown in the Supplementary Data of the article. In case the data of the species of interest are not available, cross species proteomic analysis demonstrated that the majority of proteins are conserved in terms of relative abundance[50,51].

$P(Prot_A)$ is the probability of finding $Prot_A$ and not $Prot_B$, $Prot_C$, etc., which corresponds to the normalized relative abundance of $Prot_A$ in the sample—a parameter that is usually calculated in mass spectrometry analysis. Indeed, *in silico* calculation of abundances gives rather trustworthy values:

1. the most accurate option is the emPAI[52];
2. if the emPAI is not available, the second best option is the spectra counting for each peptide (PSM)[53];
3. if the PSM is not available, the sequence coverage can be used as loose estimation[54].

We used the emPAI for hippocampal neurons and rods; for the discs, the emPAI does not give accurate values because of the extreme concentration of Rhodopsin, therefore we used the abundances obtained with other quantitative methods[55].

We demonstrated in Supplementary Fig 1 that the isolated paches of membrane contain the membrane proteins of the original cells but not the cytoplasmic proteins, therefore we created an additional binary variable $ismembrane$ for each protein equal to 0 if the protein is not a membrane protein, 1 otherwise. This information is extracted from the annotation in the Uniprot database. The final prior probability is:

$$P(Prot_A) = abundance_A \times ismembrane_A \quad (9)$$

Determination of the Likelihood function $P\left(Lc_{max,Cx}|Lc_{Prot_A}\right)$

The F-d curves encode a reliable structural information, that is the total length of the unfolded protein[18]. We revised 14 published unfolding clusters of membrane proteins[12,18,20,24,25,39,41,42,56–60] that allowed us to create the likelihood function for the observable $Lc_{max,Cx}$ as shown in Fig. 4 b–c. This likelihood is a Gaussian centered at $0.89Lc_{Prot_A}$ with a standard deviation of $0.05Lc_{Prot_A}$.

Determination of the Likelihood function $P\left(\bar{F}_{Cx}|\bar{F}_{Prot_A}\right)$

The force necessary to unfold a protein domain depends on the stability of the domain itself. α-helices and β-sheets are unfolded at different force levels as shown in Fig. 4 d. We revised the unfolding forces of 32 proteins and we used as $P\left(\bar{F}_{Cx}|\bar{F}_{Prot_A}\right)$ the smoothed trend line of the distribution (Fig. 4 e of the main text).

All the data and the Matlab functions for the Bayesian inference are present in the Supplementary Data of the article.

References

41. Cisneros, D. A., Oesterhelt, D. & Müller, D. J. Probing Origins of Molecular Interactions Stabilizing the Membrane Proteins Halorhodopsin and Bacteriorhodopsin. *Structure* **13**, 235–242 (2005).
42. Kedrov, A., Ziegler, C., Janovjak, H., Kühlbrandt, W. & Müller, D. J. Controlled Unfolding and Refolding of a Single Sodium-proton Antiporter using Atomic Force Microscopy. *Journal of Molecular Biology* **340**, 1143–1152 (2004).
43. Galvanetto, N. *Fodis: a Software for Single Molecule Force Spectroscopy*. (2018).
44. Petrosyan, R. Improved approximations for some polymer extension models. *Rheol Acta* 1–6 (2016). doi:10.1007/s00397-016-0977-9
45. Altman, N. S. An Introduction to Kernel and Nearest-Neighbor Nonparametric Regression. *The American Statistician* **46**, 175–185 (1992).
46. Facco, E., d'Errico, M., Rodriguez, A. & Laio, A. Estimating the intrinsic dimension of datasets by a minimal neighborhood information. *Scientific Reports* **7**, (2017).
47. Wang, Q. *et al.* A Bayesian framework that integrates multi-omics data and gene networks predicts risk genes from schizophrenia GWAS data. *Nature Neuroscience* **22**, 691–699 (2019).
48. Heenan, P. R. & Perkins, T. T. FEATHER: Automated Analysis of Force Spectroscopy Unbinding and Unfolding Data via a Bayesian Algorithm. *Biophysical Journal* **115**, 757–762 (2018).
49. Jaynes, E. T. *Bayesian Methods: General Background*. (1986).
50. Bayram, H. L. *et al.* Cross-species proteomics in analysis of mammalian sperm proteins. *Journal of Proteomics* **135**, 38–50 (2016).
51. Wright, J. C., Beynon, R. J. & Hubbard, S. J. Cross Species Proteomics. in *Proteome Bioinformatics* (eds. Hubbard, S. J. & Jones, A. R.) **604**, 123–135 (Humana Press, 2010).
52. Ishihama, Y. *et al.* Exponentially Modified Protein Abundance Index (emPAI) for Estimation of Absolute Protein Amount in Proteomics by the Number of Sequenced Peptides per Protein. *Mol Cell Proteomics* **4**, 1265–1272 (2005).
53. Liu, H., Sadygov, R. G. & Yates, J. R. A Model for Random Sampling and Estimation of Relative Protein Abundance in Shotgun Proteomics. *Anal. Chem.* **76**, 4193–4201 (2004).
54. Florens, L. *et al.* A proteomic view of the *Plasmodium falciparum* life cycle. *Nature* **419**, 520 (2002).
55. Milo, R. & Phillips, R. *Cell biology by the numbers*. (2016).
56. Kawamura, S. *et al.* Kinetic, Energetic, and Mechanical Differences between Dark-State Rhodopsin and Opsin. *Structure* **21**, 426–437 (2013).
57. Möller, C. *et al.* Determining molecular forces that stabilize human aquaporin-1. *Journal of Structural Biology* **142**, 369–378 (2003).
58. Ge, L. *et al.* Molecular Plasticity of the Human Voltage-Dependent Anion Channel Embedded Into a Membrane. *Structure* **24**, 585–594 (2016).
59. Bosshart, P. D. *et al.* The Transmembrane Protein KpOmpA Anchoring the Outer Membrane of Klebsiella pneumoniae Unfolds and Refolds in Response to Tensile Load. *Structure* **20**, 121–127 (2012).
60. Klyszejko, A. L. *et al.* Folding and Assembly of Proteorhodopsin. *Journal of Molecular Biology* **376**, 35–41 (2008).

Supplementary Figures

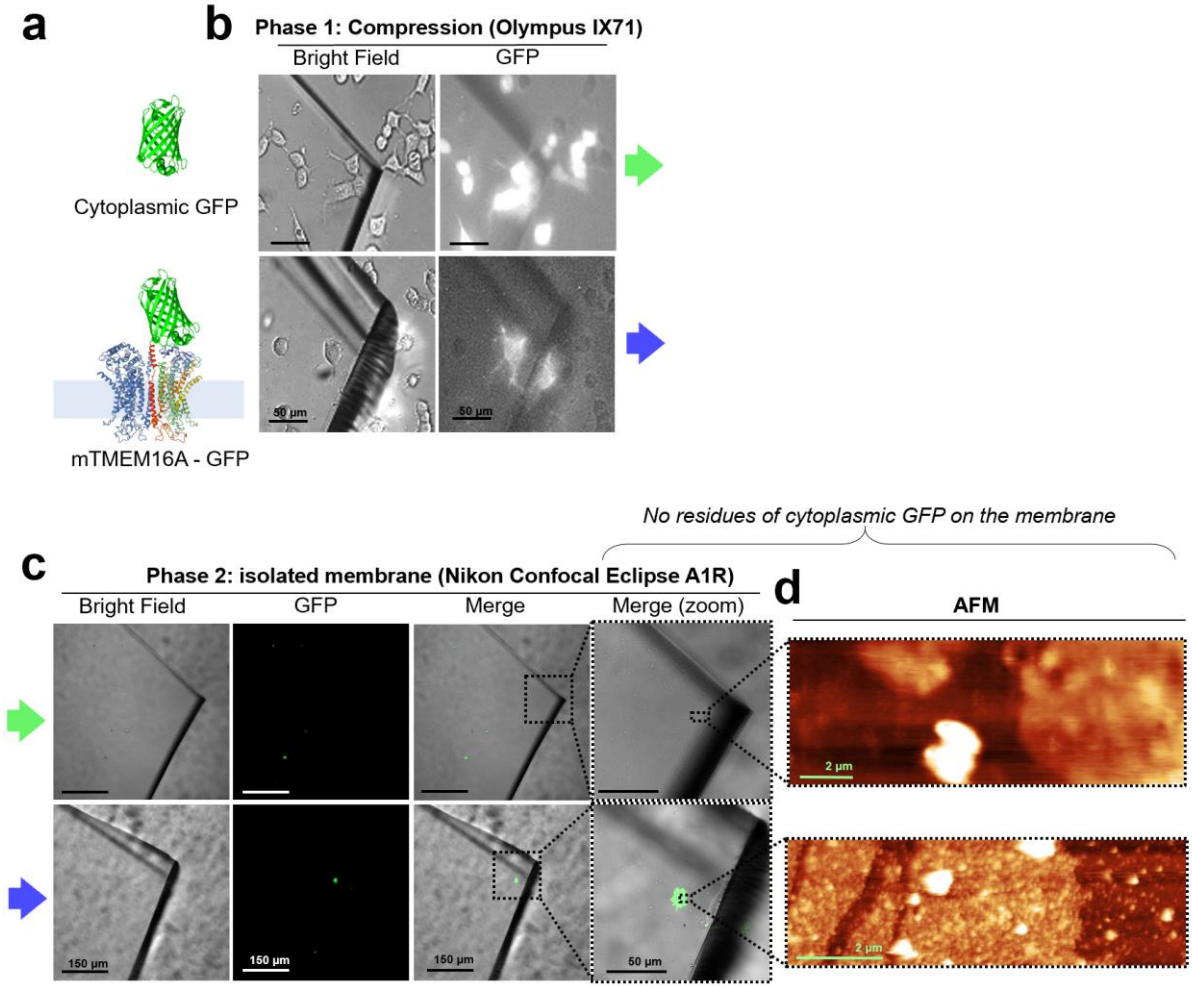

Supplementary Figure 1
Membrane proteins remain in membrane after unroofing, cytoplasmic proteins don't. **a**, (top) cytoplasmic GFP and (bottom) mTMEM16A-GFP overexpressed in NG108-15 cells. **b**, bright field and fluorescence images taken during the compression on the inverted microscope-AFM system. **c**, images of the coverslip quarter only after the unroofing process taken with the confocal microscope; the rough surface under the glass is due to the Vaseline layer used to fix the coverslip quarter. **d**, AFM images of the area in **c** showing the presence of membrane parches in both cases.

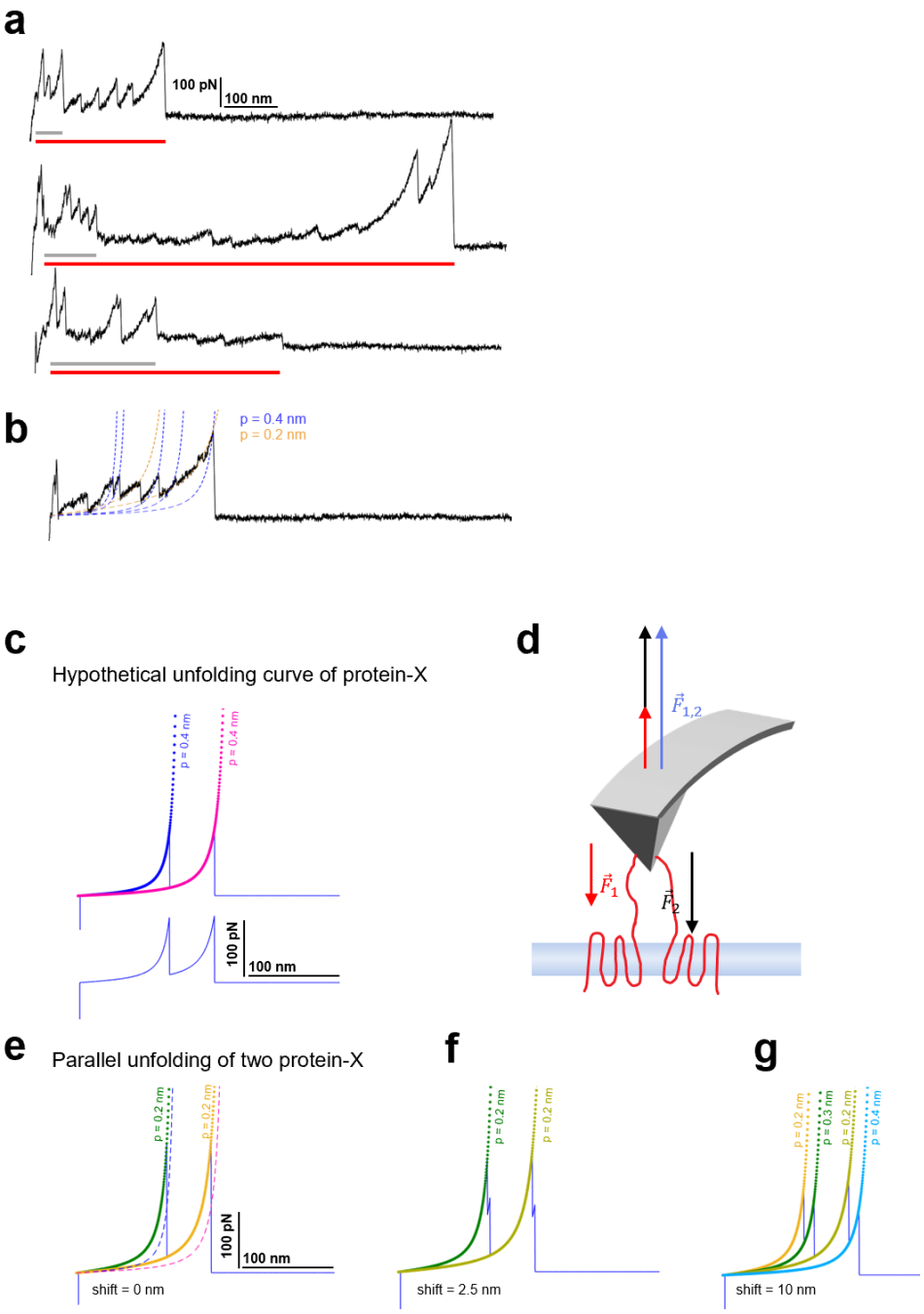

Supplementary Figure 2
Candidates of multiple unfolding and origin of persistence length deviation.
a, observed F-d curves with the features of multiple unfolding events shown in Fig 3 g (red: long protein, gray: short protein). **b**, F-d curve with intra-deviations of persistence length. **c**, hypothetical unfolding curve of protein-X (peak 1: Lc=100 nm, F=150pN; peak 2: Lc=150 nm, F=150pN) fitted with the WLC model with standard persistence length p=0.4nm. **d**, the force applied by the AFM tip balances the unfolding forces of the two proteins during the retraction. **e**, the effective F-d curve recorded during parallel unfolding of two protein-X corresponds to the sum of a single unfolding curve **c** and is best fitted with p=0.2nm. **f**, relative shift of 2.5 nm and **g**, 10 nm still result in deviations of the measured persistence length and display the doubling of the peaks.

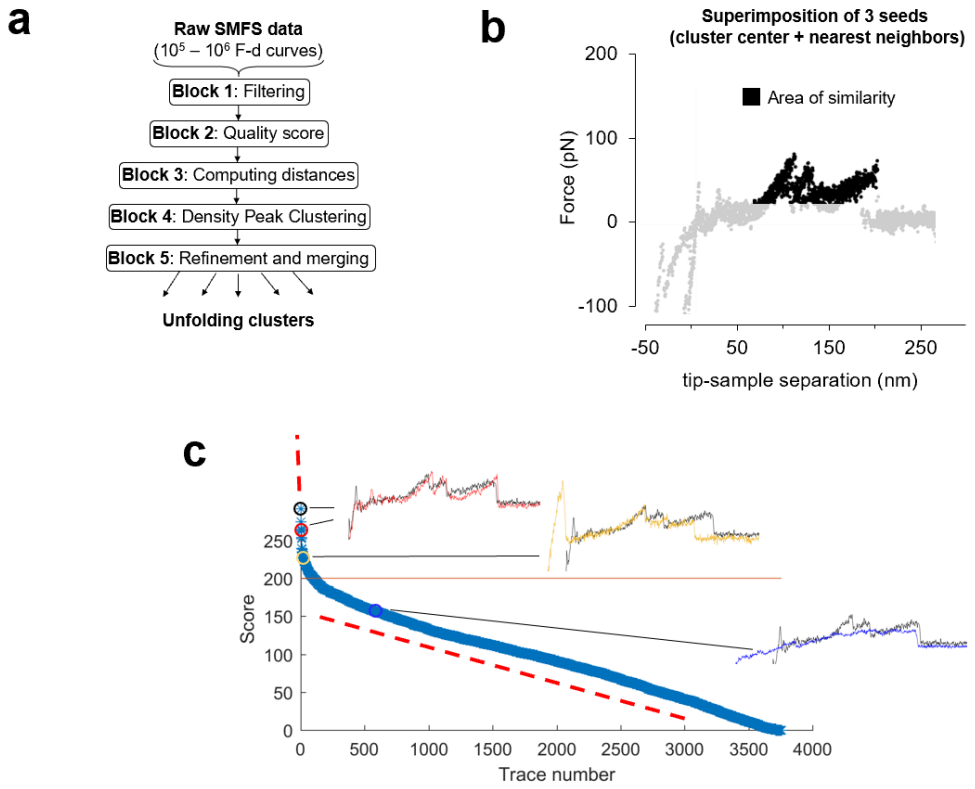

d

DRG	C. merged	Hippo.	C. merged	Rod	C. merged	Disc	C. merged
drg1	1	h1	1	r1	2	disc1	1
drg2	1	h2	1	r2	2	disc2	4
drg3	2	h3	7	r3	2	disc3	1
drg4	1	h4	2	r4	2	disc4	3
drg5	1	h5	1	r5	2	disc5	1
drg6	3	h6	1	r6	1		
drg7	1	h7	1	r7	1		
drg8	1	h8	1	r8	1		
drg9	1	h9	4				
drg10	1	h10	1				
drg11	1						
drg12	1						
drg13	1						
drg14	1						
drg15	1						

Supplementary Figure 3
Clustering.
a, block scheme of the clustering method. **b**, area of similarity (AoS) for cluster R1 used for block 5. **c**, plot of the scores in descending order. **d**, table showing the number of clusters that was merged to form the final selection of Fig. 3.

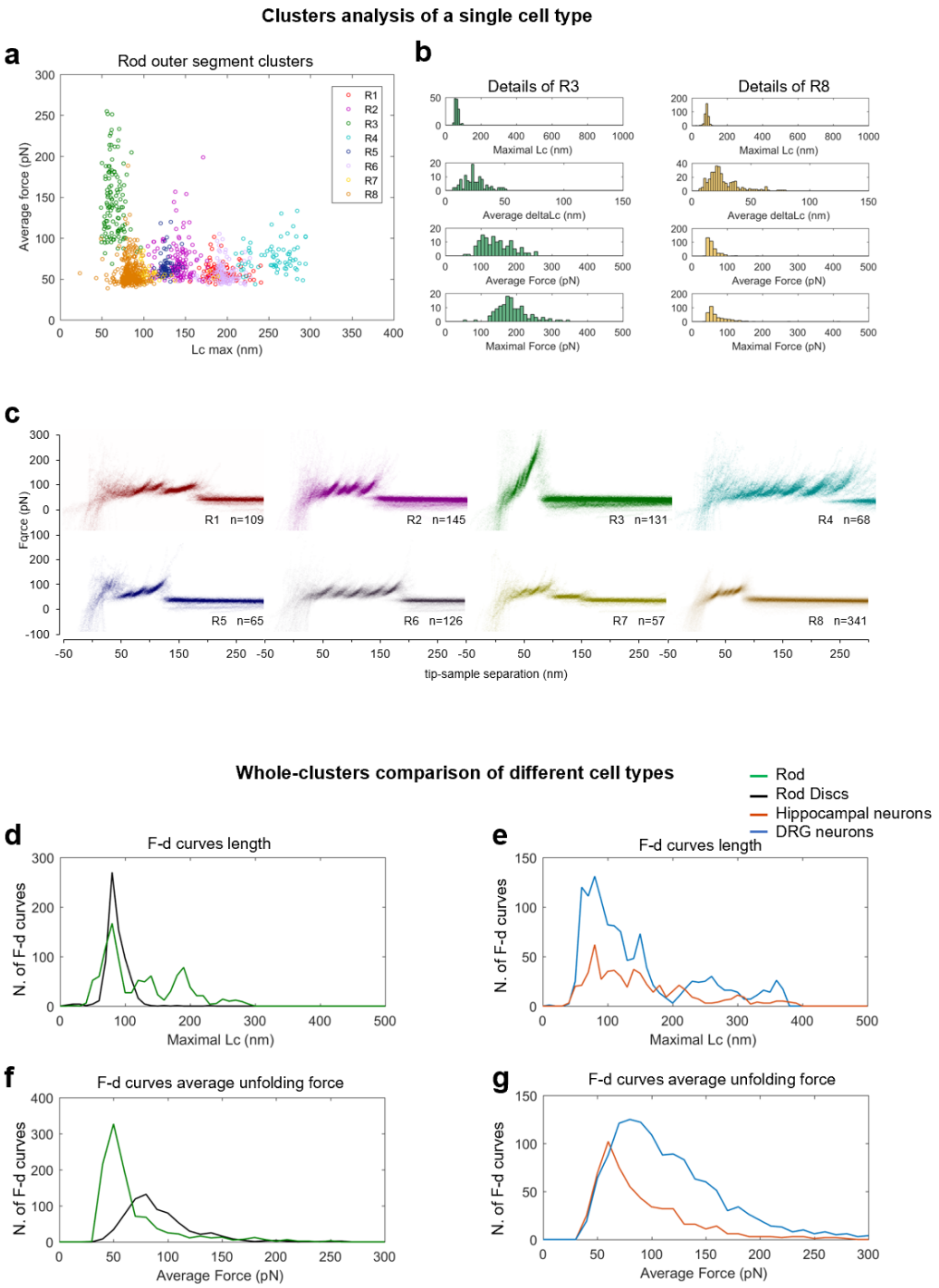

Supplementary Figure 4
Alternative visualizations for clusters analysis.
a, plot of all the F-d curves belonging to the clusters of the rod outer segment plotted with different colors in the 'average unfolding force' vs 'maximal contour length' space. **b**, distribution of representative observables for clusters R3 and R8. **c**, density plots of clusters in **a**. Comparison of the maximal contour length profiles (**d** and **e**) and of the average unfolding forces (**f** and **g**) of the four cell types investigated.

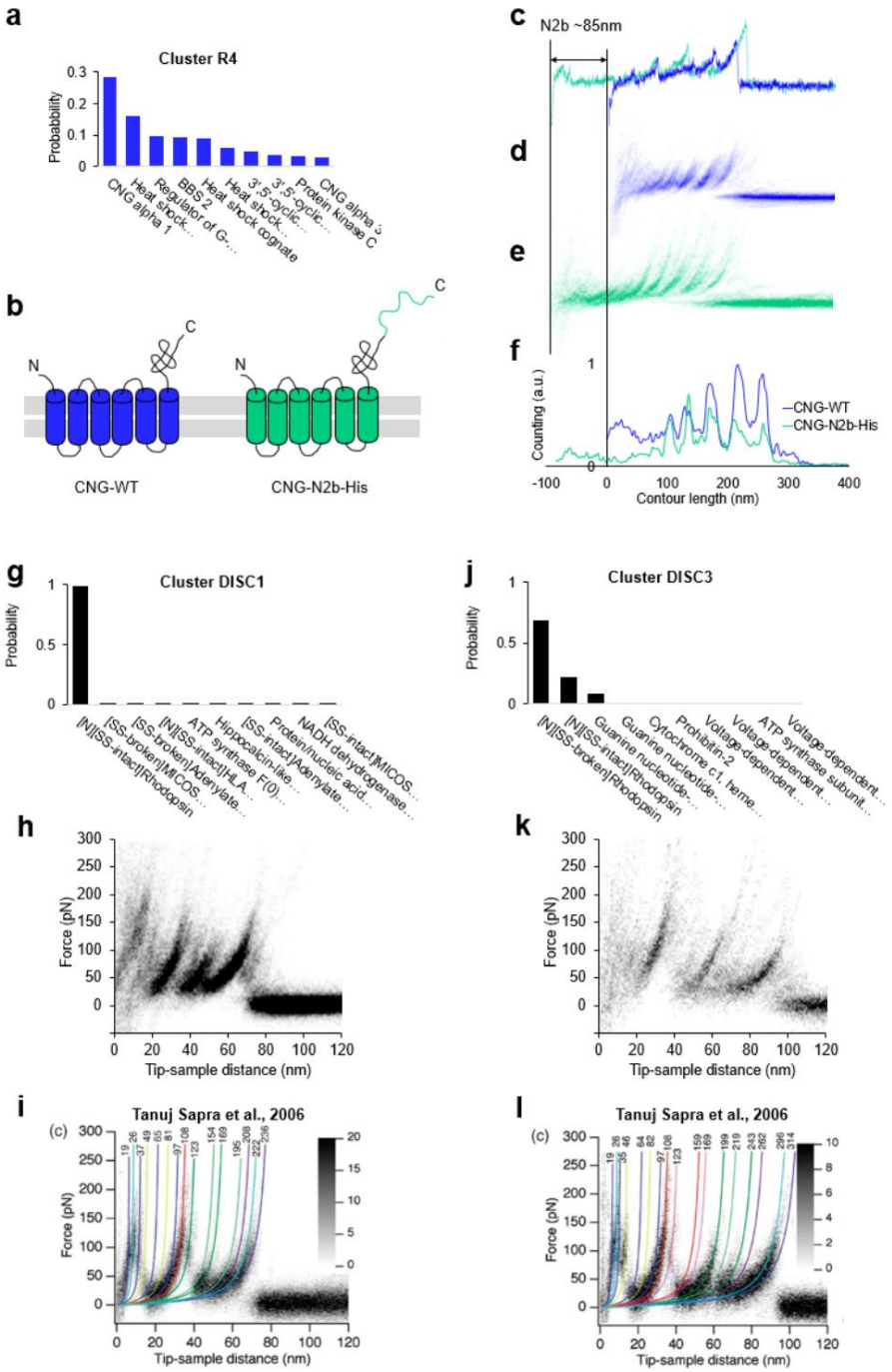

Supplementary Figure 5
Orthogonal validations of the Bayesian identification.
a, identification probability for cluster R4. **b**, scheme of the wild type CNG and of the engineered CNG linked to the N2B (unstructured amino acid chain). **c**, representative F-d curves obtained in rod outer segments (blue) and after overexpression of the CNG-N2b-His (green). **d,** density plot of R4 (n=68) and **e,** density plot of the cluster obtained after overexpression of CNG-N2b-His (n=64). **f**, comparison of the global histograms of **d** and **e** in the contour length space. **g** and **j**, identification probabilities of cluster DISC1 and DISC3 and their density plots (**h** and **k**). **i**, unfolding of rhodopsin identified by Tanuj Sapra et al. (2006) with intact SS-bond and **l**, with broken SS-bond (figure adapted from Tanuj Sapra et al. (2006)).

Chapter 3

Conclusions

The general goal of my PhD was to explore native cell membranes and membrane proteins, taking advantage of Atomic Force Microscopy. Extracting usable information from a biological native sample is hard, and my work is another demonstration of how the experimental effort alone is not sufficient to draw conclusion, indeed an equal computational effort is needed. The complexity of the native conditions needs to be taken into account seriously: both in the sample preparation stage where the experimenter has to develop a sensibility that is hard to schematize in a comprehensive to-do-list, and in the data analysis stage where it is necessary to think out-of-the-box and exploit resources that might have not been created for the desired specific purpose but that demonstrate to be useful as well.

To study native membrane and membrane proteins with AFM, I first approached the problem from the data-analysis side. In 2015 there was no comprehensive software for the analysis of protein unfolding data able to manage a large a mount of data and easily deal with it. Therefore, starting from some Matlab routines in my lab previously wrote by Paolo Fabris, I designed and developed together with Andrea Perissinotto a software capable of importing SMFS data from the most popular AFM brands (JPK, Bruker) [60]. This software—Fodis—is a visualization platform that incorporates common data representations, and it allows to perform simple, but useful, operations on the data like a filtering based on geometrical features or a selection based on the similarity of the traces, besides incorporating alignment and filtering algorithms previously published [62].

The experimental gap that I faced was the lack of a reliable technique to produce samples containing isolated patches of membranes (of any cell type) suitable for AFM investigations. For this purpose, inspired by previous studies on 'cell unroofing', I developed a single-cell unroofing technique that allowed me to reliably obtain a sample a day in about 20 minutes of preparation time [29]. With this easy access to isolated patches of native membrane, I performed a serial study on neurons and brain cancer cells, characterizing their topographical differences and mechanical properties. The optimization of this technique is still under development, and the final goal is to be able to isolate patches of membrane from *ex vivo* tissues, of potential use with biopsies of patients.

Next, I explored the unfolding pathways of the native membrane proteins with AFM-based Single-Molecule Force Spectroscopy [61]. These investigations allowed me to obtain the unfolding pathways of different native membrane proteins during the same experimental session. My results show that it is possible to

classify a cell membrane with what I called the 'unfolding phenotype', a multi-dimensional representation that is a sort of fingerprint for the cell membrane. Different cell types have different unfolding phenotypes, therefore the combination of cell unroofing and SMFS could potentially become a new screening method with clinical applications.

Acknowledgements

I would like to thank Professor Vincent Torre for the freedom he gave me to explore new techniques for membrane and membrane protein biology. I received help by many colleagues, in particular during the first years: Andrea Pedroni, Simone Mortal and Fabio Falleroni among others. I tank also Andrea Bertolucci and Professor Fabio Mammano for their unsolicited suggestions that drove me at SISSA.

Bibliography

[1] Binnig, G., Quate, C. F. & Gerber, C. Atomic force microscope. *Physical review letters* **56**, 930 (1986).

[2] Liu, S. & Wang, Y. Application of afm in microbiology: a review. *Scanning* **32**, 61–73 (2010).

[3] McClelland, G. M., Erlandsson, R. & Chiang, S. Atomic force microscopy: General principles and a new implementation. In *Review of progress in quantitative nondestructive evaluation*, 1307–1314 (Springer, 1987).

[4] Chen, I.-C. *et al.* Extremely sharp carbon nanocone probes for atomic force microscopy imaging. *Applied physics letters* **88**, 153102 (2006).

[5] Ando, T., Uchihashi, T. & Kodera, N. High-speed afm and applications to biomolecular systems. *Annual review of biophysics* **42**, 393–414 (2013).

[6] Edwards, D. T., Faulk, J. K., LeBlanc, M.-A. & Perkins, T. T. Force spectroscopy with 9-μs resolution and sub-pn stability by tailoring afm cantilever geometry. *Biophysical journal* **113**, 2595–2600 (2017).

[7] Kobayashi, H., Ogawa, M., Alford, R., Choyke, P. L. & Urano, Y. New strategies for fluorescent probe design in medical diagnostic imaging. *Chemical reviews* **110**, 2620–2640 (2009).

[8] Yguerabide, J. & Yguerabide, E. Fluorescence spectroscopy in biological and medical research. *International Journal of Radiation Applications and Instrumentation. Part C. Radiation Physics and Chemistry* **32**, 457–464 (1988).

[9] Liao, M., Cao, E., Julius, D. & Cheng, Y. Single particle electron cryo-microscopy of a mammalian ion channel. *Current opinion in structural biology* **27**, 1–7 (2014).

[10] Williams, D. H. & Mitchell, T. Latest developments in crystallography and structure-based design of protein kinase inhibitors as drug candidates. *Current opinion in pharmacology* **2**, 567–573 (2002).

[11] Contera, S. A., Voïtchovsky, K. & Ryan, J. F. Controlled ionic condensation at the surface of a native extremophile membrane. *Nanoscale* **2**, 222–229 (2010).

[12] Yin, H. & Flynn, A. D. Drugging membrane protein interactions. *Annual review of biomedical engineering* **18**, 51–76 (2016).

[13] Worcester, D., Miller, R. & Bryant, P. Atomic force microscopy of purple membranes. *Journal of microscopy* **152**, 817–821 (1988).

[14] Müller, D., Schabert, F. A., Büldt, G. & Engel, A. Imaging purple membranes in aqueous solutions at sub-nanometer resolution by atomic force microscopy. *Biophysical journal* **68**, 1681–1686 (1995).

[15] Müller, D. J., Büldt, G. & Engel, A. Force-induced conformational change of bacteriorhodopsin. *Journal of molecular biology* **249**, 239–243 (1995).

[16] Rico, F., Su, C. & Scheuring, S. Mechanical mapping of single membrane proteins at submolecular resolution. *Nano letters* **11**, 3983–3986 (2011).

[17] Lin, Y.-C. *et al.* Force-induced conformational changes in piezo1. *Nature* 1–5 (2019).

[18] Casuso, I. *et al.* Characterization of the motion of membrane proteins using high-speed atomic force microscopy. *Nature nanotechnology* **7**, 525 (2012).

[19] Marchesi, A. *et al.* An iris diaphragm mechanism to gate a cyclic nucleotide-gated ion channel. *Nature communications* **9**, 3978 (2018).

[20] Kodera, N., Yamamoto, D., Ishikawa, R. & Ando, T. Video imaging of walking myosin v by high-speed atomic force microscopy. *Nature* **468**, 72 (2010).

[21] Clarke, M., Schatten, G., Mazia, D. & Spudich, J. Visualization of actin fibers associated with the cell membrane in amoebae of dictyostelium discoideum. *Proceedings of the National Academy of Sciences* **72**, 1758–1762 (1975).

[22] Heuser, J. The production of cell cortices for light and electron microscopy. *Traffic* **1**, 545–552 (2000).

[23] Morone, N. *et al.* Three-dimensional reconstruction of the membrane skeleton at the plasma membrane interface by electron tomography. *J Cell Biol* **174**, 851–862 (2006).

[24] Sapra, K. T. *et al.* Detecting molecular interactions that stabilize native bovine rhodopsin. *Journal of molecular biology* **358**, 255–269 (2006).

[25] Rakshit, T., Senapati, S., Sinha, S., Whited, A. & Park, P. S.-H. Rhodopsin forms nanodomains in rod outer segment disc membranes of the cold-blooded xenopus laevis. *PloS one* **10**, e0141114 (2015).

[26] Whited, A. M. & Park, P. S.-H. Nanodomain organization of rhodopsin in native human and murine rod outer segment disc membranes. *Biochimica et Biophysica Acta (BBA)-Biomembranes* **1848**, 26–34 (2015).

[27] Usukura, E., Narita, A., Yagi, A., Ito, S. & Usukura, J. An unroofing method to observe the cytoskeleton directly at molecular resolution using atomic force microscopy. *Scientific reports* **6**, 27472 (2016).

[28] Nermut, M. & Williams, L. D. Freeze-fracturing of monolayers (capillary layers) of cells, membranes and viruses: some technical considerations. *Journal of microscopy* **110**, 121–132 (1977).

[29] Galvanetto, N. Single-cell unroofing: probing topology and nanomechanics of native membranes. *Biochimica et Biophysica Acta (BBA)-Biomembranes* **1860**, 2532–2538 (2018).

[30] Faria, E. C. *et al.* Measurement of elastic properties of prostate cancer cells using afm. *Analyst* **133**, 1498–1500 (2008).

[31] Lulevich, V., Zink, T., Chen, H.-Y., Liu, F.-T. & Liu, G.-y. Cell mechanics using atomic force microscopy-based single-cell compression. *Langmuir* **22**, 8151–8155 (2006).

[32] Xu, W. *et al.* Cell stiffness is a biomarker of the metastatic potential of ovarian cancer cells. *PloS one* **7**, e46609 (2012).

[33] Cross, S. E., Jin, Y.-S., Rao, J. & Gimzewski, J. K. Nanomechanical analysis of cells from cancer patients. *Nature nanotechnology* **2**, 780 (2007).

[34] Yango, A., Schäpe, J., Rianna, C., Doschke, H. & Radmacher, M. Measuring the viscoelastic creep of soft samples by step response afm. *Soft Matter* **12**, 8297–8306 (2016).

[35] Rigato, A., Miyagi, A., Scheuring, S. & Rico, F. High-frequency microrheology reveals cytoskeleton dynamics in living cells. *Nature physics* **13**, 771 (2017).

[36] Dufrêne, Y. F., Boland, T., Schneider, J. W., Barger, W. R. & Lee, G. U. Characterization of the physical properties of model biomembranes at the nanometer scale with the atomic force microscope. *Faraday discussions* **111**, 79–94 (1999).

[37] Leonenko, Z., Finot, E., Ma, H., Dahms, T. & Cramb, D. Investigation of temperature-induced phase transitions in dopc and dppc phospholipid bilayers using temperature-controlled scanning force microscopy. *Biophysical journal* **86**, 3783–3793 (2004).

[38] Sullan, R. M. A., Li, J. K., Hao, C., Walker, G. C. & Zou, S. Cholesterol-dependent nanomechanical stability of phase-segregated multicomponent lipid bilayers. *Biophysical journal* **99**, 507–516 (2010).

[39] Loi, S., Sun, G., Franz, V. & Butt, H.-J. Rupture of molecular thin films observed in atomic force microscopy. ii. experiment. *Physical Review E* **66**, 031602 (2002).

[40] García-Sáez, A. J., Chiantia, S. & Schwille, P. Effect of line tension on the lateral organization of lipid membranes. *Journal of Biological Chemistry* **282**, 33537–33544 (2007).

[41] Goncalves, R. P. *et al.* Two-chamber afm: probing membrane proteins separating two aqueous compartments. *Nature methods* **3**, 1007 (2006).

[42] Al-Rekabi, Z. & Contera, S. Multifrequency afm reveals lipid membrane mechanical properties and the effect of cholesterol in modulating viscoelasticity. *Proceedings of the National Academy of Sciences* **115**, 2658–2663 (2018).

[43] Anfinsen, C. B., Redfield, R. R., Choate, W. L., Page, J. & Carroll, W. R. Studies on the gross structure, cross-linkages, and terminal sequences in ribonuclease. *J Biol Chem* **207**, 201–210 (1954).

[44] Laio, A. & Parrinello, M. Escaping free-energy minima. *Proceedings of the National Academy of Sciences* **99**, 12562–12566 (2002).

[45] Fong, S. *et al.* Structure and stability of an immunoglobulin superfamily domain from twitchin, a muscle protein of the nematodecaenorhabditis elegans. *Journal of molecular biology* **264**, 624–639 (1996).

[46] Rief, M., Gautel, M., Oesterhelt, F., Fernandez, J. M. & Gaub, H. E. Reversible unfolding of individual titin immunoglobulin domains by afm. *science* **276**, 1109–1112 (1997).

[47] Oesterhelt, F. *et al.* Unfolding pathways of individual bacteriorhodopsins. *Science* **288**, 143–146 (2000).

[48] Doi, M. & Edwards, S. F. *The theory of polymer dynamics*, vol. 73 (oxford university press, 1988).

[49] Otten, M. *et al.* From genes to protein mechanics on a chip. *Nature methods* **11**, 1127 (2014).

[50] Johnson, A. E. & van Waes, M. A. The translocon: a dynamic gateway at the er membrane. *Annual review of cell and developmental biology* **15**, 799–842 (1999).

[51] Möller, C. *et al.* Determining molecular forces that stabilize human aquaporin-1. *Journal of structural biology* **142**, 369–378 (2003).

[52] Kedrov, A., Ziegler, C., Janovjak, H., Kühlbrandt, W. & Müller, D. J. Controlled unfolding and refolding of a single sodium-proton antiporter using atomic force microscopy. *Journal of molecular biology* **340**, 1143–1152 (2004).

[53] Thoma, J., Bosshart, P., Pfreundschuh, M. & Müller, D. J. Out but not in: the large transmembrane β-barrel protein fhua unfolds but cannot refold via β-hairpins. *Structure* **20**, 2185–2190 (2012).

[54] Marszalek, P. E. *et al.* Mechanical unfolding intermediates in titin modules. *Nature* **402**, 100 (1999).

[55] Yu, H., Siewny, M. G., Edwards, D. T., Sanders, A. W. & Perkins, T. T. Hidden dynamics in the unfolding of individual bacteriorhodopsin proteins. *Science* **355**, 945–950 (2017).

[56] Serdiuk, T. *et al.* Yidc assists the stepwise and stochastic folding of membrane proteins. *Nature chemical biology* **12**, 911 (2016).

[57] Yu, H., Heenan, P. R., Edwards, D. T., Uyetake, L. & Perkins, T. T. Quantifying the initial unfolding of bacteriorhodopsin reveals retinal stabilization. *Angewandte Chemie* **131**, 1724–1727 (2019).

[58] Kawamura, S. *et al.* Kinetic, energetic, and mechanical differences between dark-state rhodopsin and opsin. *Structure* **21**, 426–437 (2013).

[59] Spoerri, P. M. *et al.* Conformational plasticity of human protease-activated receptor 1 upon antagonist-and agonist-binding. *Structure* (2019).

[60] Galvanetto, N., Perissinotto, A., Pedroni, A. & Torre, V. Fodis: software for protein unfolding analysis. *Biophysical journal* **114**, 1264–1266 (2018).

[61] Galvanetto, N., Maity, S., Ilieva, N., Laio, A. & Torre, V. Unfolding and identification of membrane proteins from native cell membranes. *bioRxiv* 732933 (2019).

[62] Bosshart, P. D., Frederix, P. L. & Engel, A. Reference-free alignment and sorting of single-molecule force spectroscopy data. *Biophysical journal* **102**, 2202–2211 (2012).